Inkjet-Printed Microelectromechanical Systems: Materials, Process and Devices

Muhammed Karim

Electrical Engineering and Computer Sciences
University of California at Berkeley

December 1, 2017

Inkjet-Printed Microelectromechanical Systems: Materials, Process and Devices

By

Muhammed Ahosan Ul Karim

A dissertation submitted in partial satisfaction of the

requirements for the degree of

Doctor of Philosophy

in

Engineering – Electrical Engineering and Computer Sciences

in the

Graduate Division

of the

University of California, Berkeley

Committee in charge:

Professor Vivek Subramanian, Chair

Professor Elad Alon

Professor Liwei Lin

Summer 2016

Abstract

Inkjet-Printed Microelectromechanical Systems: Materials, Process and Devices

by

Muhammed Ahosan Ul Karim

Doctor of Philosophy in Engineering – Electrical Engineering and Computer Sciences

University of California, Berkeley

Professor Vivek Subramanian, Chair

Patterned deposition of solution-processed materials utilizing printing technologies is a key enabler for the realization of low-cost and large-area electronics. Inkjet printing of metal nanoparticles to form patterned conductive films is one of the major features of printed electronics. During the constrained sintering of metal nanoparticles, an in-plane tensile stress builds up due to the volumetric shrinkage of the film. While this in-plane tensile stress may induce cracks and de-lamination of the film, an out-of-plane stress gradient forces the suspended structure to curl. Curling of suspended structures is a major concern in microelectromechanical systems (MEMS). Here, the mechanism of stress gradient development in inkjet-printed silver nanoparticles film is revealed. A higher surface diffusion induced non-densifying coarsening of the nanoparticles, mediated by a higher residual polymer stabilizer concentration, retards the densifying mechanism and related volume shrinkage near the bottom of the film. A lower densification rate is substantiated by a lower Young's modulus at the bottom part of the film. Consequently, a positive stress gradient is exhibited with a lower to higher tensile stress from the bottom to the top of the film, which forces the surface-micromachined structures to curl in the upward direction. This understanding of the development of tensile stress gradient during the constrained sintering of printed nanoparticulate films constructs the way for future studies on the controlled curling of suspended structures. Moreover, having developed an understanding of stress-generation phenomena in such thin films, it is possible to propose device structures that are resistant to stress variation, or indeed, exploit this stress behavior.

Thin-film transistors (TFTs) are key devices in large-area electronic systems. Micorelectromechanical (MEM) relays are an attractive alternative to TFTs due to their excellent switching characteristics. While there have been several demonstrations of printed TFTs, reports of printed MEM switches have been generally sparse due to the difficulty in realizing robust printed suspended structures. Here, a novel MEM reed relay architecture is revealed in the first demonstration of a fully inkjet-printed 3-terminal microelectromechanical reed relay offering

excellent immunity to residual stress. In the reed relay architecture, the upward curling of the printed reed due to a stress gradient in the silver reed film is restricted by a printed blocking reed, thus delivering immunity to stress variations. The choice of sacrificial and dielectric materials for printed MEMS and their printability are also discussed in detail. The printed reed relays show hyper-abrupt switching with an on-state resistance of only ~15 Ω, immeasurable off-state leakage, a switching delay of 32 μs, and stable operation over 10^5 cycles. An analytical model of the reed relay turn-off voltage is developed, which is validated against the experimental results with varying reed relay geometrical parameters. The fully-printed processing capability of the demonstrated three-terminal reed relays in tandem with their stress tolerant nature and excellent device performance substantiates their promise as a new switching device for low-cost and large-area electronics. However, a four-terminal relay structure is required to realize logic circuits using MEM relays. This dissertation proposes a process flow to fabricate fully inkjet-printed stress-tolerant four-terminal relays with switching voltage tuning capability. This switching voltage tuning capability offers complementary relays for the implementation of logic operations.

To my parents and my wife.

Acknowledgements

Table of Contents

List of Figures

Chapter 1:   Introduction

In the 1950s, Nobel laureate Robert Solow and economist Trevor Swan predicted that technological progress is the key to the long-term growth and material well-being of a country [1], [2]. Numerous technological innovations over the past century have proven this prediction correct. Countless technological inventions, such as cars, aircrafts, communication system, energy conversion and storage, computers, data storage etc. have completely changed the human life-style all over the world. Besides adding new functionalities, one of the most important goals of technological progress is to improve product quality for a decreasing price. Any barriers towards achieving this goal have been resolved through merging knowledge from different fields of study. Recently, leveraging the advantages of inkjet-printing as a materials deposition technique and microelectromechanical systems (MEMS) as a device technology, a new arena of technology has emerged. This new field of technology is titled as "Printed MEMS". Printed MEMS aims at low-cost device solutions for large-area electronics.

1.1 Printed Electronics

Printing technology was originally invented to facilitate the mass-production of texts and graphic arts. The vast improvement of printing tools over the past century has led to the development of sophisticated material deposition printers. Also, the development of solution processed metallic, semiconducting and dielectric materials have paved the way to print both passive and active electronic devices. Consequently, printed electronics has gained a huge interest over the last decade [3]–[5]. As a processing technique, printing has several advantages and disadvantages compared to conventional microfabrication. Figure 1-1 shows the process steps required to deposit and pattern a certain material using conventional microfabrication with lithography versus the steps required to achieve this using a printing technique. The requirements for conventional microfabrication include a vacuum chamber for material deposition, masks for patterning, and a way of etching unwanted materials, all of which result in an increase in processing cost. However, printing does not require any vacuum chamber for material deposition or masks for patterning. Moreover, printing is a fully additive process that does not require any etching step. All of these factors make it a much cheaper processing technique than conventional microfabrication. The cost benefit of the printing process is greatly amplified for large-area systems. However, printing techniques have poor resolution compared to conventional microfabrication. For example, a minimum feature size of ~ 20 μm can be deposited using inkjet-printing, whereas conventional lithography can achieve sub-10 nm resolution utilizing the multiple patterning technique [6]. Also, printing has poor reliability compared to the conventional microfabrication. Table 1-1 provides a comparative summary of different aspects of materials processing using printing and conventional microfabrication techniques.
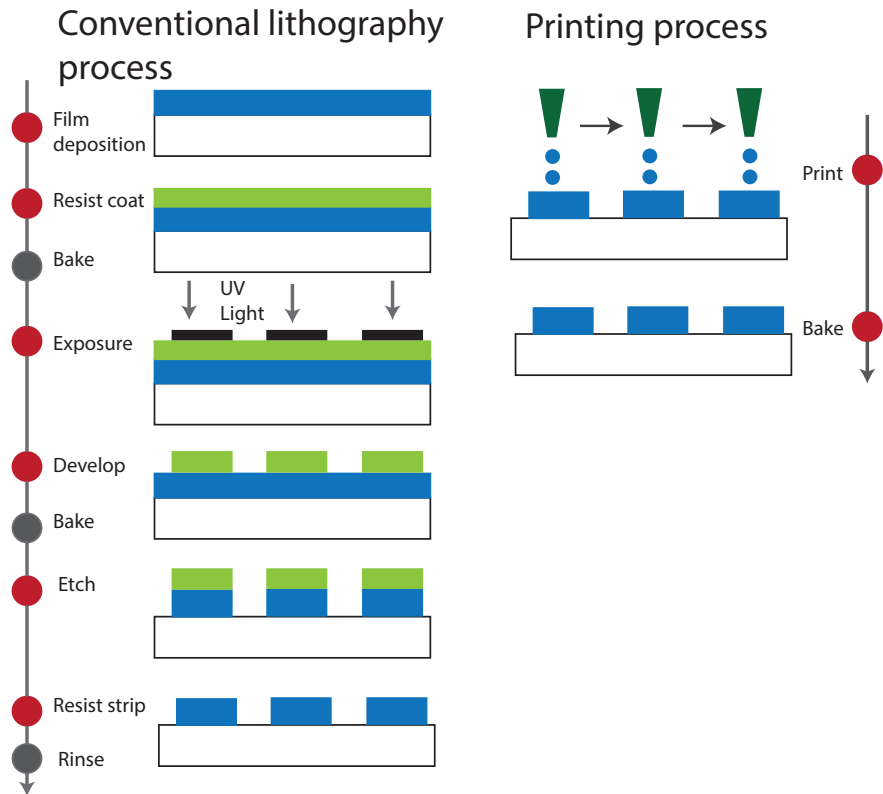
Figure 1-1. Patterned deposition of materials using conventional lithography process and printing process.

	Lithography	*Print*
Vacuum	Dependent	Independent
Mask	Dependent	Independent
Cost	High	Low
Large-area Processing Capability	Poor	Good
Max. Process Temperature	High	Low
Substrate Choice	Limited	Ample
Resolution	High	Not high
Reliability	High	Not high

Table 1-1. Different processing aspects of conventional lithography and printing techniques.
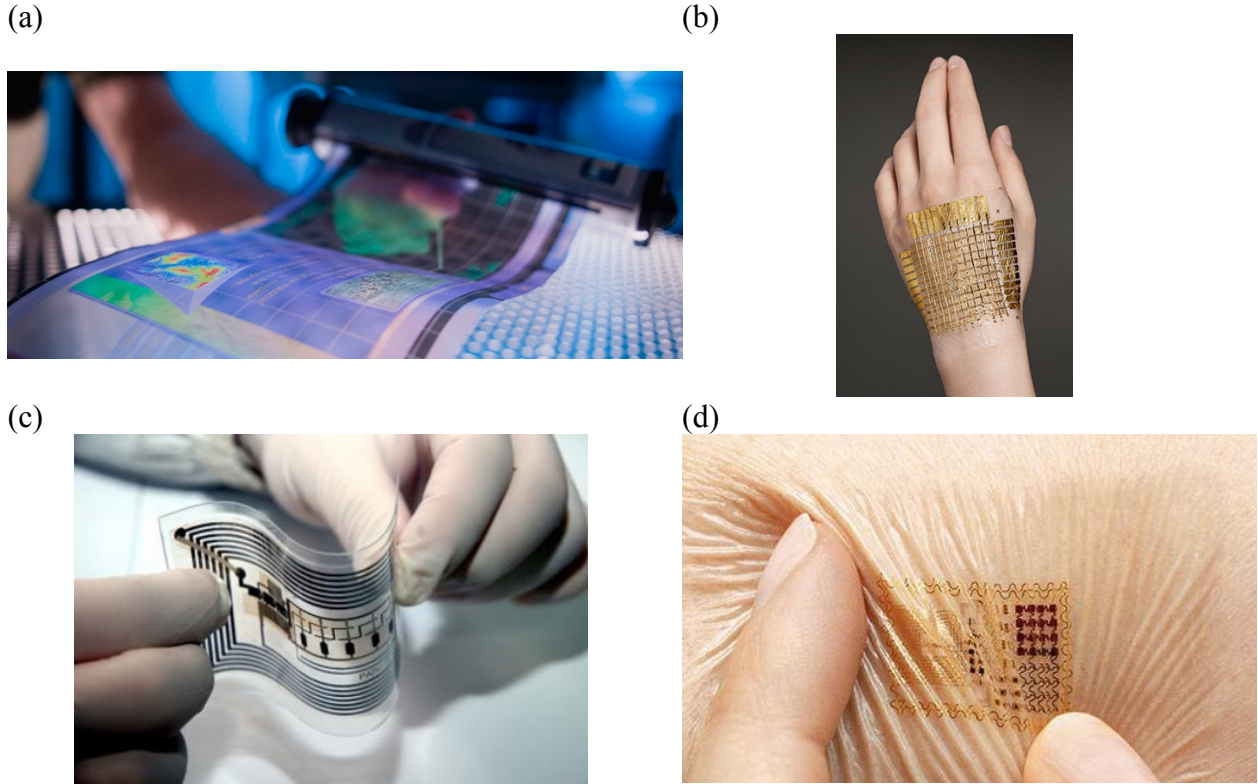
Figure 1-2. Printed electronics for large-area electronics. (a) flexible display (www.factor-tech.com), (b) E-skin (www.hight3ch.com), (c) RFID tag (www.wired.com), (d) Smart bandage (www.brit.co).

Despite the aforementioned resolution limitation, printed electronics has gained immense attention due to its low-cost and large-area processing capability of electronic materials. Printed electronics has exhibited substantial promise in many large-area applications (see Figure 1-2). These applications include displays, sensors, radio-frequency identification tags, transistors, MEMS devices, batteries, solar cells, organic light-emitting diodes (OLEDs), antennas, passive components etc. [7]–[28].

Another key advantage of the printing process is the low maximum processing temperature. The glass transition temperature of typical plastic substrates is less than 200 ^{0}C [29], [30]. For processing on flexible plastic substrates, the process temperature cannot exceed the glass transition temperature to avoid the deformation of the substrates. Fortunately, low-temperature compatible metallic inks have been demonstrated in recent years [31], [32]. Also, low-temperature compatible dielectrics and semiconductors have been developed from organic small molecules and polymers [33]–[36]. Recently, printed thin-film transistors (TFTs) have been demonstrated as pixel switches in active matrix display backplanes [7], [8], [37]–[40]. Figure 1-3 shows a fully printed backplane with organic TFTs in an electronic paper display.

3
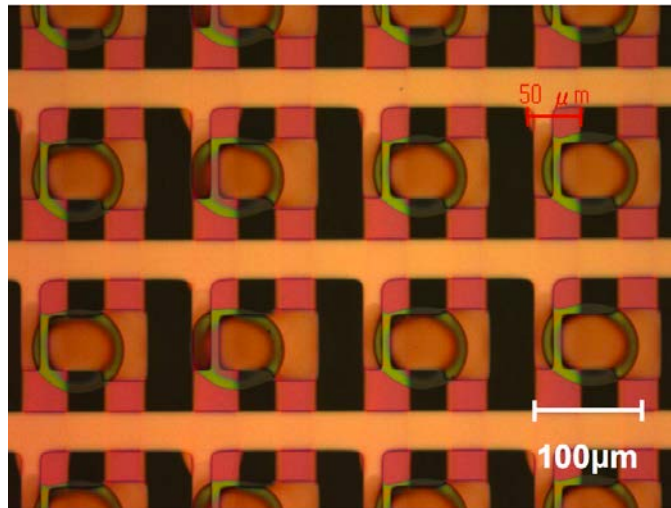
Figure 1-3. All-printed display backplane for electronic paper [40].

In a nutshell, with the advantages of low-cost and low-temperature processing, printed electronics has become a very promising technology for realization of large-area electronics.

1.2 Printing Techniques

Many different printing techniques have evolved based on the transfer of ink to the substrate and their patterning methods. The major printing technologies include inkjet, gravure, screen, offset and flexographic printing. Each of these printing technologies have their advantages and disadvantages in terms of pattern resolution, throughput, registration accuracy, ink usage etc. In this section, a brief survey of different printing techniques will be presented including an analysis to select a suitable process for printed electronics.

1.2.1 Screen Printing

Screen-printing is the most matured technology for printed electronics as it has been practiced in the electronics industry for many decades to print metallic interconnects on printed circuit boards. A screen printer is a simple setup comprising of a screen, squeegee, press bed, and substrate, as shown in Figure 1-4. In flatbed screen printing, the ink poured on the screen is spread using a squeegee to move it across the screen. This results in a transfer of ink through the stencil openings to the substrate beneath. Flatbed screen printing has the disadvantage of low throughput. For higher throughput, flatbed screens can be substituted with rotary screens for continuous processing in

which the web of the screen is folded while the squeegee and ink are placed inside the tube. But the screens for rotary setup are expensive and very difficult to clean [41].
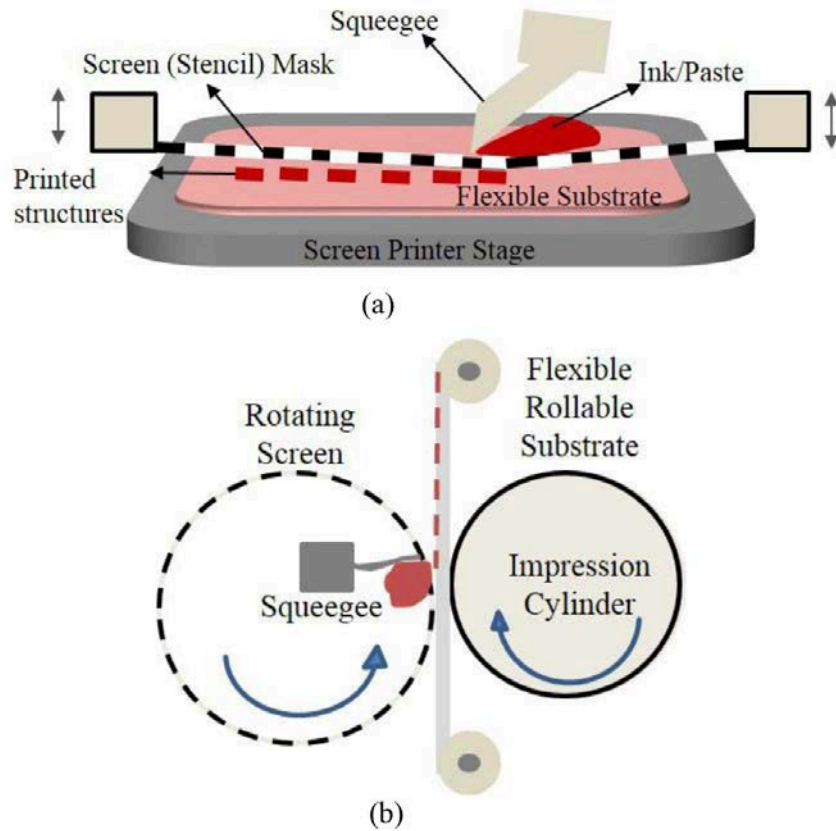
Figure 1-4. Flatbed screen printing with planar substrates under screen and squeegee for solution dispensing. (b) Rotary screen printer with moving substrate (web) between cylindrical mask and impression cylinder. From Ref. [47]

Although screen printing is a very simple process, the print quality and characteristics are affected by various factors such as solution viscosity, printing speed, angle and geometry of the squeegee, snap-off between the screen and substrate, mesh size and material [42], [43]. Screen printing also has an inherent pattern resolution limitation since it is difficult to push the ink through the very small mesh openings of finer features [44], [45]. Screen printing typically uses paste-like inks, with very high viscosities; the high viscosity minimizes the flow of ink on the substrate after deposition and ensures pattern fidelity. Ink formulation for screen printing requires the use of binders to make high viscosity ink. Therefore, a typical screen printable conductive ink consists of conductive particles or flakes interspersed with a binder material, such as a polymer, within a

solvent base. The resistivity of screen-printed materials is typically poor compared to an equivalent film of pure metal, as the binder material is relatively nonconductive. This imposes the requirement of printing thicker or wider features to minimize resistance [46]. Without giving any consideration to proper tuning of the ink properties and mesh count, a nominal print resolution of >50 μm and pattern thickness of a few microns are common. Furthermore, screen printing typically produces films with large roughness due to the nature of inks as discussed above. As a result, the use of screen printing is limited for the fabrication of thin-film devices.

1.2.2 Gravure, Flexographic and Offset Printing

Gravure, offset and flexography are contact based printing techniques and somewhat related to each other. All of these techniques utilize direct transfer of functional inks in pre-patterned features onto a substrate via physical contact with a drum (see Figure 1-5). Ink is dispensed into the drum such that it lies within the depressed regions of the pattern but not in the elevated regions of the drum [48], [49]. The drum is pressed against the substrate, which results in transfer of most of the ink contained in the wells onto the substrate. The choice of drum material is the main difference between gravure and flexographic printing. Gravure makes use of a hard metallic drum, while flexographic printing makes use of a relatively compliant drum. Therefore, the requirements for the ink viscosity and surface wetting properties gravure printing are different from the flexographic printing. This results in slightly different pattern fidelity characteristics. Offset printing adds an intermediate step. In offset printing, the ink from the master drum is transferred to an intermediate drum, which, in turn, transfers the ink to the substrate [50]. Although, the use of an intermediate drum typically results in better drum reusability, the double transfer typically requires the use of higher viscosity inks. Similar to the screen printing ink, gravure and flexographic printing typically require the use of binders. However, the required ink viscosity for gravure and flexographic printing are less than that of screen printing ink. This allows the use of lower binder content for the realization of features with lower resistivity. Among these printing techniques, gravure is considered as the most promising technology for printed electronics due to its recent development of high resolution (sub 5 μm) printing capability with high throughput [51], [52].

The gravure printing tools consist of a large cylinder electroplated with copper and engraved with microcells. The microcells are engraved using wet etching, laser or electromechanical means. The engraved cylinder is electroplated with chrome to protect it from wear and tear during the ink transfer and contact with the substrate. The transfer of the engraved pattern from the cylinder to the substrate comprises of four main stages: cell filling, doctor blade wiping, ink transfer and ink spreading on the substrate. Engraved cells are filled with the ink either by using a reservoir beneath the rotating gravure cylinder or through a nozzle dispenser from the top.

6

(a)
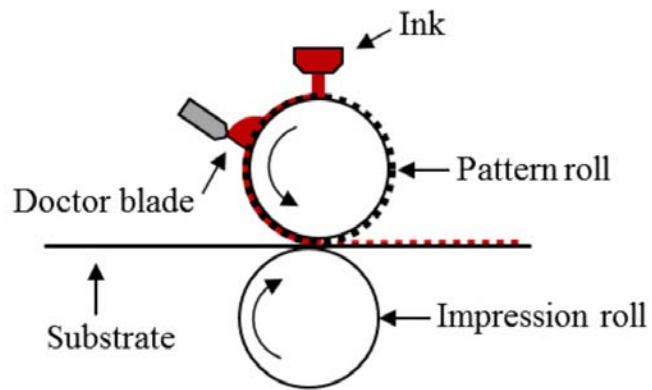
(b)
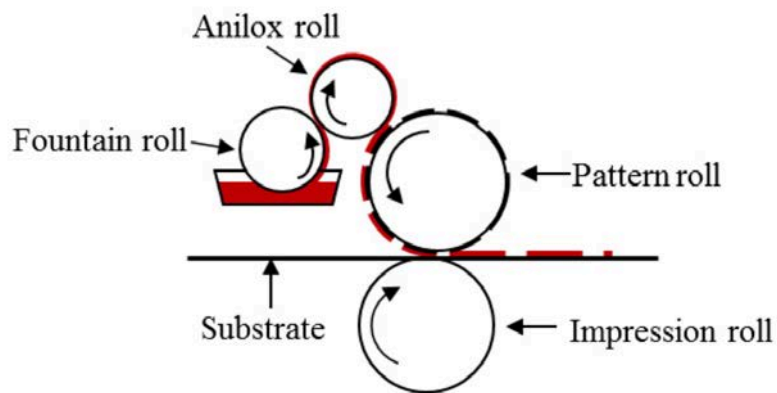
(c)
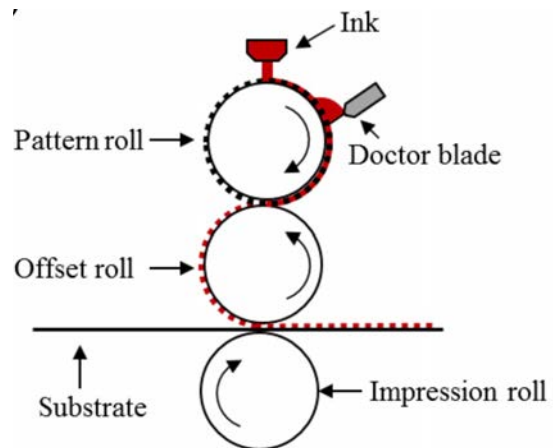
Figure 1-5. Schematic representation of (a) rotary gravure system, (b) flexographic system, and (c) offset printing system.

A doctor blade is used for wiping extra ink from the rotating cylinder. Ink is transferred through capillary action onto a substrate when it comes in contact with the engraved microcells. Surface properties of the microcells and the substrate can be modified for better transfer of ink from the cells. Also, for efficient transfer of the ink, proper ratio of the cells width and depth is required. Both cell emptying and drop spreading play important roles in defining the final printed features. After ink transfer, the drop will begin to spread on the substrate to minimize its total surface energy. Line formation occurs when drops are deposited close together and thus coalesce as they spread on the substrate.

Currently, the main bottleneck for gravure printing are the non-idealities during the doctor blade wiping process and poor registration accuracy. A better doctor blade wiping process is required to reduce the drag-out tail and improve pattern fidelity. Also, an improvement in the gravure printing tool is necessary for high registration accuracy to take advantage of fully gravure printed high-resolution and high-throughput electronic devices.

1.2.3 Inkjet Printing

The vast majority of previously demonstrated printed devices have been fabricated using ink-jet printing because of its excellent material compatibility and ease of use. Inkjet printing is a digital printing technique where drops are jetted on demand. The setup for an inkjet printing system is very simple (see Figure 1-6) The substrates are placed on a motorized platen. The system requires two cameras; one is a top view camera to view the sample and another is a drop watcher camera. Different controller units control the platen and nozzle head movement, pressure of the reservoir, platen temperature, and nozzle temperature. Inks in the form of colloidal or chemical solutions are kept in pressurized reservoirs. Inks are dispensed through a micrometer sized inkjet nozzle head. A number of mechanisms for actuation of inkjet nozzle head have been developed. Among these, the most prominent techniques are thermal, piezoelectric and electrohydrodynamic systems. Droplets of very small volume (1-100 pL) are ejected using the corresponding pulse generated by either thermal or piezoelectric actuators used in the inkjet nozzle head.

A thermal nozzle head uses a heater in the form of a resistor to superheat the ink to its spinodalian limit. As a result, the ink boils and a bubble is created in the time span of microseconds and causes pressures that cause droplet ejection (Figure 1-7). Highly scaled heads have been realized using thermal bubble processes due to the simplicity of design. However, the requirement of a heating step poses compatibility concerns for thin-film electronic materials, where the inks are usually temperature sensitive.

In piezoelectric inkjet printing, print heads are actuated using a piezoelectric crystal. The deformation of the crystal through an appropriate electrical waveform creates a pressure wave that

ejects ink droplets (Figure 1-8) [54]–[57]. Unlike thermal inkjet heads, piezoelectric heads do not suffer from ink degradation concerns due to heating.
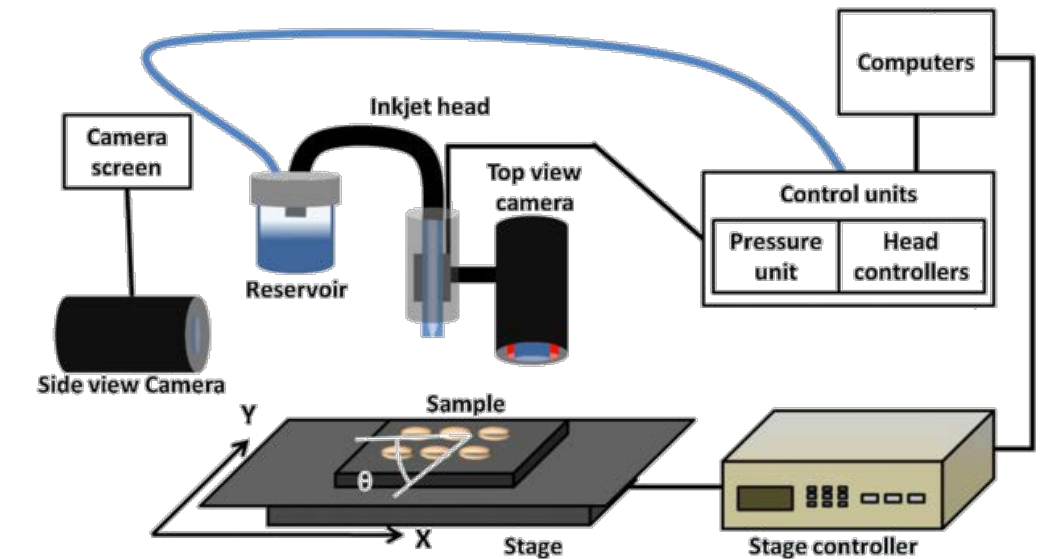
Figure 1-6. Schematic illustration of an inkjet-printing system comprising of motorized platen, pressurized reservoir, top view camera, drop watcher camera, and control units. Figure drawn from [53].
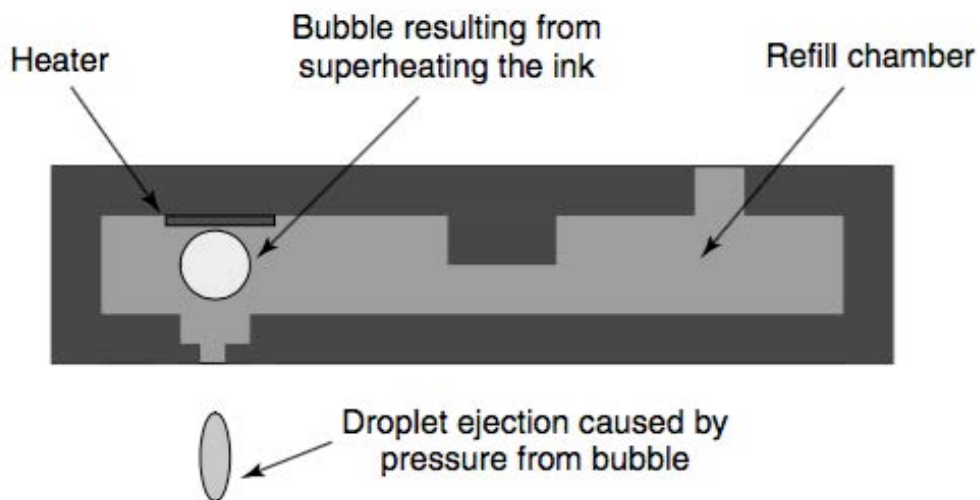
Figure 1-7. Cross-section of a typical bubble jet dispenser showing droplet generation mechanism.
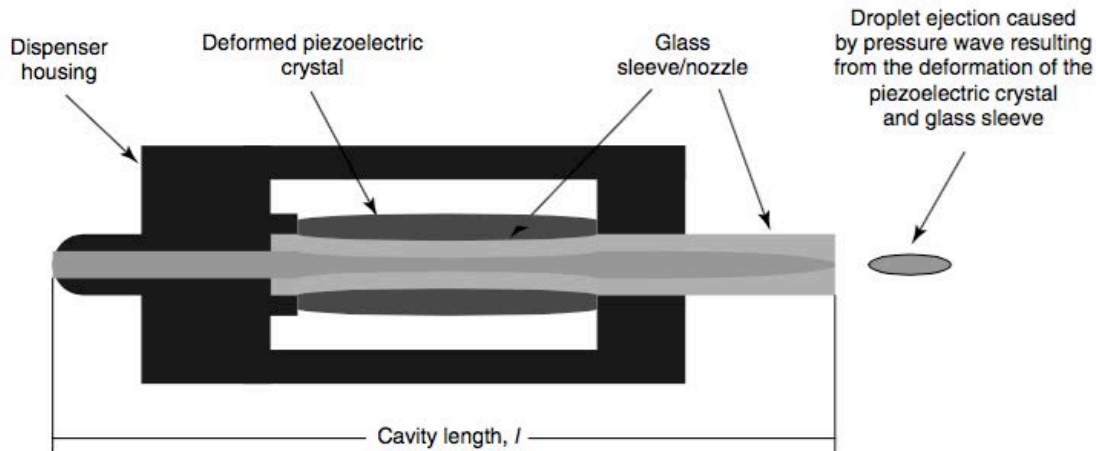
Figure 1-8. Cross-section of a piezoelectric inkjet dispenser showing droplet generation mechanism.

Inkjet has several advantages for printed electronics. Inkjet typically requires the lowest viscosity inks compared to other printing technologies. Therefore, it is possible to produce inkjet compatible inks with no binder materials. This allows for the realization of high quality inkjet printed patterns. Also, inkjet is a non-contact printing method which reduces the possibility of introducing contamination in the printed electronic devices. As a drop on demand printing technique, inkjet systems also provide zero waste of materials. Most importantly, the mechanism of droplet and pattern formation is very well understood [57]–[59]. However, inkjet-printing has limited throughput due to its serial nature of processing. This disadvantage can be overcome by designing an inkjet system with a large number of nozzles to realize throughput enhancement via parallelization [60]. In addition, inkjet-printing typically has higher registration accuracy than any other printing technique. Registration accuracy is very important in a process flow that requires multiple layers of material deposition.

Since all the printing techniques have their advantages and disadvantages, a systematic comparison is necessary to select the suitable printing technique for electronics fabrication. A good printing process for electronics fabrication should provide high pattern resolution, high throughput, high pattern fidelity, high layer-to-layer registration accuracy, materials deposition capability on complex topography and good quality of deposited materials. Table 1-2 compares the performance parameters for different printing techniques based on the values reported in literature.

Among the different printing techniques, gravure and inkjet printing provide the most benefits for use as a processing technique for electronic devices. High resolution, high throughput and high pattern fidelity makes gravure a suitable process to fabricate thin-film devices. However, the contact nature of printing and the use of binder materials to get high viscosity ink reduces the

10

quality of printed materials in gravure printing processes. Also, gravure systems have lower registration accuracy, which can create overlap between layers, and thus introduces parasitic capacitance into the circuit. Gravure is also not very good at depositing materials on complex topographies.

Parameters	Gravure	Offset	Flexographic	Screen	Inkjet
Best resolution (μm)	5	20	40	40	20
Print thickness (μm)	0.02-12	0.6-2	0.17-8	3-30	0.01-1
Printing speed (m/min)	8-100	0.6-15	5-180	0.6-100	0.02-5
Required solution viscosity (Pa s)	0.01-1.1	0.05-2	0.01-0.5	0.5-5	0.001-0.1
Solution surface tension (mN/m)	41-44	NA	13.9-23	38-47	15-40
Material wastage	Yes	Yes	Yes	Yes	No
Experimental approach	Contact	Contact	Contact	Contact	Contact-less
Registration accuracy	Poor	Poor	Poor	Poor	Good
Printing on complex topography	Poor	Poor	Poor	Poor	Good
Hard mask requirement	No	No	No	Yes	No
References	[5], [48], [52], [61]–[64]	[5], [61], [65]–[67]	[5], [61], [63], [68]–[70]	[5], [61], [71]–[73]	[10], [61], [74]–[78]

Table 1-2. Comparison among different printing technologies.

Inkjet printing has lower resolution and throughput than gravure printing. But the non-contact nature of printing and use of binder-less ink makes inkjet-printing suitable to deposit higher quality materials than other printing techniques. Moreover, inkjet-printing has higher registration accuracy and it can be used to deposit materials on complex topographies. These properties make inkjet-printing a very good processing technique for fabrication of thin film devices. Inkjet-printing is

particularly beneficial to fabricate microelectromechanical (MEM) devices, where multiple layers of materials are deposited on complex topographies. This dissertation primarily focuses on the development of fully inkjet-printed processes for MEM devices, which requires insight into basic processing principles and device operations for microelectromechanical systems (MEMS). Therefore, the next section presents a brief outline of MEMS processing and an overview of various classes of MEMS devices.

1.3 Microelectromechanical Systems

From the nomenclature, microelectromechanical system (MEMS) can be explained as a micrometer scale electrical system consisting of some sort of moving elements. But the field of MEMS has grown beyond this definition, encompassing many other types of micrometer and nanometer scale systems including magnetic, thermal, fluidic and optical systems. MEMS has miniaturized many macro scale sensors and actuators such as the accelerometer, gyroscope, motors etc. Moreover, MEMS technology has accomplished much more than just reducing the size of existing systems, it has also created new products such as the inkjet-print head, thin-film magnetic disk head etc. MEMS technology also contributed to microfluidic devices, which has enabled astounding advancement in biochemical analysis and drug discovery.
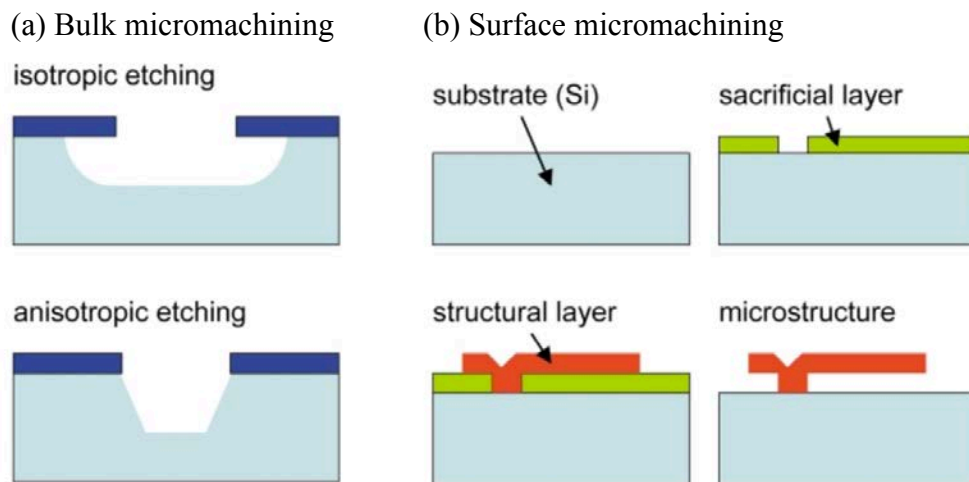
Figure 1-9. Bulk and surface micromachining to fabricate MEMS structures. This figure is taken from reference [79].

Typically, the fabrication of MEMS devices involves lithography-based conventional microfabrication techniques augmented with a specialized technique called "micromachining". Micromachining is the technique of selectively removing materials at the micrometer scale using

dry or wet etching to fabricate three dimensional (3D) devices [79], [80]. Dry etching techniques include plasma or reactive ion etching (RIE), deep RIE (DRIE), and vapor phase dry etching. Wet etching involves either isotropic or anisotropic chemical etching. There exist two main categories of micromachining: bulk micromachining and surface micromachining. In bulk micromachining, features are etched into the bulk of the substrate, while in surface micromachining, features are built up from the surface. In surface micromachining, the structures are fabricated on sacrificial layers and subsequently released by etching these layers. Figure 1-9 shows the bulk micromachining and surface micromachining processes.

One of the key aspects of MEMS devices is that the devices are suspended in the air. This suspended nature of the MEMS structures is particularly important in two main classes of micro-devices: sensors and actuators. Sensors convert the non-electrical input into electrical signals and actuators mainly convert electrical signals into mechanical displacements. The non-electrical inputs in a sensor system can be in the form of four main categories: mechanical, optical, magnetic and thermal signals. For a sensor system, suspended structures are especially beneficial for the improved sensitivity and efficiency since the sensing materials can avoid substrate losses. For example, Figure 1-10 shows the SEM image of the high performance nanometer-thick freestanding uncooled infrared micro-bolometer fabricated using surface micromachining technique. Micro-bolometers are used as detectors in thermal cameras. Infrared radiation strikes the absorber material, heating it, and thus changing its electrical resistance. This resistance change is measured and mapped into temperatures, which can be used to create an image. The lower the mass of the illuminated absorber, the less IR energy is needed to increase its temperature a given amount, and the more sensitive it is. The heating mass can be reduced significantly by suspending the absorber materials in air.
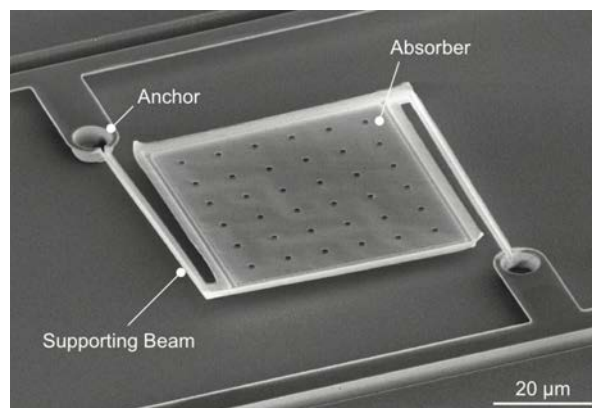
Figure 1-10. SEM image of a nanometer-thick freestanding uncooled infrared bolometer [81].

13

Electrostatic sensing and actuation of movable structures is used in the vast majority of MEMS sensors and actuators. Comb drive based electrostatic sensors and actuators such as accelerometers, gyroscopes, resonators, filters etc. have been successfully integrated in many commercial products. MEMS accelerometers are used in modern cars for a large number of purposes including airbag deployment and electronic stability control. MEMS accelerometers are also used in consumer electronics devices such as game controllers, personal media players and cell phones and a number of Digital Cameras. MEMS gyroscopes and accelerometers are used in remote controlled or autonomous helicopters, planes and drones for automatically sensing and balancing roll, pitch and yaw.
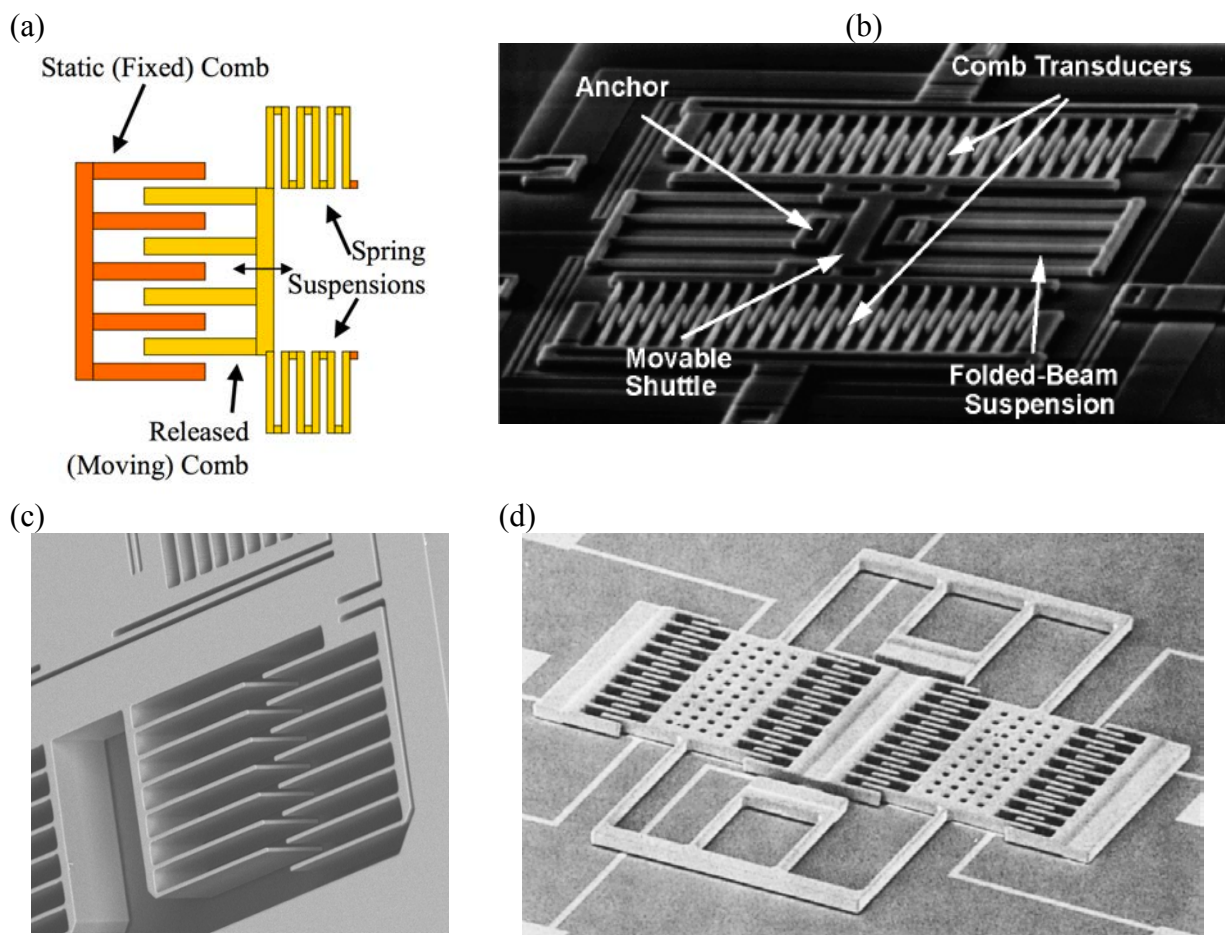
Figure 1-11. (a) Schematic and (b) SEM image of comb drive. (c) Zoomed image of accelerometer. (d) SEM image of vibrating gyroscope.

Comb drives are transducers where electrostatic forces act between two electrically conductive combs. Comb drives consist of a static comb and a suspended movable comb (Figure 1-11(a) and

(b)). In this structure, interlacing comb fingers create large area to increase capacitance. In the comb drive based sensors, any movement of the movable comb is sensed by measuring the changes in capacitances between the interlaced fingers. Figure 1-11(c) shows SEM image of a zoomed section of an accelerometer and Figure 1-11(d) shows SEM image of a gyroscope.

Besides comb drive based actuators, MEMS relays are particularly interesting devices that use electrostatic actuation of movable structures (Figure 1-12) to turn the relay on and off. In this electrostatic switch, a movable electrode and a fixed electrode form a capacitor. When a voltage is applied to this capacitor, electrostatic force, generated due to the attraction between oppositely charged electrodes, accelerates the movable electrode toward the fixed electrode. This force is always attractive regardless of the polarity of the applied voltage and its strength depends on the area of the electrodes and the separation between them.

(a) (b)
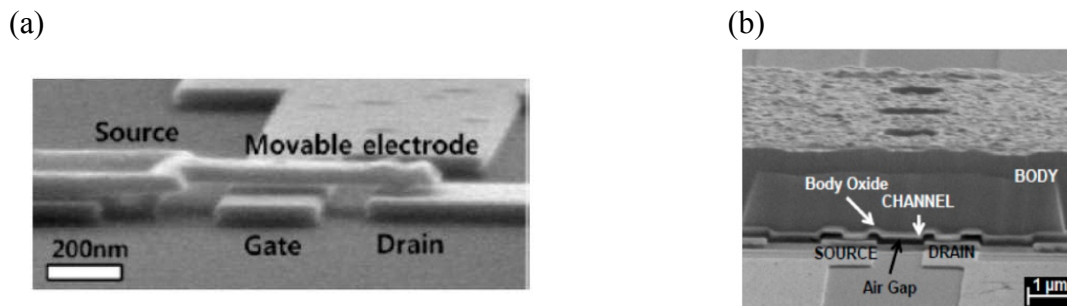
Figure 1-12. SEM images of MEMS relays showing movable electrodes and air gap.

One of the key aspects of a MEMS relay is that it possesses the properties of an ideal switch: very abrupt on/off switching transition and no leakage current in the off-state. These properties of MEMS relay give it the potential to be a highly energy efficient switching device. Therefore, MEMS Relays are considered candidates to be an energy efficient alternative to field-effect transistors.

1.3.1 Energy-Efficient MEMS Relays

The invention of integrated circuit (IC) by Jack Kilby in 1958 initiated a revolution that transformed the world into the modern high-tech age [82]. Metal-Oxide-Semiconductor Field Effect Transistor (MOSFET) has been the main building block with which ICs are built. Over the past several decades, consistent improvement of transistors has provided an exponential increase in computing power. The pace of innovation was set by "Moore's Law". Moore's Law is an observation made by Gordon Moore, which states that the number of transistors on a chip

approximately doubles every two years [83], [84]. The world's first single-chip microprocessor (the Intel 4004 introduced in 1971) had 2300 transistors and operated with a clock frequency of 108 kHz. Today's Intel Core i7 Extreme Processor has over 2.27 billion transistors with six processing cores operating at a clock frequency of up to 4GHz [85].

In the modern world, billions of ICs are tirelessly at work in almost all electronic appliances. However, power dissipation and management issues at the hardware level threatens the tempo of this revolution in future years. This power dissipation crisis originates at the transistor level. Figure 1-13 shows the transfer characteristics of a n-channel MOSFET. Here, the transition from the off-state to on-state is not abrupt and there exist an off-state leakage current (I_{OFF}). This leakage current causes a static energy dissipation ($E_{LEAKAGE}$). The amount of the off-state leakage current depends on the subthreshold swing (SS). Subthreshold swing is defined as the inverse slope of the $\log(I_D)$-V_G curve in the subthreshold region. Moreover, with the same subthreshold swing, the off-state leakage increases exponentially with the reduction of the threshold voltage (V_{TH}). On the other hand, a reduction in threshold voltage and chip operating voltage (V_{DD}) is necessary to reduce the switching or dynamic energy dissipation ($E_{DYNAMIC}$) without sacrificing operating speed.
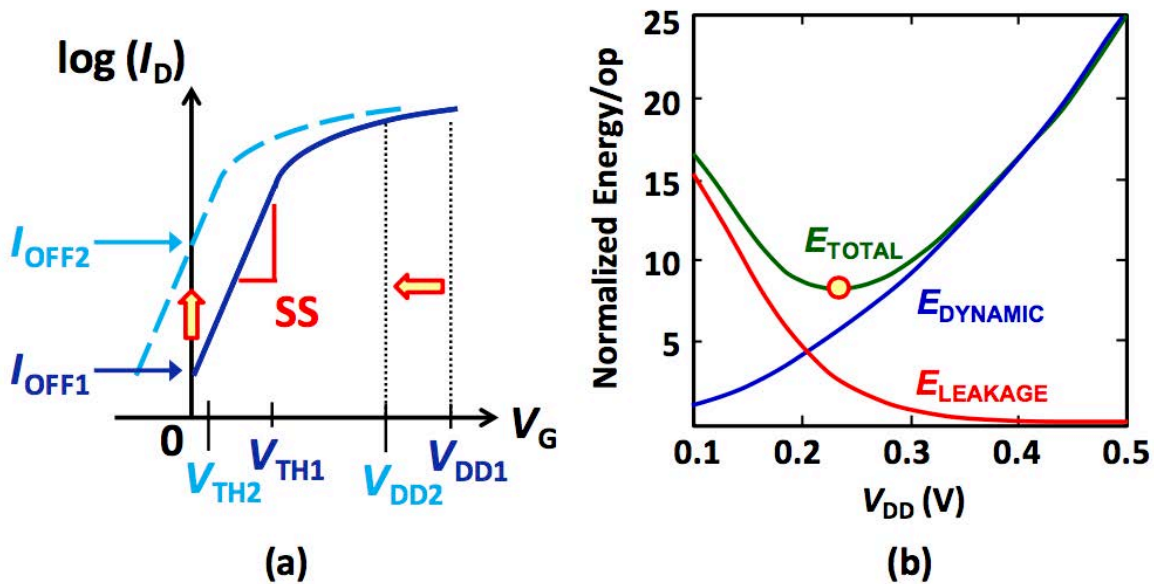
Figure 1-13. (a) $\log(I_D)$-V_G plot of a n-channel MOSFET showing the effect of lowering V_{TH} and V_{DD} and its (b) energy per operation implications. Adapted from [86].

The 60 mV/dec fundamental limit of subthreshold swing, known as the Boltzmann tyranny, poses a power crisis for the future of MOS transistors. This bottleneck can be overcome using a mechanical switch, which shows abrupt switching from off to on-state. Hence, these mechanical

switches do not cause any static energy dissipation. Figure 1-14 shows the transfer characteristics of a mechanical switch and its implication with V_{DD} scaling.

The concept of MEMS makes it possible to make an on-chip electromechanical switch using microfabrication techniques [87]. Figure 1-15 shows the operation of a typical electromechanical switch and its transfer characteristics. In the off-state, the suspended cantilever (source terminal) is separated from the drain terminal and there is no current flowing through the device. To turn the device on, an electrostatic force exerted between the gate and the source terminal pulls the suspended source terminal downwards to make contact with the drain terminal. The gate voltage at which the source cantilever touches the drain terminal, turning the device on, is called the pull-in voltage (V_{PI}). MEMS switches inherently show hysteresis. The gate voltage at which the source cantilever gets released from the drain terminal is called the release voltage (V_{RL}). Note that the hysteresis voltage sets the lower limit of the relay voltage scaling.

Both three and four terminal microelectromechanical (MEM) relays fabricated using the microfabrication technique have been demonstrated with on resistance of ~10 kΩ, mechanical delay of ~10 ns, and ~10^9 on/off switching cycle [87]–[90]. Spencer et al. demonstrated MEM relay based VLSI circuits and predicted that relay-based adders in a 90 nm technology node can achieve energy savings of ~10x over a minimum-energy-point CMOS design for up to 20 MOPS [91].
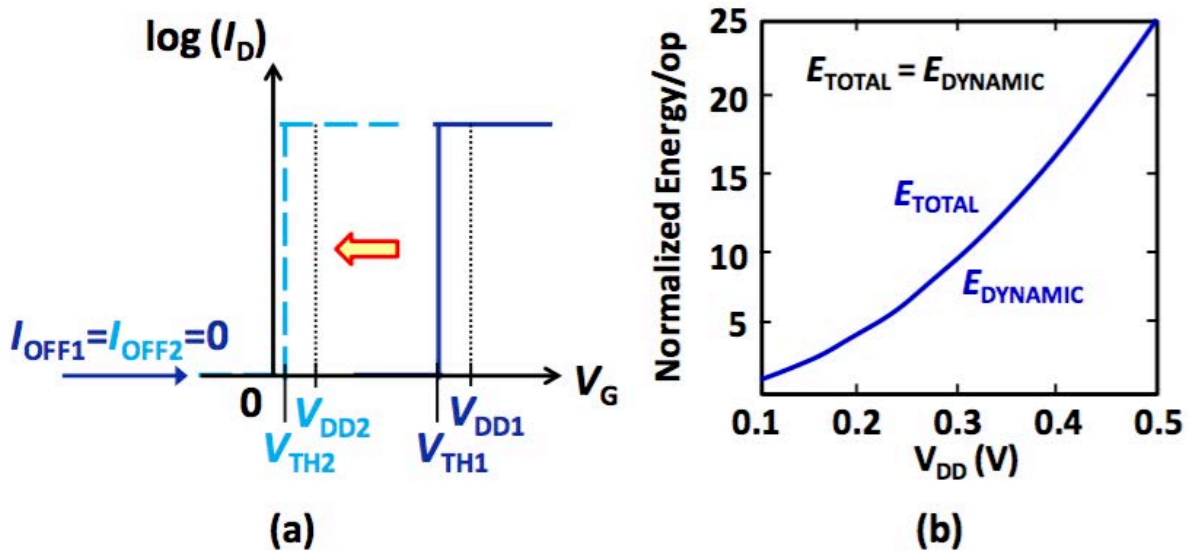
Figure 1-14. (a) log(I_D)-V_G plot of a mechanical switch showing the effect of lowering V_{TH} and V_{DD} and its (b) energy per operation implications. Adapted from [86].
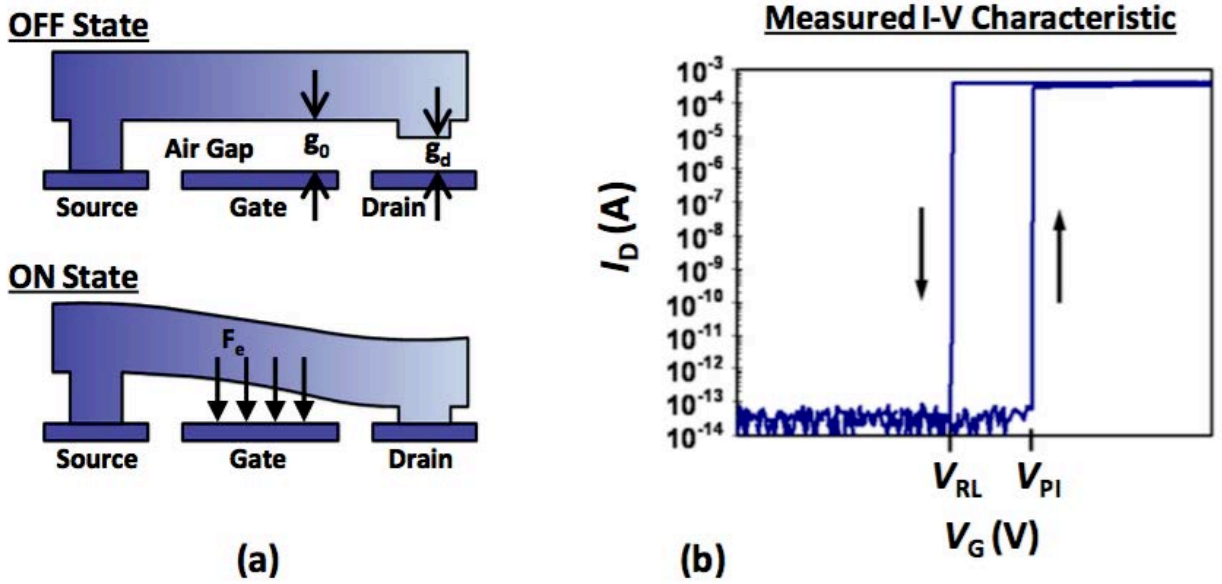
Figure 1-15. (a) Schematic of a typical 3-Terminal relay structure in the off-state and the on-state and (b) its usual log(I_D)-V_G characteristic, showing the pull-in (V_{PI}) and release (V_{RL}) voltages. Adapted from [86].

To design MEMS devices, proper understanding of the physics of electrostatic actuation of suspended mechanical structure is very important. An electrostatically actuated beam can be modeled as a parallel plate capacitor on a mass-spring-damper system. In the next section, we review the underlying physics of such systems.

1.3.2 Electrostatic Actuation of the Mass-Spring-Damper System

Figure 1-16 shows a basic illustration of the electrostatic actuation of the mass-spring-damper system containing a fixed electrode and a movable electrode. The movable electrode is modeled as a mass-spring-damper system and the motion dynamics are expressed as

$$m\ddot{z} + b\dot{z} + kz = F_{elec}(z),$$ Eq. 1-1

where z is the displacement, m is the mass, b is the damping factor, and k is the spring constant of the movable electrode. F_{elec} is the electrostatic force between the two electrodes applied with a voltage V.
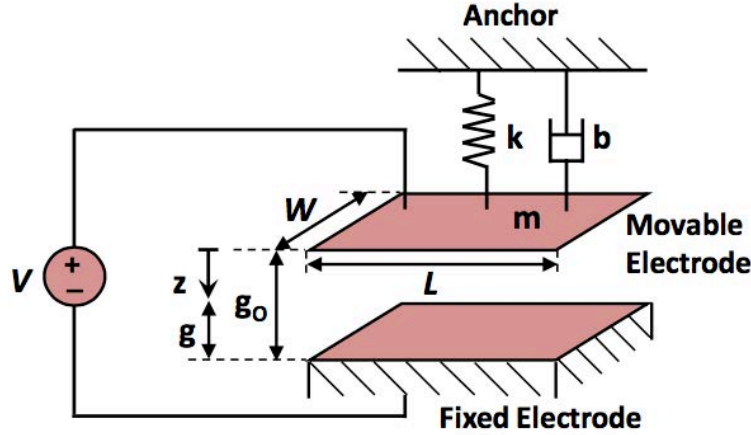
Figure 1-16. Electrostatic actuation of a basic mass-spring-damper system.

Modeling this system with a simple parallel plate capacitor, the electrostatic force can be expressed as

$$F_{elec} = \frac{\varepsilon_0 W L V^2}{2(g_0 - z)^2} = \frac{\varepsilon_0 W L V^2}{2g^2}.$$ Eq. 1-2

Here, g is the actuation gap, g_0 is the as fabricated actuation gap, W and L is the width and length of the actuation area, respectively.

The spring restoration force, which opposes the electrostatic actuation is

$$F_{spring}(z) = kz = k(g_0 - g)$$ Eq. 1-3

At equilibrium, the spring restoration force balances the electrostatic force:

$$\frac{\varepsilon_0 W L V^2}{2g^2} = k(g_0 - g)$$ Eq. 1-4

F_{elec} increases superlinearly with displacement, while F_{spring} increases linearly with displacement. Therefore, beyond a certain displacement, F_{elec} is always greater than F_{spring}, and the system becomes unstable. Using stability analysis of Eq. 1-4, it can be shown that this critical displacement occurs when the electrode moves 1/3 of g_0. After this critical displacement, the movable electrode abruptly snaps into the fixed electrode with the slightest increase in actuation voltage. The voltage at which this phenomenon occurs is defined as the 'pull-in' voltage (V_{PI}) where,

$$V_{PI} = \sqrt{\frac{8kg_0^3}{27\varepsilon_0 WL}}$$

This voltage actuation of the mass-spring-damper system is the basic building block of the MEMS relays. If MEMS relays can be processed using printing techniques, they can be used as high-performance switching devices in large-area electronics. Printing of MEMS structures is a very new technology, whose history goes back only about a decade.

1.4 Evolution of Printed MEMS

The field of printed MEMS has evolved to utilize all the benefits of MEMS as a device technology and printing as a low-cost and large-area process technology. The first endeavor to fabricate printed MEMS devices was made by Fuller et al. in 2002 [92]. They inkjet-printed metallic inks formed from gold nanoparticles at ~300 ^{0}C platen temperature to make an additively built three-dimensional structures without employing any sacrificial layer; and demonstrated resonant inductive coil, linear and rotary electrostatic-drive motors and vertical electrothermal actuators. They also realized the necessity of using a sacrificial layer for the fabrication of planer vertical electrothermal actuators. Poly(methyl methacrylate)(PMMA), patterned using a draw-down bar, was used as the sacrificial layer. Wilhelm et al. demonstrated actuators to modulate light employing an offset liquid embossing technique [93]. Solution-processed nanoparticles were used as the structural material. Polyimide was used as the sacrificial material and etched using oxygen plasma. Nakano et al. employed inkjet-printing and a NC cutting machine to fabricate MEM switches with an operating voltage of ~70 V [94], [95]. They inkjet-printed silver nanoparticles as control electrodes on two polyimide substrates. A NC cutter processed adhesive film was sandwiched between the two polyimide films containing the control electrodes. Parylene was coated on one control electrode to avoid any short between the two control electrodes. Via-holes were formed by a punching machine and signal electrodes were inkjet-printed with silver nanoparticles ink. A similar fabrication approach was employed to fabricate a complementary MEM switches from the same research group, where a cantilever-type polyimide beam was placed in between two actuating electrodes [96]. The demonstrated MEM switch showed an operating voltage of ~60 V with switching delays in the range of few milliseconds. Although these works successfully demonstrated printed MEM switches, a great deal of manual assembling was involved in the process which may limit the processability. Lam et al. demonstrated an inkjet-printed cantilever as a structural material [97]. PMMA was inkjet-printed and smoothed with solvent vapor annealing. A PMMA barrier was created on two sides of the sacrificial layer to form a mold-like structure. Silver nanoparticles ink was inkjet printed inside the mold and any undesired rims were trimmed using a laser trimmer. They also implemented an accelerometer structure using this technique. This work showed a repeatable inkjet-printed process flow excluding any manual processing and provided a very important improvement in printed MEMS. However, they used laser trimming to define the cantilever beam after the completion of printing. Also, the fabricated

cantilever structure did not show any functionality due to the lack of an integrated actuation component. Figure 1-17 shows the images of different attempts to make printed MEM structure.

(a)

(b)

(c)

(d)
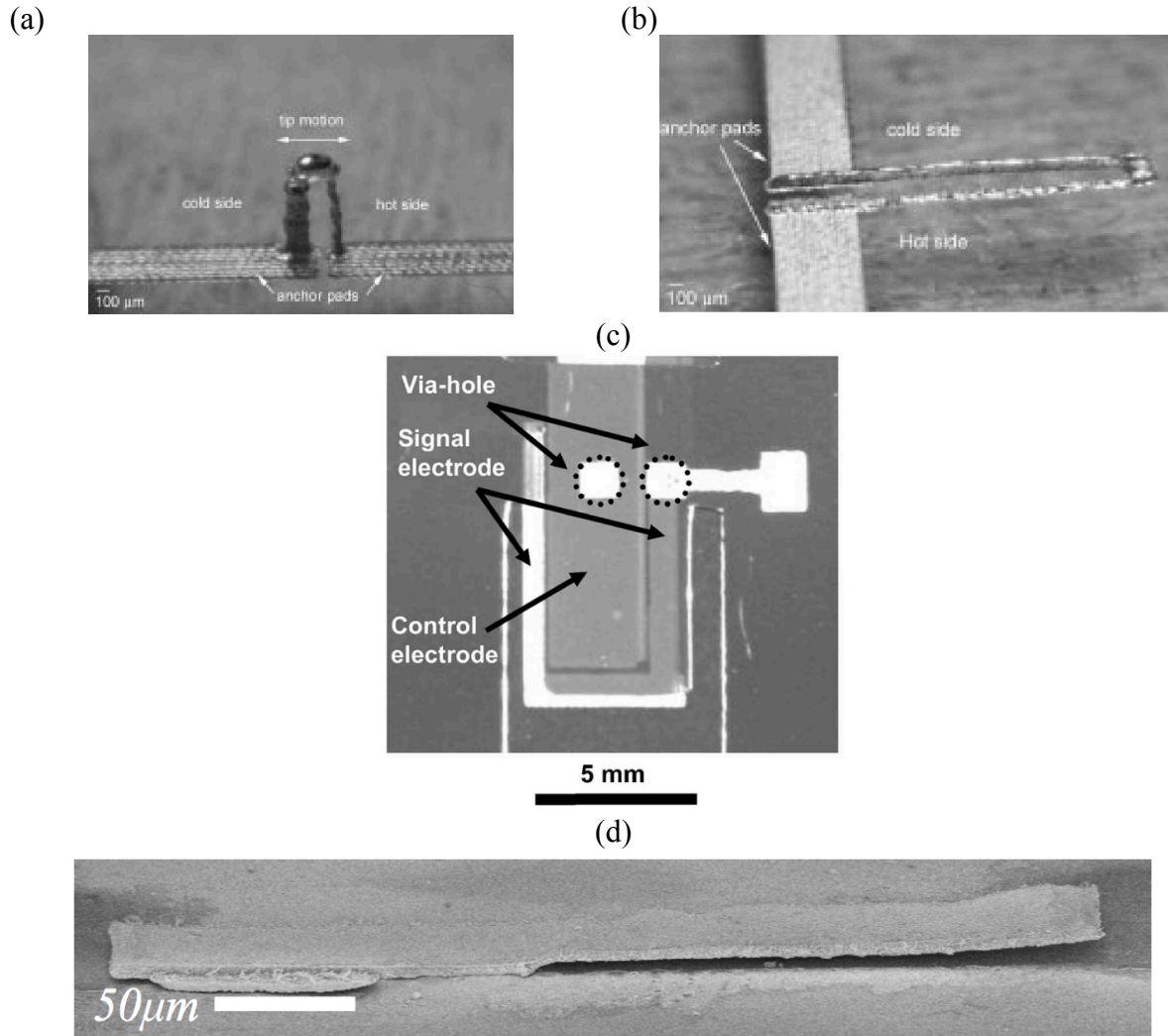
Figure 1-17. Three dimensional (a) vertical and (b) planar thermal actuators fabricated using inkjet-printing of gold nanoparticles ink at high platen temperature [92]. (c) MEM switch fabricated using inkjet-printing and NC cutter tools [94]. (d) Cantilever fabricated using inkjet-printed silver nanoparticle ink and laser trimming [97].

Recently, Park et al. and Chung et al. demonstrated functional MEM relays with well-controlled inkjet-printing and spin coating technique, which showed a realistic route towards the application of printed MEMS for large-area electronics [19], [21]. Figure 1-18 illustrates a three terminal MEM relay by Park et al. and four terminal MEM relay by Chung et al. with inkjet-printed

21

electrodes and structural materials. These relays use a spin coating technique to deposit the gate dielectric and sacrificial layer. Anchor regions were etched by inkjet-printing the appropriate solvents and a two-step beam and anchor printing was employed. Although the previously reported printed MEM relays showed superior performance in terms of very low on state resistance (R_{ON}) and minimal off current (I_{OFF}), their not-fully-printed process flow leads to poor area scalability. Moreover, these structures are vulnerable to stress variations in the printed cantilevers that can cause the suspended beam to curl up, which increase device-to-device variability. For these reasons, an improved fully printed process flow is required to process stress-tolerant MEM relays. A major portion of this dissertation will focus on the process development and characterization of fully printed MEMS relays for large area electronics.

(a)

(b)
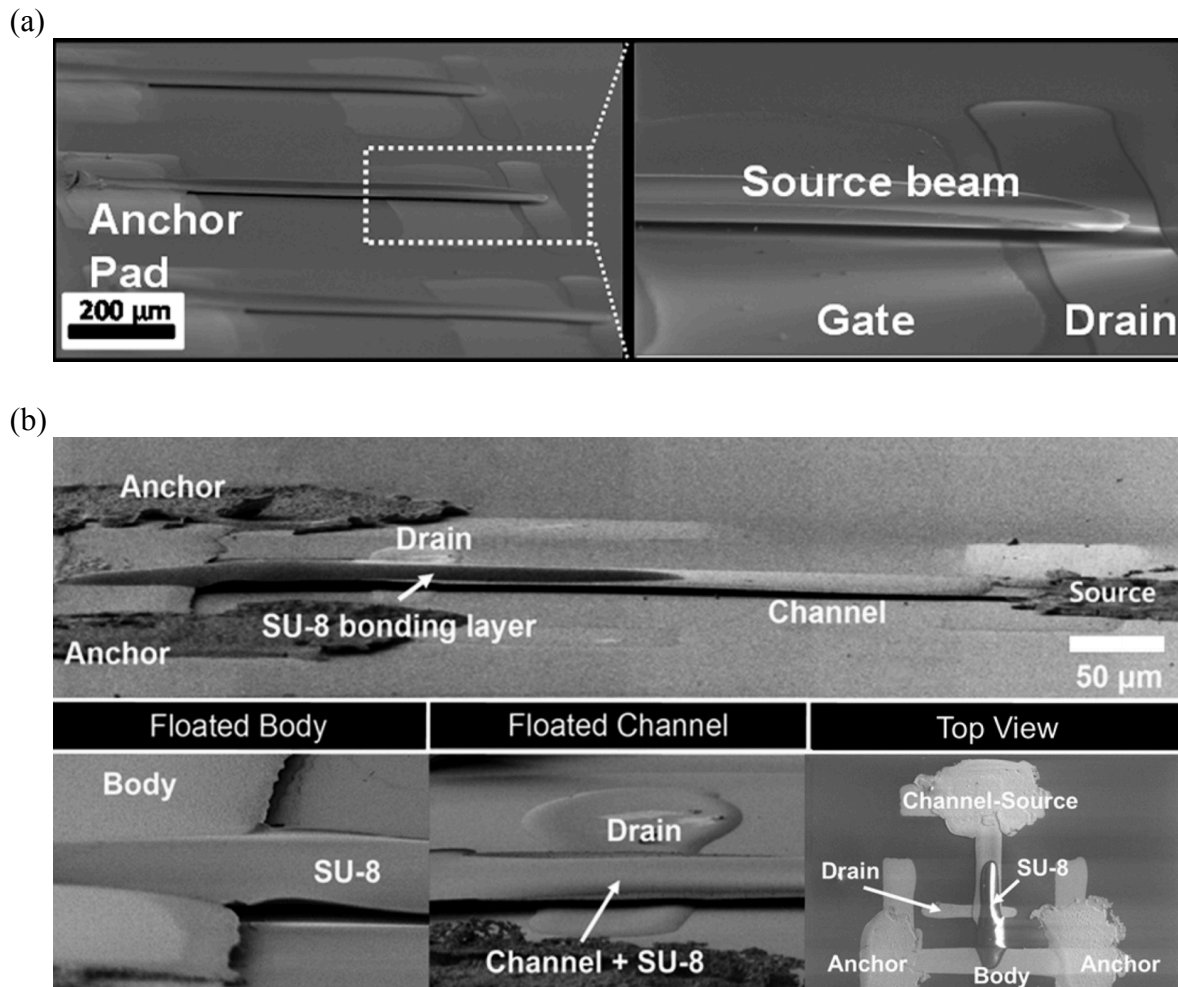
Figure 1-18. Inkjet-printed MEM relays. (a) Three terminal [19] and (b) four terminal relays [20]. Structures were inkjet-printed using silver nanoparticles ink. Poly(methyl methacrylate) (PMMA) sacrificial layers were spin coated.

Printed MEMS relays are particularly interesting for the possibility of their use as pixel switching devices in large-area displays Good understanding of the operational principle of high-performance display technologies is necessary to realize the usefulness of printed MEMS relays as pixel switching device. Therefore, in the next section, a review of major display technologies including the performance requirements for the switching devices used in display backplanes is provided.

1.5 Display Technologies

Displays are an essential component of portable electronic devices, as displays act as an interface to convey information between human and machine. There are three main display technologies for modern electronic appliances: liquid crystal display (LCD), organic light emitting diode (OLED), and electrophoretic display (EPD). Currently, all of these display technologies have an active matrix of thin film transistors (TFTs) in the backplane for precise control of the display pixels [98]–[106].

An archetypal Active-Matrix Liquid Crystal Display (AMLCD) includes a backlight source, a first polarizer, a TFT array with liquid crystal, a color filter and a second polarizer (Figure 1-19(a)). The operation principle of AMLCD is as follows. AMLCD requires a backlight, typically LEDs or fluorescent tubes. The first polarizer polarizes the backlight into a single orientation. The liquid crystal is used to rotate the polarization of the light by 90^0. The TFTs control the liquid crystal alignment by changing the electric field across the liquid crystal and determine the polarization state of the light. A color filter is used in each pixel to select the wavelength of white backlight to construct individual red, green and blue sub-pixels. The sub-pixels are used to construct the final color to display. A second polarizer is used, which is orthogonal to the first polarizer. If the light retains the same polarization as transmitted out of the first polarizer, the light will be blocked by the second polarizer. In this case no light passes through and the pixel is in the dark state. The polarization of light passing through the second polarizer must be orthogonal to the light transmitted from the first polarizer for a bright pixel.

Figure 1-19(b) shows the schematic of a pixel consisting of one TFT, a storage capacitor (C_{ST}), and a parasitic capacitor from the liquid crystal (C_{LC}). The gate of the TFTs are connected to the horizontal scan lines that scan the pixels row by row. Pixels are selected by the data lines connected to the drain of the TFTs. TFTs supplies the voltage to charge or discharge the storage capacitor. The voltage stored in the storage capacitor creates an electric field across the liquid crystal. Therefore, the stored voltage in the capacitor determines the brightness of the pixel.

(a)
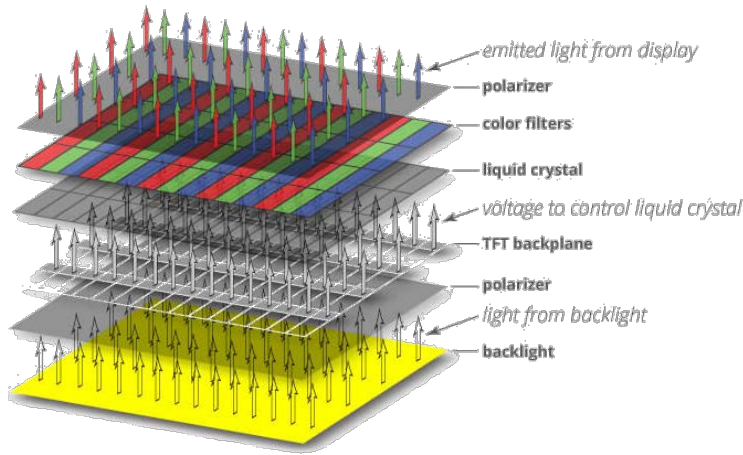
(b)
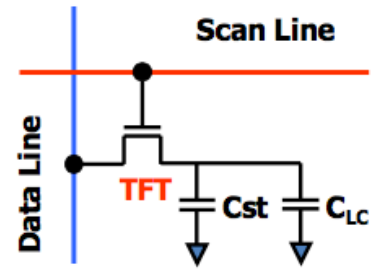
Figure 1-19. (a) Basic architecture of AMLCD. (b) Schematic diagram of AMLCD pixel.

(a)
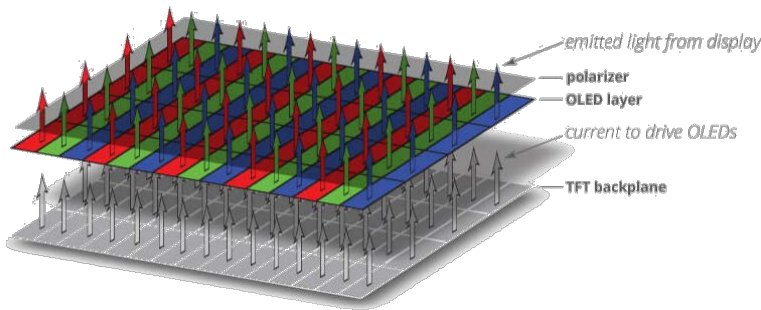
(b)
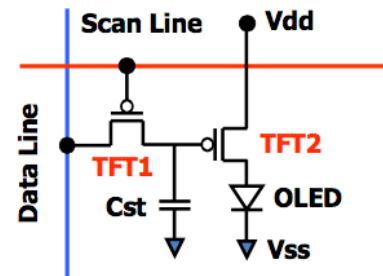
Figure 1-20. (a) Basic architecture of AMOLED. (b) Schematic diagram of AMOLED pixel.

Although AMLCD is a revolutionary flat panel display technology which is used in many portable displays, it has several disadvantages. In AMLCD, light has to pass through several layers before reaching to the human eye. This limits the overall brightness and viewing angle. Moreover, light is blocked by opaque metal layers used for bus lines, TFTs, and capacitors. Therefore, higher

aperture ratio (ratio of the transparent area to the total area) of the pixels are required to maximize the brightness as well as contrast of the AMLCD. Also, the backlight must stay on even while displaying dim images, which makes AMLCD less power efficient.

Active-Matrix Organic Light-Emitting Diode (AMOLED) is a relatively new display technology for portable devices. In contrast to the AMLCD technology, AMOLED is a self-emitting technology, which means it does not require any backlight. AMOLED has the advantages of higher contrast, wider viewing angle and faster response time. AMOLED displays are inherently simpler and have only two main layers: An OLED (organic light-emitting diode) layer that emits light, and a backplane made of TFT (thin-film transistor) circuits that provide current to the OLEDs, thereby controlling their brightness. Usually, a polarizer is also used to cut reflected lights. Figure 1-20(a) shows the basic architecture of the AMOLED display, comprising an AMTFT backplane and OLED components. The OLED typically consists of an electron transport layer, an organic emitter, and a hole injection layer. In an AMOLED pixel, TFT1 and the storage capacitor function similar to those in AMLCD to control the voltage storage in the pixel (Figure 1-20(b)). The stored voltage is then applied to the gate of TFT2, which acts as a controlled current source. The light emission of the OLEDs is controlled by controlling the current through TFT2. The brightness of the OLED is directly proportional to the current through TFT2.
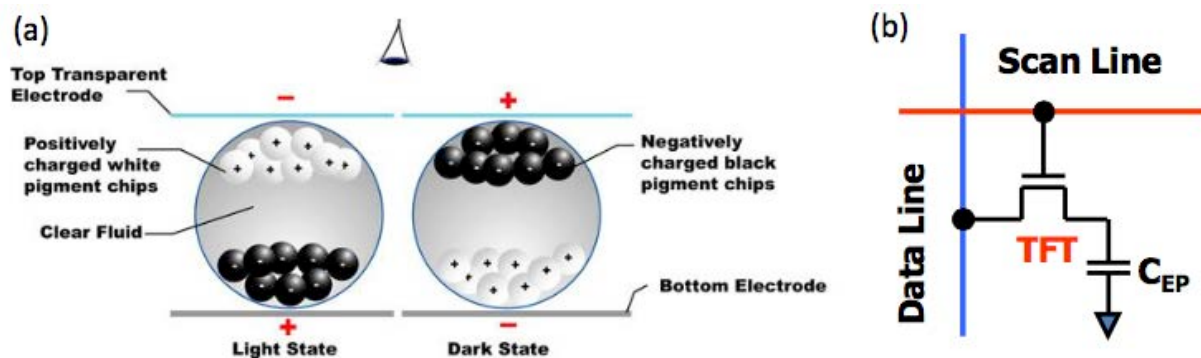
Figure 1-21. (a) Electrophoretic display. (b) Schematic diagram of AMEPD pixel.

Apart from AMLCD and AMOLED displays, Active-Matrix Electrophoretic Displays (AMEPD) are also gaining interest as this type of display mimics the appearance of ordinary printed paper using reflected daylight instead of a backlight or light emitting component. EPD can be read under direct sunlight and requires no power to maintain the display content, making it the most promising technology for E-book applications. Figure 1-21(a) shows the cross-sectional structure of the EPD, which is composed of millions of microcapsules sandwiched by two parallel electrodes. Each microcapsule contains positively charged (white) and negatively charged (black) pigment chips suspended in a clear liquid. The top electrode is transparent and the presence of white or black

pigment chips near the top electrode determines the state of the pixels. The charged pigment chips are moved through the liquid by applying appropriate electric field across the pixel. The simple operation of EPD results in a pixel with only one TFT that controls the electric field applied across the pixels (Figure 1-21(b)). However, EPD technology has a very low refresh rate compared to LCD and OLED. This limits their implementation in very large displays and in sophisticated interactive applications such as fast-moving menus, mouse pointers or scrolling etc.

AMLCDs are, by far, the most commercially important flat panel display technology; and the use of AMOLEDs are growing rapidly. Although OLED technology is inherently better performing than the LCD technology, in both of these technologies, display performance largely depends on the performance of the pixel switching devices. High-quality display technologies require a high brightness display with good contrast, darkest blacks and no flickering. To meet these requirements, the pixel switching devices needs to have very high on current (I_{ON}) and low (ideally zero) off-state current (I_{OFF}). High on/off ratio (I_{ON}/I_{OFF}) of more than 10^7 ensure finer shades of grayscale. Zero or very low I_{OFF} also provides low power displays. Also, a low-cost and large-area processing technique is required. Today's active matrix backplanes have mainly three categories of semiconductor based TFTs: amorphous silicon (a-silicon), poly-silicon and solution-processed transparent organic or inorganic TFTs. Amorphous Silicon is used in most of the commercial AMLCD displays due to its low variability, good operational stability and lower processing cost than poly-silicon TFTs. However, a-Silicon has low mobility and hence TFTs made with a-silicon show low on current. The on current of a-silicon TFT meet the requirements for AMLCDs, but it cannot meet the requirement of the high brightness AMOLED displays. Poly-silicon TFTs provide the high on current required for AMOLED displays. But the cost of processing poly-silicon TFTs are higher than a-silicon TFTs. Also, there is higher variability associated with poly-silicon TFTs. In recent years, solution-processed organic and inorganic TFTs have gained huge attention due to their potential low cost processing and compatibility with flexible substrates. Moreover, the transparent nature of these TFTs increases the pixel aperture ratio, which is very important for high brightness displays.

Although extensive research on solution processed TFTs over the last decade has improved their performance significantly [107]–[119], further improvements in power consumption, on/off current ratio, sub-threshold swing, and environmental stability are still required for a broader range of applications. Moreover, fully printed TFTs show degraded performance due to the poorer quality of printed semiconductors and dielectrics compared to their conventional counterparts [119], [120]. An alternative approach is microelectromechanical (MEM) relays with movable cantilevers operated by electrostatic actuation. These provide a solution for ultra-low leakage devices with hyper-abrupt switching, excellent subthreshold swing, and very low on-resistance. Considering all the benefits of MEM relays over printed TFTs, printed MEM relays have been proposed as a new switching devices for large-area displays [19]–[21]. To realize MEMS relays as pixel switching devices in display backplanes, a fully printed process flow needs to be developed. Moreover, stress generation in printed thin films poses a bottleneck to print MEMS

relays. This dissertation presents novel architectures and fully printed process flows for stress-tolerant three and four terminal MEMS relays including materials and device characterization.

1.6 Thesis Organization

In this thesis, several aspects of printed MEMS will be discussed including the characterization of structural materials, development of process flow and device characterization. In chapter 2, the choice of materials for a fully inkjet-printed MEMS processes will be discussed. This includes the choice and printability of electrodes and structural materials, dielectric materials, and sacrificial materials. A detailed study of polymer ink formulation and pattering will also be presented. The release process of structural materials will also be discussed including the solution to avoid stiction of movable structures. Chapter 3 will discuss the mechanism of stress gradient development in the inkjet-printed films formed from sintered silver nanoparticles through elemental and mechanical analysis of the film. Chapter 4 will discuss the first demonstration of the fully inkjet-printed stress-tolerant three terminal MEM reed relay including process development and device characterization. This chapter will also discuss about the modeling and scaling of the three terminal reed relay. Chapter 5 will introduce a fully printed four terminal relay including the process development and device characterization. Chapter 6 will conclude the thesis and outline the potential future of printed MEMS.

Chapter 2:   Materials for Inkjet-Printed MEMS Processing

Any microelectromechanical system requires structural materials to be deposited on a sacrificial material, followed by a release step using wet or dry etching of the sacrificial material. A dielectric material is also required for any electrical isolation. In this chapter, the choice of these materials for printed MEMS and their processing conditions will be discussed.

2.1 Materials for Structures

In conventional MEMS, poly-silicon is the most widely used structural material. Since printed MEMS seeks for a printable material that can be processed at a plastic compatible low-temperature, poly-silicon is not a viable material. Various low-temperature compatible polymer materials including dielectric and transparent conductive oxides can be printed as structural materials. However, many MEMS applications utilize electrostatic force exerted through capacitive coupling between a fixed electrode and a movable structure. Therefore, a highly conductive metallic structure is the most attractive choice for MEMS devices. Fortunately, highly conductive metals such as silver, gold and copper can be printed using nanoparticle based inks.

To formulate conductive inks, metallic nanoparticles, coated with polymers or organic ligands, are dispersed in organic solvents. After deposition of the ink using inkjet-printing, a sintering step is required to form the metallic film. The printed ink is usually sintered on a hot-plate. In the initial phase of sintering, the solvents evaporate; then the ligands get detached from the nanoparticles surface and out-diffuse. In the final stage of the sintering, the nanoparticles come close to each other and go through coarsening to form a film. Figure 2-1 illustrates the mechanism of sintering of the nanoparticles based ink. Various commercial silver nanoparticles based inks e.g. CCI-300 from Cabot Corp., EMD 5603 from Sun Chemicals, EMD 5730 from Sun Chemicals, DGP 40LT-15C from ANP etc. are used to inkjet-print silver films. All of these silver films require a curing temperature of less than 150 ^{0}C. Both CCI-300 and EMD 5603 have a silver mass loading of 15-20 wt%, EMD 5730 has a mass loading of ~40 wt % and DGP 40LT-15C has a mass loading of 30-35 wt%. CCI-300, EMD 5603 and EMD 5730 contains alcohol based solvent, and DGP 40LT-15C contains ether based solvent (Triethylene glycol monoethyl ether).

Figure 2-2 shows optical micrograph of a printed silver film using CCI-300 ink and its thickness profile. CCI-300 ink, printed with 25 μm drop spacing and sintered at 150 ^{0}C, produces ~400 nm thick films with a sheet resistance of 0.2 Ω/sq.
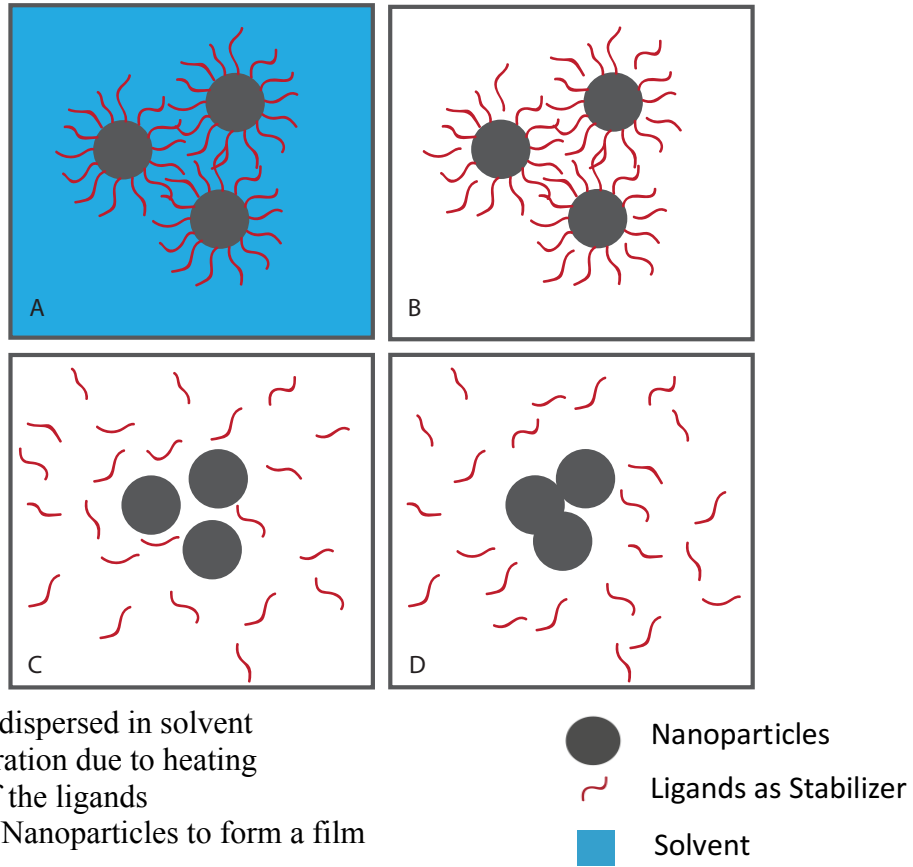
A: Nanoparticles dispersed in solvent
B: Solvent evaporation due to heating
C: Detachment of the ligands
D: Coarsening of Nanoparticles to form a film

- Nanoparticles
- Ligands as Stabilizer
- Solvent

Figure 2-1. Sintering mechanism of nanoparticles based ink.

(a)

(b)
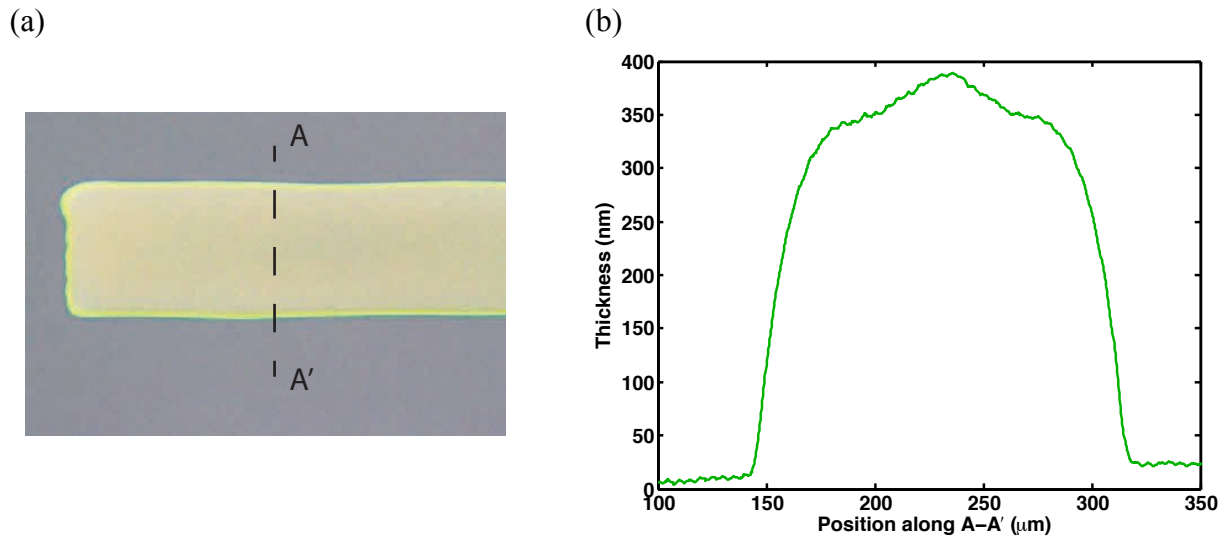
Figure 2-2. (a) Inkjet-printed silver line using ~20 wt% silver ink and (b) its thickness profile

Nanoparticle based silver inks require a curing temperature in the range of 100-150 ^{0}C to produce highly-conductive films. Note that, the decomposition temperature of the ligands used in these inks are above 250 ^{0}C. Therefore, the formation of conductive films does not need complete decomposition of the ligands. In fact, some studies show that residual ligands help in the coarsening of the nanoparticles [121], [122]. Also note that, nanoparticles do not need to melt to undergo coarsening. The melting temperature of silver nanoparticles with 30 nm diameters is ~500 ^{0}C. Therefore, melting point depression of nanoparticles due to increased surface to volume ratio is not the main process of nanoparticle coarsening. Rather, coarsening mostly happens due to solid state diffusion. However, a volume compaction occurs during the sintering process of the constrained films, which induces an average tensile stress in the film. Also, a gradient of tensile stress, generated across the thickness of printed films, forces the suspended structures to curl. This curling of suspended structures introduces difficulties to realize MEMS relays. The mechanism of the development of stress gradient in printed thin films is discussed thoroughly in Chapter 3. Chapter 4 and Chapter 5 present fully printed process flows for three and four terminal MEMS relays, respectively, both of which provide excellent tolerance against the stress variations in printed films.

In a typical MEMS process, dielectric materials provide electrical isolation among conductors. For example, in three terminal MEMS relays, a dielectric material is necessary to isolate the fixed gate electrode from the movable source electrode.

2.2 Dielectric Materials

A dielectric material is a substance that is a poor conductor of electricity, but an efficient supporter of electrostatic field. An ideal dielectric material has perfect electrical insulation capability. The quality of a dielectric material is determined by its "dielectric strength". For a specific configuration of dielectric material and electrodes, dielectric strength refers to the minimum applied electric field that results in breakdown. After breakdown dielectrics lose their insulating properties and become electrically conductive. A measurement of dielectric strength is necessary for proper design of MEMS devices. For a fully printed MEMS process, use of solution processed dielectric materials is necessary. Additionally, the dielectric materials should not lose its dielectric strength during further processing steps.

Various solution processed polymer materials including Poly(4-vinyl phenol) (PVP), Poly(vinyl alcohol) (PVA), Poly(methyl methacrylate) (PMMA), Polyvinylidene fluoride (PVDF), CYTOP^{TM} etc. have been used as the dielectric materials for the electronic devices [107], [123]–[129]. Among these dielectric materials, cross-linked PVP shows highly reliable dielectric performance. Also, it shows strong etch resistivity to most solvents, which is very important for further processing steps. A dielectric solution can be prepared by dissolving Poly-4(vinylphenol) (PVP) (10 wt%) powder in propylene glycol methyl ether acetate (PGMEA) solvent, with

poly(melamine-co-formaldehyde) (2 wt %) as a cross-linking agent (CLA). This dielectric solution can be deposited using spin coating technique. A 2000 rpm spin coating of this cross-linked PVP solution produces a film thickness of ~500 nm after cross-linking for 30 min on a 180 ^{0}C hot plate. Figure 2-3 shows the profile of a trench made on spin coated PVP sample to measure the thickness of PVP layer.

The breakdown characteristics of cross-linked PVP was measured using a crossbar capacitance structure. A silver bottom electrode was inkjet-printed on oxidized silicon wafer followed by the spin coating of PVP layer. After that, a top silver electrode was inkjet printed to fabricate the metal-insulator-metal (MIM) crossbar capacitance structure. Figure 2-4 shows that the minimum breakdown field for the cross-linked PVP dielectric is more than 1.3 MV/cm, which is good enough for most electronic devices.

To measure the etch resistance of the cross-linked PVP dielectric layer during further processing steps, different treatment processes were performed on the spin coated PVP layer. These treatment processes include dipping the PVP layer in Anisole for 30 min (Process B), dipping PVP layer in N-Methyl-2-pyrrolidone (NMP) for 30 min (Process C), dipping PVP layer in N-Methyl-2-pyrrolidone (NMP) for 30 min followed by the sample drying process in critical point drying (CPD) tool (Process D), dipping PVP layer in N-Methyl-2-pyrrolidone (NMP) for 30 min followed by another dip in acetone for 10 min and after that the sample drying process in CPD tool (Process E). CPD is a widely used sample drying technique in MEMS process. CPD operation will be discussed in detail in section 2.4.2. Figure 2-5 shows that the minimum breakdown field does not decrease with anisole treatment, but does decrease with NMP and CPD treatment. However, the drop observed in the minimum breakdown field is also not very high. After treatment process E, the PVP dielectric still delivers a minimum breakdown field of ~ 1.15 MV/cm, which is sufficient for most MEMS applications.

For the fully printed MEMS process, the inkjet-printable PVP ink was prepared by dissolving Poly-4(vinylphenol) (PVP) (12 wt%) powder in 1-Hexanol solvent, with poly(melamine-co-formaldehyde) (1 wt %) as a cross-linking agent. Inkjet-printed PVP dielectric shows similar electrical performance of spin coated PVP.

In surface micromachined MEMS processes, the structural layer is deposited on top of a sacrificial layer which is removed or etched out to create the necessary void in the thickness direction for the fabrication of suspended structures. Unlike bulk micromachining process, here, the structures are built on top of the substrate and not inside it. Therefore, the properties of the substrates in this process are not very important and a variety of substrates including glass and plastic can be used. Proper combination of structural and sacrificial materials is extremely important to ensure their processing compatibility and etching orthogonality.
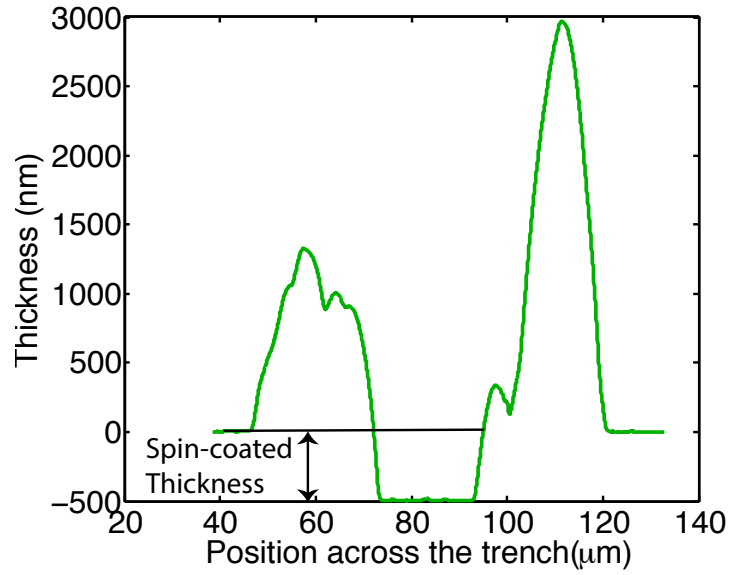
Figure 2-3. Measurement of spin coated thickness of PVP dielectric using contact profilometry.
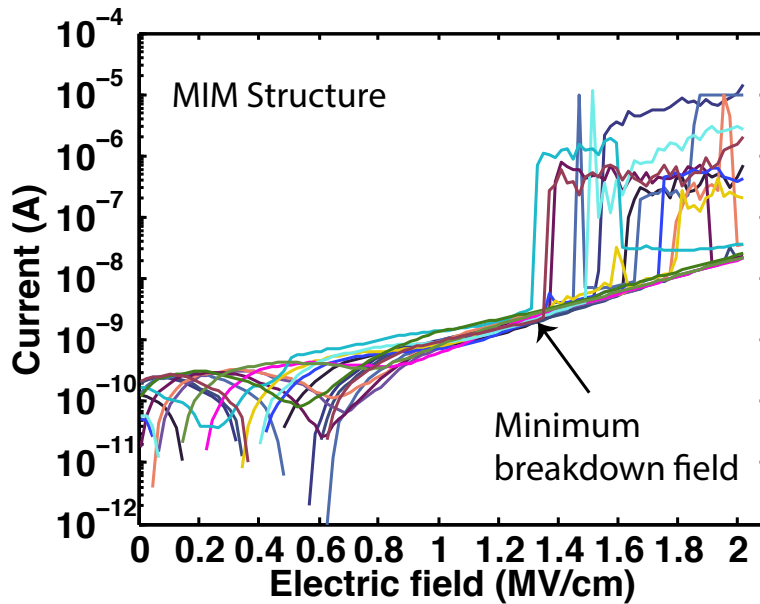
Figure 2-4. Breakdown voltage characterization of cross-linked PVP using crossbar Metal-Insulator-Metal (MIM) structure.

PVP treatment	Process ID
Untreated	A
Dipped in Anisole for 30 min	B
Dipped in NMP for 30 min	C
Dipped in NMP for 30 min + CPD	D
Dipped in NMP for 30 min + Dipped in Acetone for 10 min + CPD	E
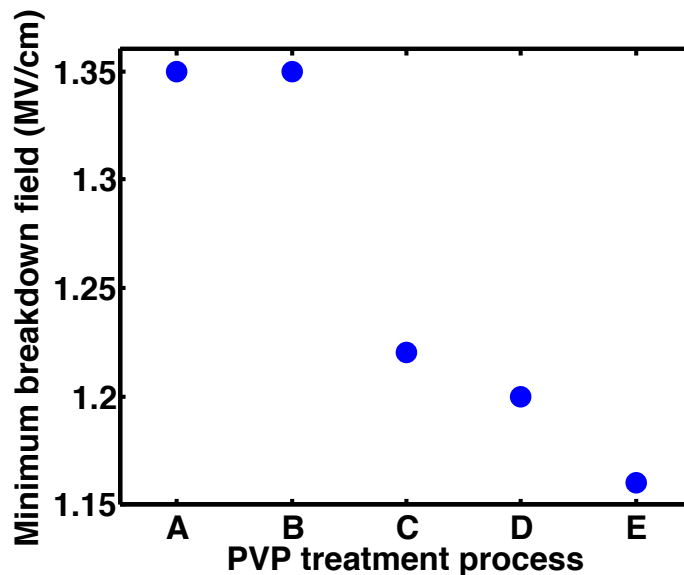
Figure 2-5. Reliability of PVP dielectric with different solvent treatment and drying process.

2.3 Materials for Sacrificial Layer

A set of candidate materials, listed in Table 2-1, were investigated to be used as the sacrificial layer in printed MEMS. These materials were primarily chosen for their solution processing capabilities and low curing temperatures. Solution processing capability of materials is necessary for their printability. Printable sacrificial layers ensure better area scalability of MEMS devices. Low curing temperatures allows the use of variety of substrates such as glass, plastics etc. The selection of the sacrificial material was further narrowed down based on their compatibility with the structural layer. Sacrificial materials should be compatible with the processing of MEMS structures formed from nanoparticles based silver ink. Also, the sacrificial layer should be easily removable with the appropriate solvent without damaging the structural materials. PVA and SU-8

show good performance, PMMA shows moderate performance and solgel derived ZnO shows poor compatibility with the silver structural materials processing. PVA and SU-8 become very robust after processing and hence they are very difficult to remove. Solgel ZnO can be removed using diluted HCl and PMMA can be easily removed using acetone. Considering these facts, PMMA is chosen for the sacrificial layer for printed MEMS.

Sacrificial Materials	Solution Processing Capability	Compatibility with silver structure processing	Removability /Etching
PVA	Yes	Very good	Very difficult to remove
Solgel ZnO	Yes	Poor	Removable (HCl)
SU-8	Yes	Very good	Very difficult to remove
PMMA	Yes	Moderate	Easy to remove with Acetone

Table 2-1. Choice of sacrificial materials for printed MEMS.

PMMA is a positive photoresist. It is widely used in photolithography process. Commercially available PMMA solutions use a high molecular weight PMMA solute, which is not suitable for inkjet-printing. Therefore, a systematic investigation for the formulation of PMMA ink considering various PMMA solvents and molecular weights is necessary.

2.3.1 PMMA Ink Formulation for Inkjet-Printing

A study on the inkjet-printable PMMA ink formulation was carried out for printed sacrificial layer in MEMS processing. There are several key parameters of concern to design inkjet-printable ink. Choosing the right molecular weight (MW) of the solute is very important for designing jettable ink. Lower MW solutes are ideal for jettable ink, since higher MW solutes have longer polymer chains and hence are not suitable for jetting drops out of the nozzle. The recommended surface tension and viscosity of the ink are ~10 cPs and 33 dynes/cm respectively. Also, the solvents used to prepare the ink should have a high boiling point and low vapor pressure to avoid nozzle clogging. Table 2-2 presents the physical properties of various solvents for PMMA ink and their effect on the clogging rate of inkjet nozzle. The high boiling point (202 ^{0}C) and low vapor pressure (0.0316 kPa at 20 ^{0}C) of NMP solvent ensures stable jetting by reducing the probability of nozzle clogging (see Figure 2-6).

Solvents	Boiling point (^{0}C)	Surface Tension (dynes/cm^2)	Viscosity (cP) @20^{0}C	Vapor Pressure (kPa) @20^{0}C	Nozzle Clogging
Toluene	111	28.40	0.59	3.786	Frequent
Acetone	56	25.20	0.3311	14.6	Frequent
Anisole	153	28	1.40	1.1	moderate
NMP	202	40	1.7	0.133	Rare

Table 2-2. Physical properties of various solvents for PMMA and their effect on the nozzle clogging rate.
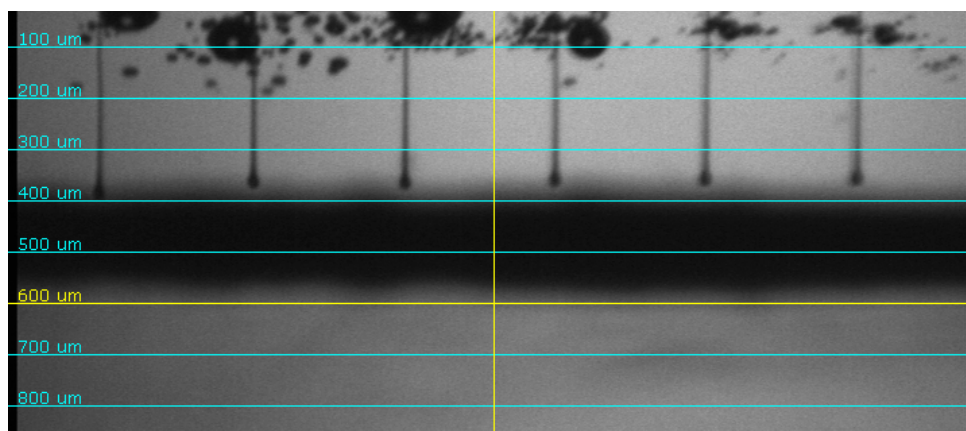
Figure 2-6. Image from the drop watcher camera of the Fujifilm Dimatix materials printer (DMP-2831) showing reliable jetting of PMMA ink using NMP solvent.

The rheology of inkjet printing inks must be well controlled in order to be able to jet droplets. In most cases, appropriate rheology for inkjet printing means low viscosity at high shear rates. Allowable range of viscosity for inkjet compatible inks is lower than inks used in other printing techniques. This limits the maximum allowable mass loading for inkjet printable ink. In general, inks with low solute mass loading results in a highly non-uniform deposition due to a phenomenon known as coffee ring effect.

2.3.2 Coffee Ring Effect

Coffee ring is a known effect in inkjet printing. Coffee ring effect can easily occur when the jetted drop completely wets the surfaces. The coffee ring effect was first explained by Deegan et al.

[130]. To explain coffee ring effect, let's consider a droplet of solution. The evaporation rate of the solvent is higher near the edge of the drop than the interior due to the higher surface to volume ratio near the edge. The evaporated solvent near the edge is replenished by the solvent from interior. This creates an outward capillary flow which carries almost all the solute near the edge of the drop (see Figure 2-7). Various methods have been employed to reduce the coffee ring effect. It has been shown that reducing the substrate temperature helps to reduce coffee ring effect [58]. A cooler substrate reduces the evaporation rate near the edge more than the evaporation rate near the middle of the drop. A highly effective method to reduce the coffee ring effect is to utilize the Marangoni flow that develops in co-solvent systems [131]. In this technique, a co-solvent with higher boiling point and a lower surface tension than the primary solvent is added to the primary solvent. Due to a higher evaporation rate, the solvent compositions near the edge of the drop become mainly the solvent with high boiling point. Therefore, the solvent near the edges has a lower surface tension than in the middle. This results in a surface tension gradient, which creates an inward Marangoni flow. This inward Marangoni flow opposes the initial outward capillary flow and reduces the coffee-ring effect [132].
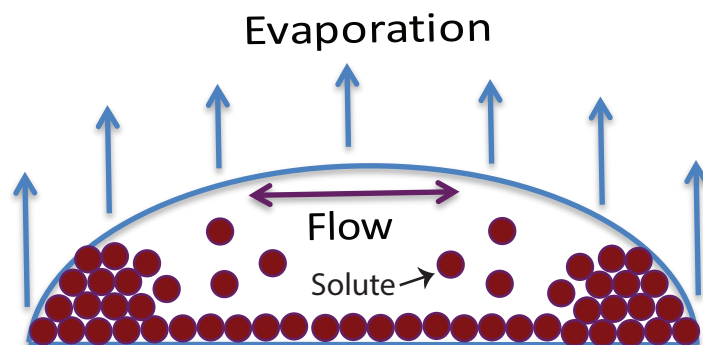
Figure 2-7. Coffee ring effect. Outward capillary flow caused by the different edge to center evaporation rate of the solvent carries almost all the solutes near the edges of the drop.

Coffee ring effect is prominent in an ink system with low mass loading. An ink formulated with higher molecular weight solute is difficult to jet and delivers a reduced amount of maximum jettable mass loading. The low jettable mass loading of high MW PMMA causes a huge coffee ring in the printed pattern (see Figure 2-8). The MEMS structure printed on this non uniform sacrificial layer will introduce weak anchor points. To print coffee-ring-less sacrificial layers, a low molecular weigh PMMA is used to increase the maximum jettable mass loading. Table 2-3 shows the maximum mass loading window for reliable jetting of PMMA inks with different

molecular weights of PMMA. A 15 wt% mass loading of 15kDa MW PMMA dissolved in NMP solvent is used as the ink for sacrificial layer.

PMMA MW (kDa)	Jettable mass loading (wt%)
495	<1
120	<3
15	5-18

Table 2-3. Jettable mass loading window of inks with different molecular weight of PMMA solute.
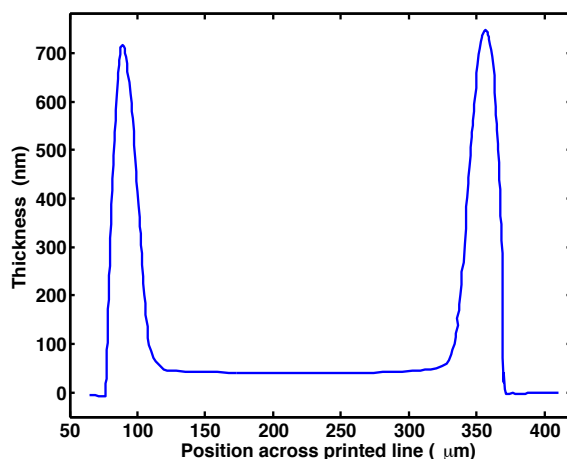
Figure 2-8. Coffee ring observed in the pattern printed using an ink formulated with 1 wt% mass-loading of 495 kDa PMMA.

The coffee ring effect produces tall peaks near the edges and a much thinner valley in the printed lines. If the coffee ring effect is not minimized, MEMS structures printed on this non uniform sacrificial layer will suffer from weak anchoring. Therefore, printing a smooth sacrificial layer is necessary. Although higher jettable mass loading of low molecular weight PMMA helps to reduce coffee ring effect, an experiment considering the printed drop spacing and printing passes is required for optimizing the thickness uniformity of the sacrificial layer.

2.3.3 Patterning a Uniform Sacrificial Layer

To pattern the PMMA sacrificial layer, inkjet-printing was performed using a Fujifilm Dimatix materials printer (DMP-2831) with a Fujifilm Dimatix cartridge delivering a 10 pL droplet volume.

A single pass PMMA ink printing creates a dome shaped sacrificial pad due to the high surface tension of NMP solvent (40 dynes/cm at 20 ^{0}C) while a three-pass printing results in a coffee-ring pattern (see Figure 2-9).

(a)   (b)
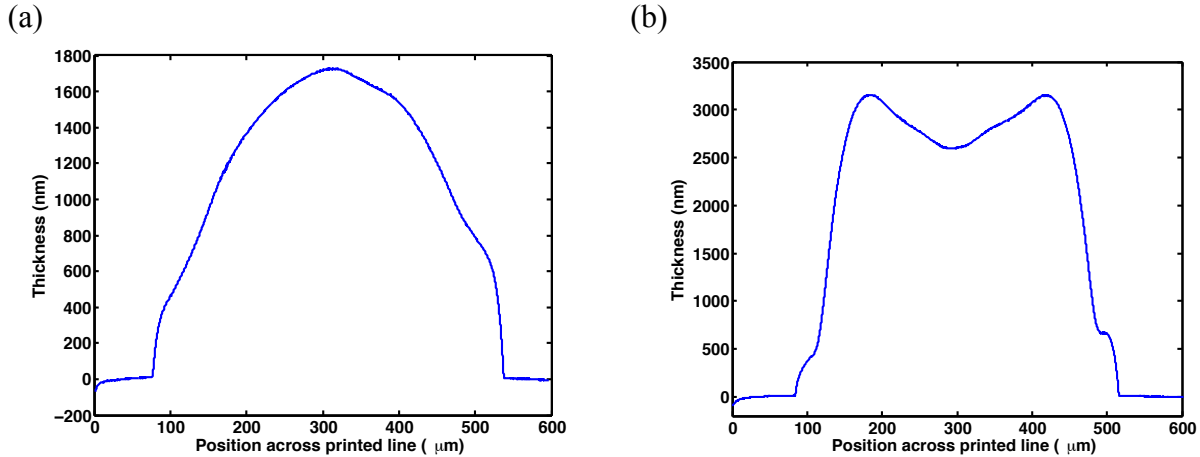
Figure 2-9. (a) Dome-shaped thickness profile of single-pass printed PMMA. (b) Coffee ring pattern in three-pass printed PMMA

Due to this shift in thickness profile from dome shaped to coffee ring, the edge to midpoint thickness ratio is used as the uniformity metric. For a uniform pattern, the edge to thickness ratio has to be close to unity. Figure 2-10(a) shows the variation in the edge to thickness ratio with increasing printing passes. Less than 2-pass printing of PMMA shows an edge to midpoint thickness ratio of less than 1, which indicates a dome-shaped pattern. On the other hand, increasing the printing passes over 2 passes increases the edge to midpoint thickness ratio illustrating an increasing coffee ring. Increasing the spacing of inkjet drops can reduce coffee-ring patterns in multi-pass printed sacrificial pads (see Figure 2-10(b)). A fairly uniform PMMA sacrificial pad with a midpoint thickness of 2.2 μm and an edge-to-midpoint thickness ratio of 1.16 was inkjet-printed exploiting 3-pass printing and a drop spacing (DS) of 35 μm while placing the substrate on a 32 ^{0}C platen; printing was followed by thermal cross-linking on a 180 ^{0}C hotplate for 10 min (see Figure 2-10(c)). Besides reducing the cost of materials used, the printed PMMA sacrificial layer also simplifies MEMS structure fabrication by replacing the previously reported two step anchor and beam-printing process [19], [21] with a single printing step.
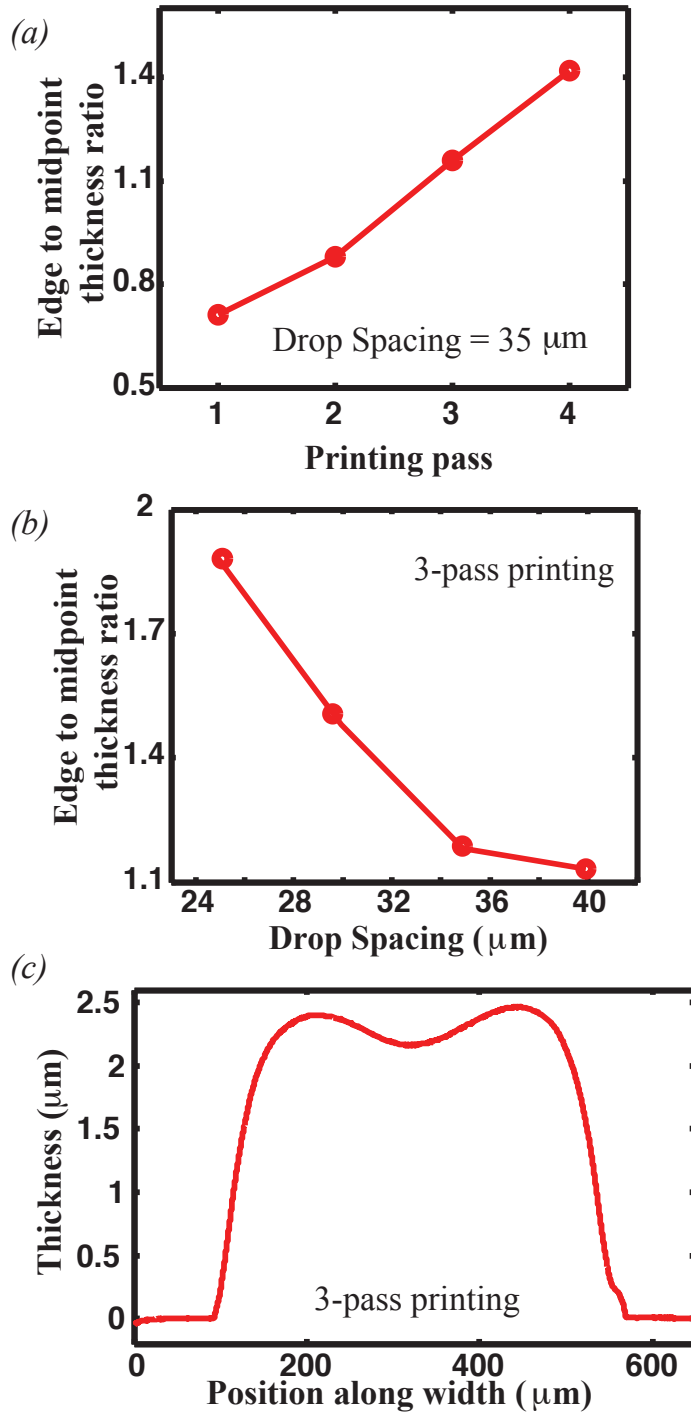
Figure 2-10. Optimization of the PMMA sacrificial layer printing. (a) Increase in edge to midpoint thickness ratio with printing passes (b) Increasing the drop spacing reduces the edge to midpoint thickness ratio and hence decreases the coffee ring effect. (c) A fairly uniform thickness profile for inkjet-printed PMMA using a 3-pass printing and a drop spacing of 35 µm.

Selective etching of the sacrificial layer is the final and one of the most important process steps in MEMS. The sacrificial layer can be etched using isotropic dry or wet etching techniques. Dry etching of PMMA is possible by using a plasma asher, but this significantly damages the silver structural layer. Therefore, wet etching of PMMA using acetone, followed by a drying step, is used to remove the sacrificial layer. The released structures can be collapsed during the drying step due to a phenomenon known as stiction.

2.4 Release of Printed MEMS Structure

2.4.1 Stiction

Stiction is the most important failure mechanism for surface micromachined MEMS [133]–[135]. Stiction is the sticking of the MEMS structure to the substrate (see Figure 2-11). Due to surface forces such as capillary forces, hydrogen bridging, electrostatic forces, van der Waals forces etc. suspended structures come in contact with the substrate. Once contact is made, the high adhesion force due to the high contact surface area between the structure and the substrate makes it almost impossible for the spring restoring force to bring the structure back to its original suspended position. Among the surface forces, the capillary force created during the drying process of liquid etchant is the strongest one.
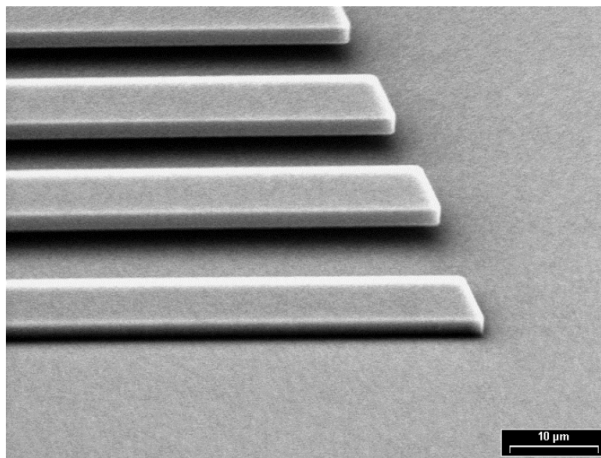
Figure 2-11. Stiction failure of cantilever beams. Image taken from reference [133]
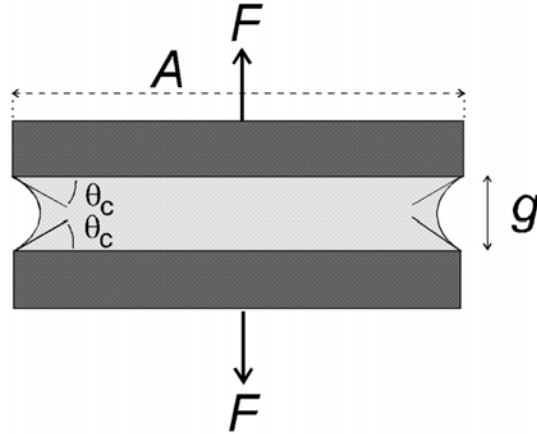
Figure 2-12. A thin layer of liquid working as an adhesive between two plates. A force
F is applied to maintain equilibrium.

Figure 2-12 shows the mechanism of the formulation of this capillary force. A thin layer of liquid
in between two solid plates acts as an adhesive. If the contact angle between the liquid and the
solid (θ_c) is less than 90^0, pressure inside the liquid becomes lower than outside. This creates a net
attractive force between the plates. If F is the force applied to the plates to maintain the
equilibrium, then it can be expressed as

$$F = \frac{2A\gamma_{la}\cos\theta_c}{g}$$
Eq. 2-1

where A is the wetted area, γ_{la} is the surface tension of the liquid to air interface and g is the liquid
layer thickness.
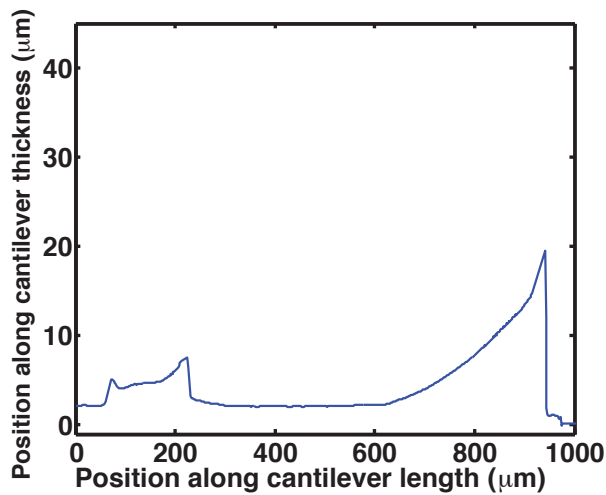
Figure 2-13. Partial collapsing of a printed cantilever beam due to stiction.

It is clear from $F = \dfrac{2A\gamma_{la}\cos\theta_c}{g}$

Eq. 2-1 that a lower surface tension value of the etching solvent can reduce the surface capillary force and reduce the possibility of stiction. However, even using a very low surface tension organic solvent such as acetone and 2-propanol (IPA) does not completely eliminate stiction of printed MEMS structures (see Figure 2-13). The stiction issue can be eliminated by limiting the direct transition of liquid phase into the gas phase during the drying process. This can be achieved by using critical point drying technique.

2.4.2 Critical Point Drying

Critical point drying is one of the most useful and reliable technique to process stiction-free MEMS. The etching solvent is replaced by liquid CO_2 in a drying chamber. The temperature and pressure of the drying chamber is controlled such that the sample dries through a supercritical state. Figure 2-14 shows the simplified phase diagram of CO_2 and temperature and pressure control for the supercritical drying. When the liquid crosses the boundary from liquid to gas, the liquid changes into gas at a finite rate and stiction happens. Therefore, in the critical point drying process, this crossing from liquid to gas is avoided. The drying chamber is first cooled at less than 10 ^{0}C and filled with liquid CO_2. During the purging step, all the liquid etching solvent is replaced by liquid CO_2 and the temperature and pressure of the chamber is controlled such that CO_2 enters in a supercritical state. In the bleed stage, supercritical CO_2 exits the chamber leaving the sample in dried state.
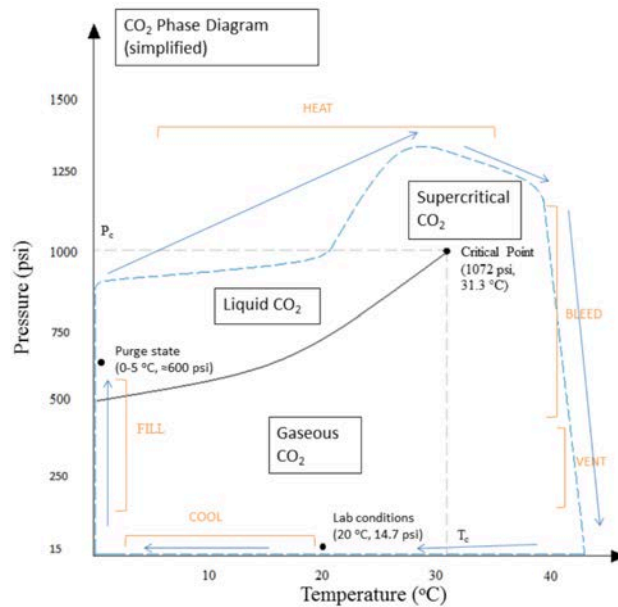
Figure 2-14. Simplified phase diagram of liquid CO_2 showing the critical point drying process.
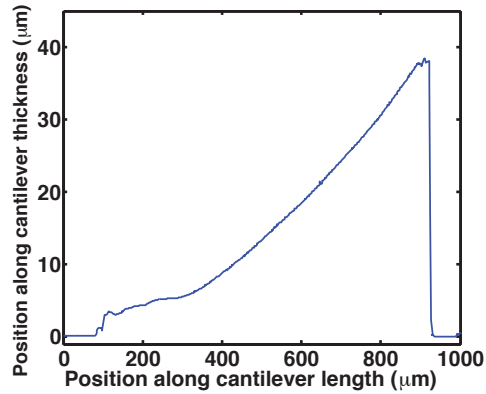
Figure 2-15. Stiction free cantilever processing using critical point drying.

Process layers for MEMS	Selected materials for processing	Processing and performance highlights
Structure	Silver (nanoparticles based ink)	- Inkjet- printing. - Sintering on hotplate. - Low sintering temperature of < 150 ^{0}C. - Low sheet resistance of < 0.5 Ω/sq.
Dielectric	Poly-4(vinylphenol) (PVP)	- Inkjet-printing. - Cross-linking at 180 ^{0}C on hotplate. - Sufficient dielectric strength of ~ 1.3 MV/cm. - Robustness to subsequent processing.
Sacrificial	Poly(methyl methacrylate) (PMMA)	- Inkjet-printing. - Ink formulation: 15 wt% 15 kDa MW PMMA dissolved in NMP solvent. - 35 μm drop spacing and 3-pass printing for smooth sacrificial layer. - Annealing at 180 ^{0}C on hotplate. - Moderate robustness to subsequent processing. - Easily removable with acetone.

Table 2-4. Selection of materials for MEMS including their processing and performance highlights.

A MEMS structure printed on the PMMA sacrificial layer can be etched by dipping the sample in an acetone bath kept at 40 ^{0}C. The sample is then washed in IPA, which replaces all the acetone. The sample containing the MEMS structure immersed in IPA is the transferred to critical point drying chamber for stiction-less drying (see Figure 2-15).

In this chapter, choices of structural, dielectric and sacrificial materials for printed MEMS and their printability are discussed. Table 2-4 presents selection of materials for MEMS including their processing and performance highlights. MEMS structures are constructed using conductive patterns, which can be achieved by inkjet-printing of nanoparticle based silver inks followed by a sintering step. Various commercial silver inks, such as CCI 300, EMD 5603, EMD 5730 and DGP 40LT-15C, deliver highly conductive films (sheet resistances of < 0.5 Ω/sq) at a low sintering temperature (< 150 ^{0}C). Dielectric materials require good dielectric strength and robustness to subsequent processing. Inkjet-printed PVP has a dielectric strength of 1.3 MV/cm and good tolerance to further processing steps, making it a suitable dielectric material for most printed MEMS applications. For the sacrificial material, PMMA is selected for its printability, adequate compatibility to the processing of silver structure and good etching orthogonality to silver. A PMMA ink is carefully designed for stable jetting performance and coffee-ring free printing of the sacrificial layer. A sacrificial layer suffering from coffee-ring effect is detrimental to MEM structures due to weak anchoring of the suspended structure and variations in the suspended height upon release. Inks with high mass loading show less coffee-ring effect. To increase the jettable mass loading window, low molecular weight (15 kDa) PMMA is used to formulate the PMMA ink. The spacing of ink-jetted droplets and number of printing passes are also optimized for better PMMA thickness uniformity. Wet etching of PMMA using acetone releases silver structures printed on PMMA sacrificial layers. After release, drying the samples in a critical point drying chamber improves the yield of the suspended structures. However, suspended cantilevers formed from nanoparticle based silver inks curl in the upward direction (see Figure 2-15). This occurs due to the stress gradient generated in the structural layer. A proper understanding of the stress gradient generation in printed films is necessary to control or, even, utilize this phenomenon to design MEMS devices. The next chapter investigates the generation of stress gradient in inkjet-printed silver films.

Chapter 3: Stress Gradient in Printed Silver Cantilevers

3.1 Stress Development in the Film Formed from Metallic Nanoparticles: Literature Review

The reduced dimensions of the metallic nanoparticles creates a high surface to volume ratio which alters their physical properties compared to their bulk counterparts [136]. The nanoscale properties and solution processing capability of nanoparticles facilitates the use of technologies such as inkjet, gravure, and screen printing for the patterned deposition of highly conductive film at a low curing temperatures [137]. The use of printed conductive films as electrodes, contacts, interconnects, and antenna assemblies blessed the field of flexible, low-cost and large-area electronics with numerous applications such as radio-frequency identification tags (RFID), photovoltaics, thin film transistors (TFT), organic light emitting diodes (OLED), sensors, diagnostic devices, and electromagnetic shielding [10], [74], [138]–[142]. Recently, inkjet-printing of metal nanoparticles demonstrated three dimensional features such as pillars for packaging and interconnects, and suspended cantilevers for microelectromechanical switches [20], [143], [144]. The most commonly used metals include gold, silver and copper [31], [145], [146]. Silver is the most frequently used material due to its lower cost than gold, high electrical conductivity, and stability against oxidation. To formulate printable ink, metal nanoparticles are dispersed in aqueous or organic solvents and stabilized by encapsulating with either polymer (poly acrylic acid, polyvinylpyrolidone etc.) or low molar mass molecules (long chained thiols and carboxylates etc.) to avoid aggregation of nanoparticles and inkjet nozzle clogging. A curing temperature of well above 200 ^{0}C is required to decompose these stabilizers completely leaving bare nanoparticles behind [147], [148]. It was found that it is not mandatory to decompose the stabilizer completely, because just after detachment from the surface of the nanoparticles, the stabilizer catalyzes the aggregation of the nanoparticles [121], [149]. Above the stabilizer detachment temperature, nanoparticles coalesce through different diffusion mechanisms to achieve a more thermodynamically stable state where the surface-to-volume ratio is minimized [148], [150]. A percolation path is thus generated after the nanoparticles coalesce, which makes the entire deposited film electrically conductive. Therefore, the sintering temperature of an ink is outlined by the detachment of the stabilizers from the surface of the nanoparticles [137], [151], [152]. During the sintering of a thin film on a rigid substrate, the film is constrained in its plane and shrinkage occurs only in the direction perpendicular to the plane of the substrate. Consequently, an in-plane tensile stress develops in the film, which opposes the in-plane shrinkage [153], [154]. The magnitude of the developed tensile stress is proportional to the rate of the shrinkage [155]. A fair amount of analysis on the development of in-plane tensile stress during thermal sintering of metal nanoparticles film is reported in the literature [148], [155], [156]. However, a study on the

stress gradient development across the thickness of nanoparticulate film due to the differential densification rate has not been presented.

3.2 Stress Gradient Induced Curling of Cantilever: Theory

Let's consider the case where a film has an average tensile stress in the film and a positive stress gradient across the thickness of the film where the bottom of the film has less tensile stress than the top of the film. After release, initially the film gets rid of all the average in-plane tensile stress by an in-plane shrinkage of the film. In this state, the bottom of the film has a compressive stress and the top of the film has a tensile stress. The released film relaxes this stresses through a shrinkage in the top of the film and expansion at the bottom of the film. The final curled up beam takes a circular bending profile. The strain gradient developed in the film before release can be expressed as the inverse of the radius of curvature of the beam. A similar curling in a cantilever can be observed in a film with an average compressive stress and a positive stress gradient where the bottom of the film has more compressive stress than the top of the film. Figure 3-1 illustrates the mechanism of the stress gradient induced curling of cantilever.
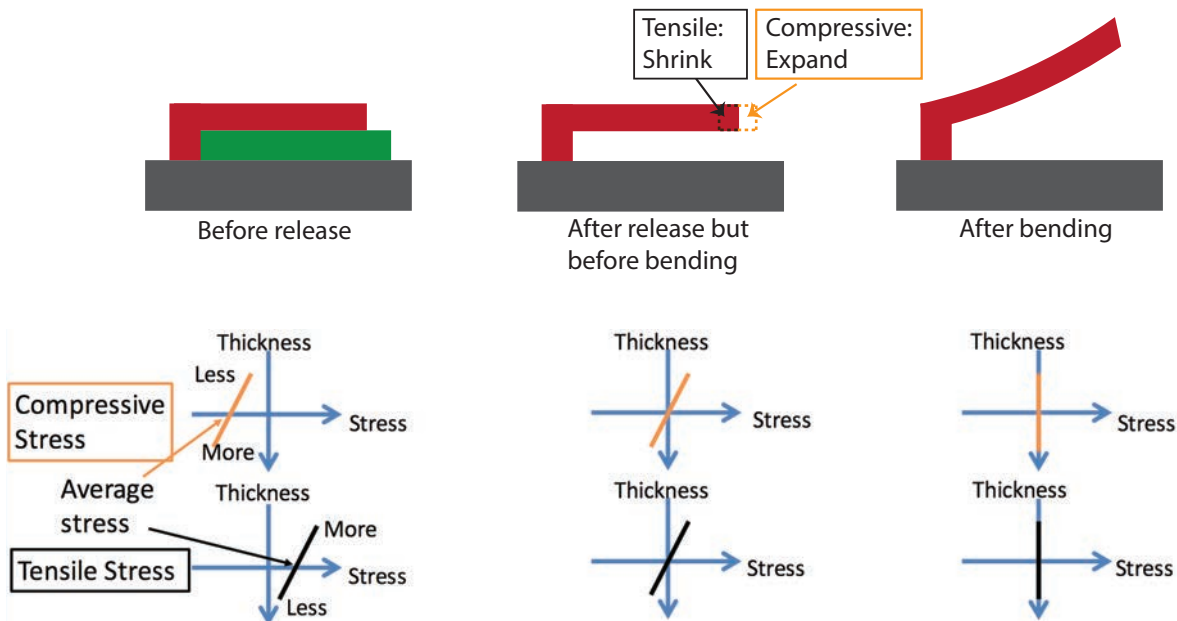
Figure 3-1. Illustration of the stress gradient induced curling of cantilever.

46

3.3 Printed Silver Cantilever: Process Flow
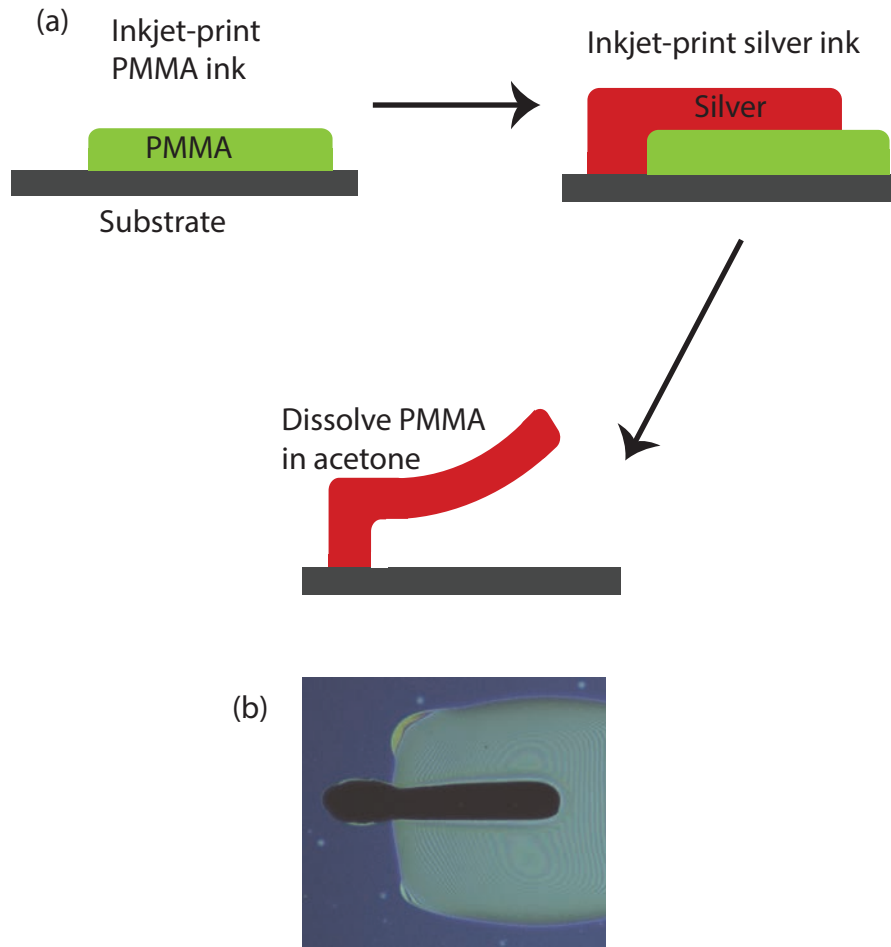
Figure 3-2. (a) Process flow to make inkjet-printed silver cantilevers. Polymethyl methacrylate (PMMA) powder was dissolved in N-Methyl-2-pyrrolidone (NMP) solvent and inkjet-printed on oxidized silicon substrate as the sacrificial layer. A nanoparticles based silver ink (EMD 5730) was inkjet-printed in the same pass to form anchor on the oxidized silicon and beam on the PMMA layer. Multi-pass printing was carried out to get higher beam thickness with interspersed drying. The sample was dipped into acetone bath to dissolve PMMA and release the cantilever. (b) Optical micrograph of an unreleased cantilever.

The development of stress gradients in thin film cantilevers reveals itself through curling of the beam after the removal of the sacrificial layer. A positive stress gradient makes the cantilever curl upward while a negative stress gradient causes the cantilever to curl downward. This cantilever based technique was utilized to measure and analyze the formation of stress gradient in inkjet-printed silver nanoparticles film. A schematic of the fabrication process of the cantilever is illustrated in Figure 3-2. A Fujifilm Dimatix materials printer (DMP-2831) with a Fujifilm Dimatix cartridge delivering a 10 pL droplet volume was used for the patterned deposition of the materials. The sacrificial layer for the cantilever fabrication process was deposited on oxidized silicon substrate by inkjet-printing of Polymethyl methacrylate (PMMA) ink. The PMMA ink was prepared by dissolving 15 wt% low molecular weight (15 kDa) PMMA powder in N-Methyl-2-pyrrolidone (NMP) solvent. PMMA was thermally cross-linked at 180 ^{0}C on a hot plate. A nanoparticle based silver ink (EMD 5730 from Sunchemical Corp.) was inkjet printed on PMMA to deposit the beam and on an oxidized silicon surface to form the anchor in the same printing pass.

EMD 5730 ink contains silver nanoparticles with nominal particle size of 30-50 nm. These nanoparticles are coated with Polyvinylpyrrolidone (PVP) to stabilize them in organic solvent. To realize a suspended cantilever, a multi-pass printing with interspersed drying at 100 ^{0}C for 5 min on a hotplate was used to increase the thickness of the cantilever where each printing pass deposit a ca. 1 μm thick silver layer. Prior to the printing of the EMD 5730 ink, the PMMA surface was treated with 40 W O_2 plasma for 15 sec to improve the ink wettability. The printing process was carried out on a 60 ^{0}C substrate to achieve a better anchor to beam step coverage. After the final printing pass, the printed anchored beam was dried at 110 ^{0}C for 20 min and then sintered at 150 ^{0}C for 15 min on a hot plate with a ramp rate of 5 ^{0}C/min. An optical image of the unreleased cantilever is presented in Figure 3-2(b). The cantilever was released by dissolving the PMMA layer in a hot acetone bath (45 ^{0}C) for 5 min. The acetone was substituted with isopropyl alcohol (IPA) by dipping into a series of IPA baths, and then the sample was dried on a 120 ^{0}C hot plate. The cantilever feels less stiction force during the drying step as the cantilever curls in the upward direction after release creating a high gap between the cantilever and the substrate. For this reason, critical point drying is not necessary to fabricate a suspended cantilever.

3.4 Cantilever Curling Profile

After release, the cantilevers relax the average tensile stress by in-plane shrinkage of the beam. However, the cantilevers bend in the out-of-plane direction to get rid of the stress gradient that develops across the thickness of the film, as shown in Figure 3-3(a). Figure 3-3(b) shows the tip deflection with varying length (*L*) of the cantilever for different printing passes. The thickness of the cantilever increases with accumulated printing passes and consequently increases the stiffness of the beam. Therefore, a cantilever fabricated with more printing passes shows lower tip deflection for the same length of the cantilever.
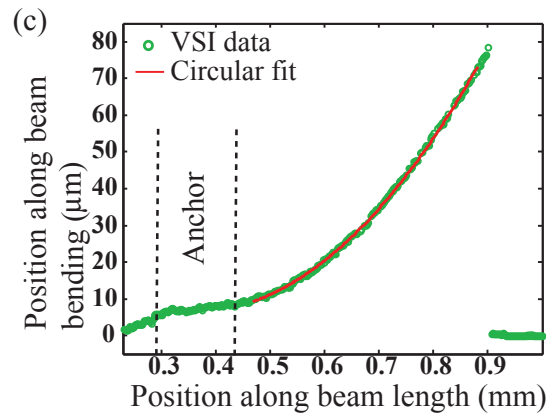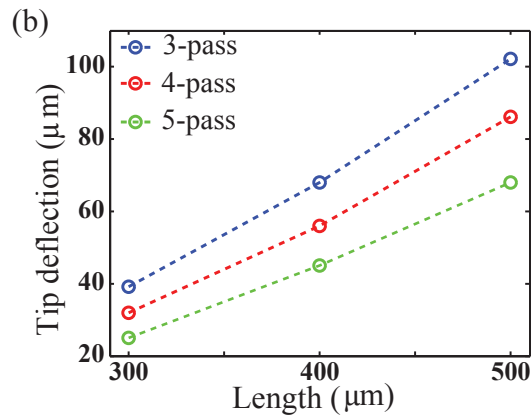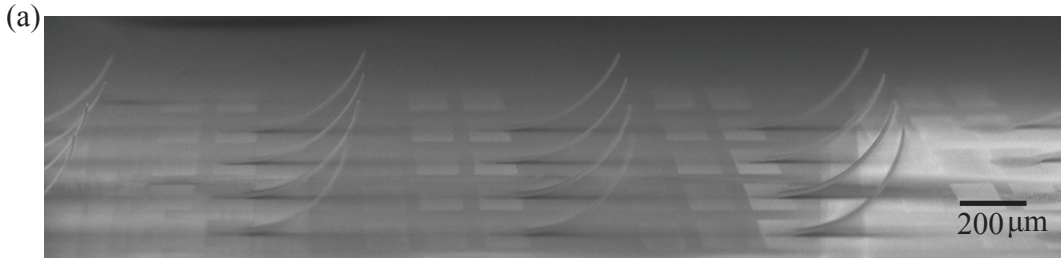
Figure 3-3. (a) Upward curling of the cantilevers formed by exploiting inkjet-printing of silver nanoparticles. (b) Tip deflection with varying length of the cantilever, measured using vertical scanning interferometry (VSI); stiffer beams with higher printing passes enforce less bending of the cantilevers. (c) Circular fit of the cantilever bending profile, obtained from VSI measurement, to extract the radius of the curvature and to subsequently calculate strain gradient.

The out-of-plane bending moment that is generated due to the stress gradient across the thickness of the beam causes the cantilever to curl in a circular manner[157]. Figure 3-3(c) shows the procedure to extract the radius of the curvature of the curled cantilever. Vertical scanning interferometry (Wyko NT3300 profiling system) was used to measure the curling profile of the

49

cantilever. The radius of curvature was extracted by circular fitting of the measured curling profile of the cantilever. Subsequently, the strain gradient that developed across the thickness of the cantilever was calculated from the inverse of the radius of the curvature. For a 5-pass printed cantilever the extracted radius of curvature and the calculated strain gradient is 2.07 mm and 4.83×10^{-4} μm^{-1}, respectively.

3.5 Elemental Analysis of the Printed Silver Film

(a)

(b)

(c)
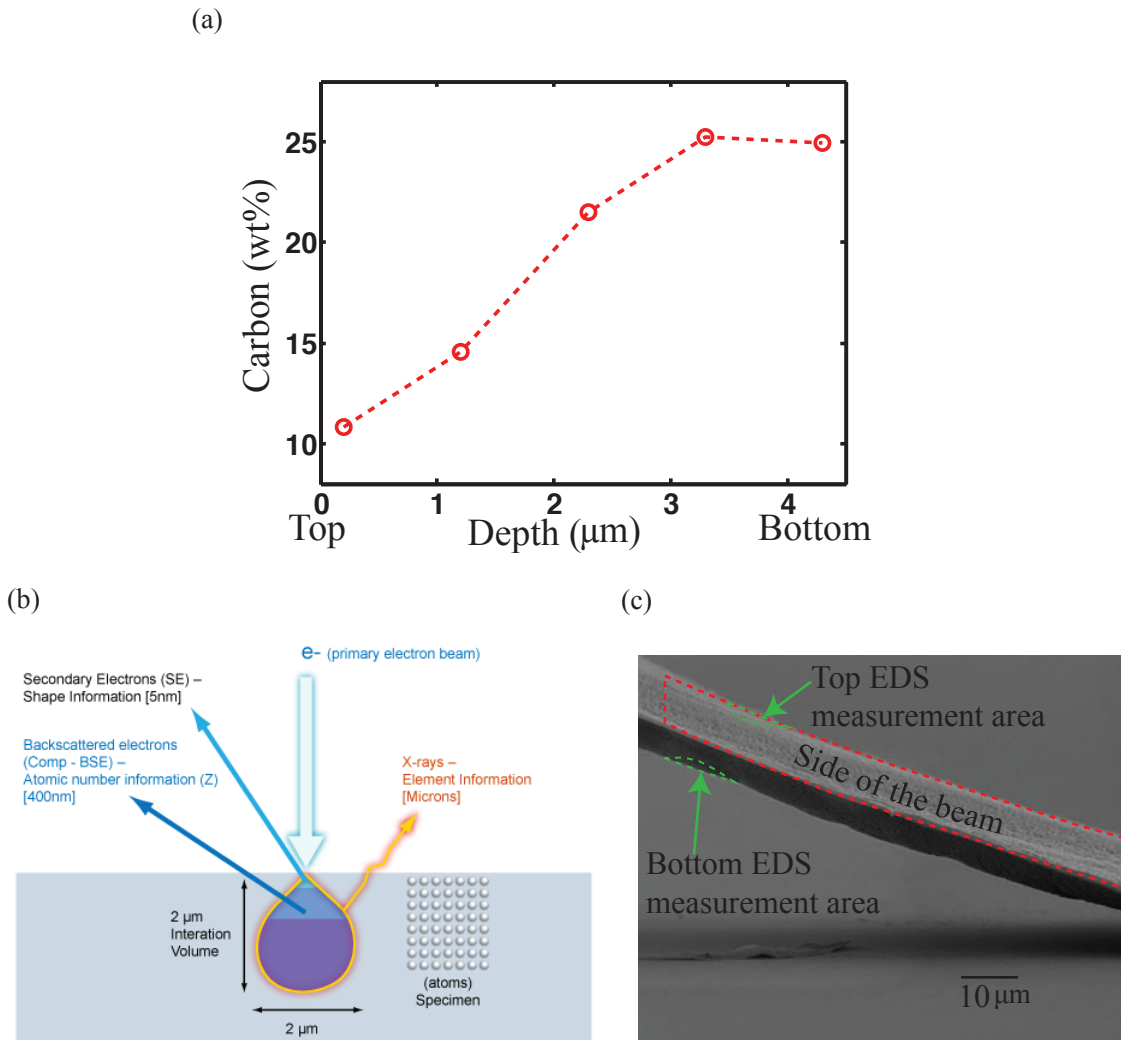
Figure 3-4. (a) Cross-sectional Auger Electron Spectroscopy (AES) of the inkjet-printed sintered silver nanoparticles film showing larger amount of residual carbon near the bottom of the film than the top of the film. (b) Typical Interaction volume of the electron beam. (c) 8-pass printed curled cantilever is tilted to measure the residual carbon amount only at the top and the bottom region of the film using Energy Dispersive X-ray Spectroscopy (EDS).
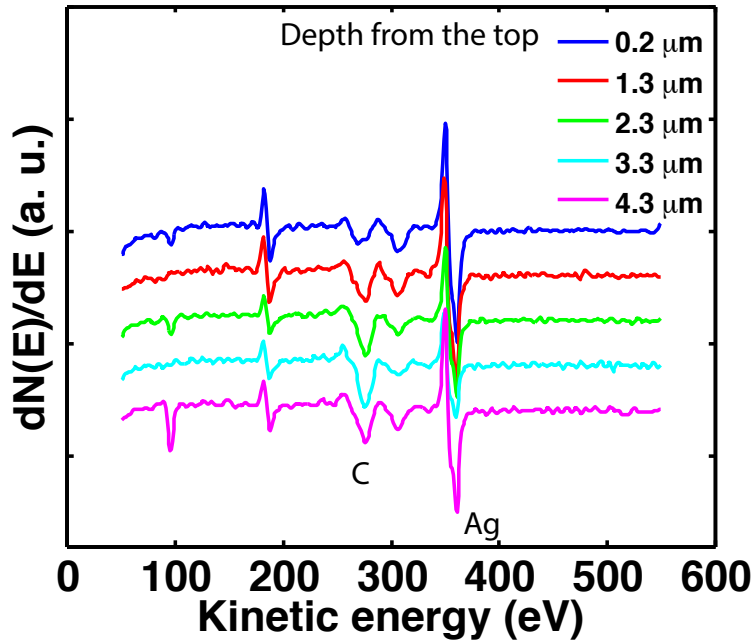
Figure 3-5. Auger Electron spectroscopy (AES) spectrums of the silver nanoparticles film, which was measured at different depth of the cross-sectional sample from the top of the film.

Cross-sectional Auger electron spectroscopy (AES) was utilized to perform elemental analysis across the thickness of the beam. A cross-section of the beam was made by cleaving the unreleased sintered cantilever sample and AES was performed at different depths of the beam. The cross-sectional AES revealed that the film formed from sintered silver nanoparticles consists of silver and residual carbon from the stabilizer with a larger concentration of carbon near the bottom of the film than the top of the film, as shown in Figure 3-4(a). The Energy Dispersive X-ray Spectroscopy (EDS) measurement was performed to check the reliability of the AES data. AES is an analytical technique to determine the elemental composition of the surface layer of a sample, which utilizes the emission of the Auger electron. On the other hand, EDS measurements have a large electron beam interaction volume (ca. 2-4 μm^3) with the specimen. Hence, EDS is not generally a suitable technique for cross-sectional elemental analysis of the beam made with limited number of printing passes. Figure 3-4(b) shows the typical interaction volume of electron beam with the sample. To measure the elemental composition only near the top and the bottom of the cantilever, a thicker cantilever with 8 printing passes was printed. Figure 3-4(c) shows this thicker cantilever after release, which is tilted such that the EDS measurement can be performed on the region only near the top and the bottom of the cantilever. The amount of carbon near the top (ca. 12 wt%) and near the bottom (ca. 26 wt%) of the cantilever measured by EDS technique shows

similar results with the data obtained using AES. The spectrums from the AES and EDS measurements are presented in Figure 3-5 and Figure 3-6.

(a)

(b)
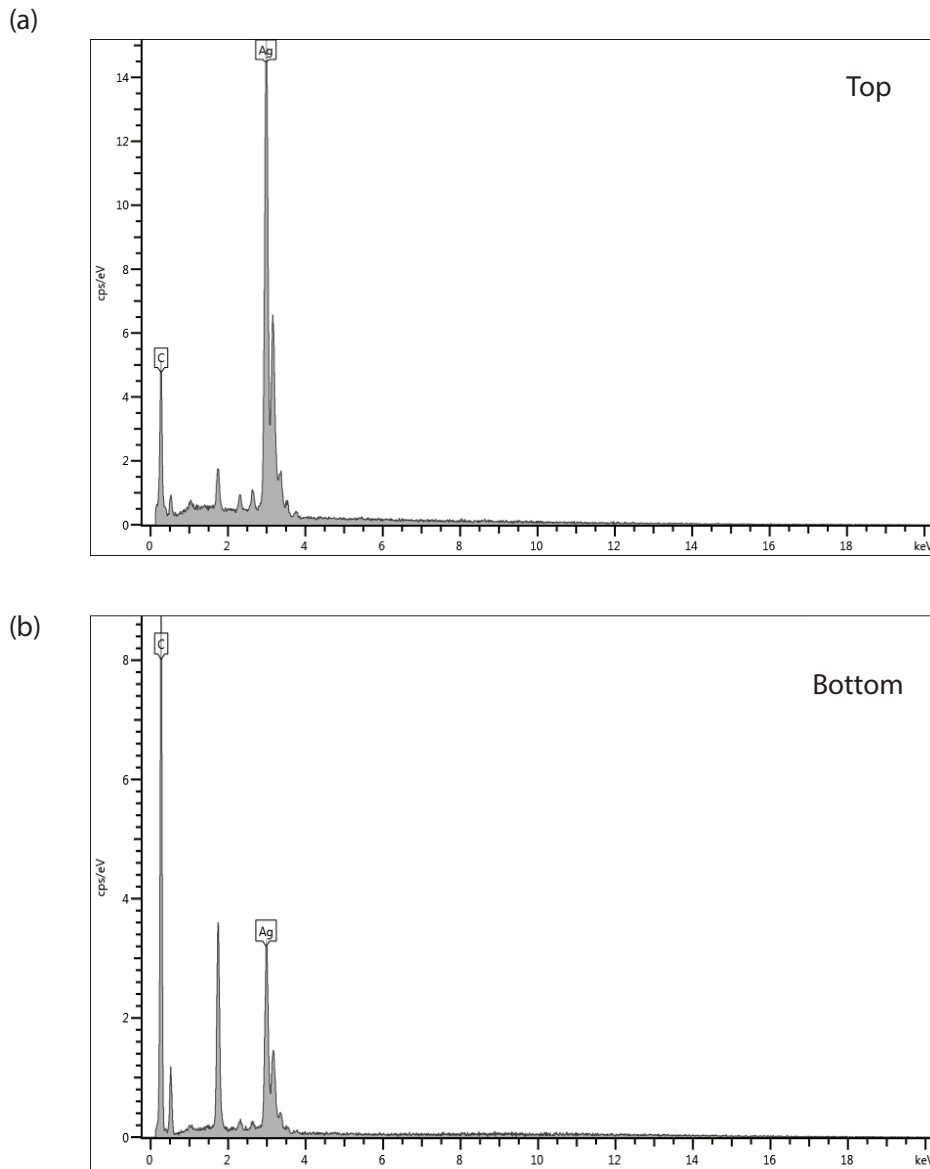
Figure 3-6. Energy Dispersive X-ray Spectroscopy (EDS) spectrums at the (a) top and (b) the bottom of the silver nanoparticles film. The suspended cantilever form from silver nanoparticles was tilted such that the electron beam interaction volume resides only at the top or the bottom of the beam.

3.6 Variation in Coarsening and Densification across the Thickness of the Sintered Film

The matter transport paths during the sintering of two nanoparticles includes surface diffusion, lattice diffusion, and grain boundary diffusion, as illustrated in Figure 3-7. All these matter transport mechanism can be classified as two competing group of densifying and non-densifying mechanisms depending on their capability of causing shrinkage [158]. Figure 3-7(b) illustrates the shrinkage behavior of the densifying matter transport as opposed to its non-densifying counterpart using a two particle model. Both densifying and non-densifying mechanisms lead to a more thermodynamically stable state by reducing the surface area to volume ratio. The non-densifying mechanisms of surface atomic diffusion and lattice diffusion initiate neck formation and also cause subsequent neck growth. The densifying mechanisms of grain boundary diffusion and through-lattice diffusion cause volume shrinkage which leads to the development of tensile stress in the film.
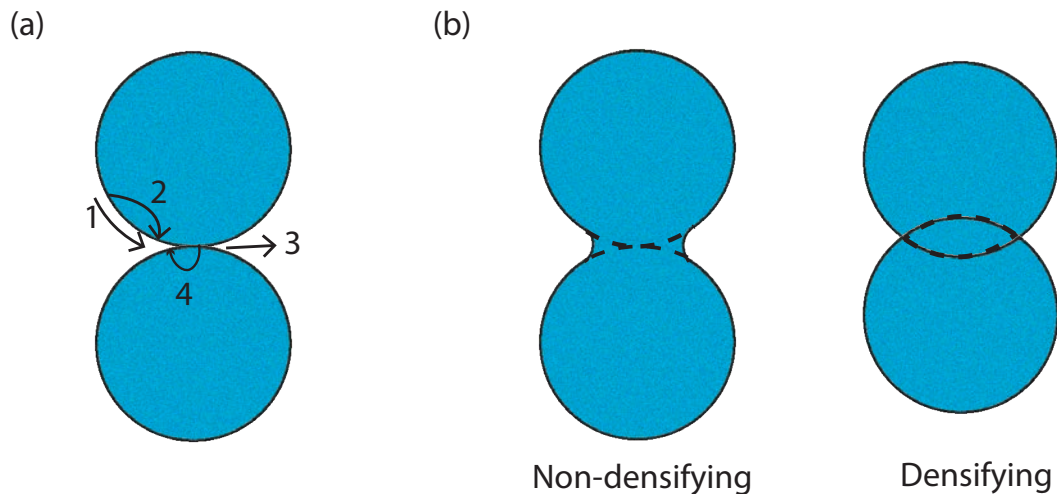
Figure 3-7. (a) Diffusion mechanisms in nanoparticles sintering process: 1) Surface diffusion, 2) lattice diffusion, 3) grain boundary diffusion, 4) through-Lattice diffusion. (b) Non-densifying and densifying diffusion mechanism: Non-densifying mechanism includes surface and lattice diffusion, and densifying mechanism includes grain boundary and through-lattice diffusion.

During the sintering of a constrained film, the slower through-lattice diffusion dominates over faster grain boundary diffusion [155]. The higher concentration of residual stabilizers near the bottom of the inkjet-printed silver nanoparticles film promotes more particle coarsening through

non-densifying diffusion mechanisms than the top of the film as shown in the cross-sectional scanning electron microscope (SEM) image presented in Figure 3-8.

(a)

(b)
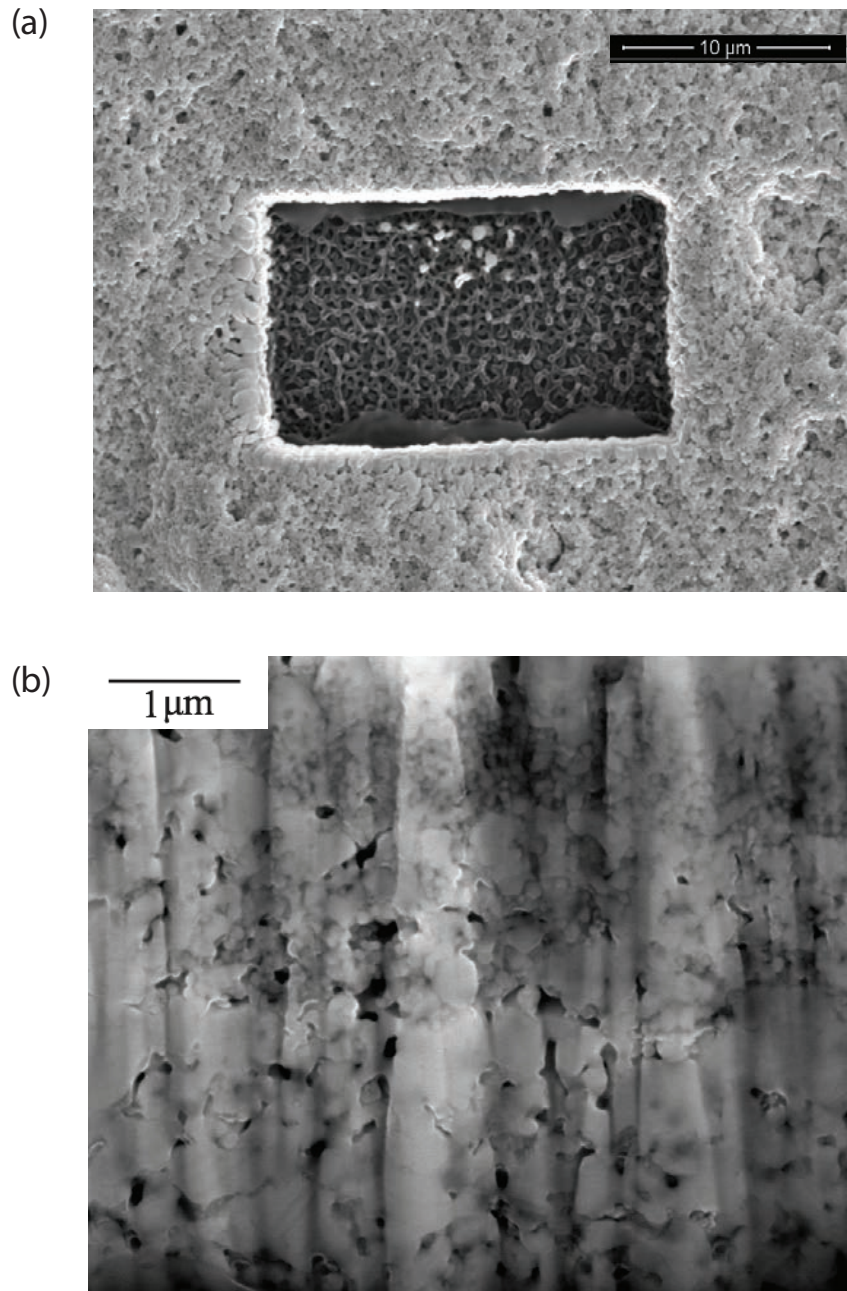
Figure 3-8. (a) Milling of silver film using Focused Ion Beam (FIB). (b) Bottom of the film shows more coarsening than the top of the film.

A focused ion beam (FIB) was used to make the cross section in the silver nanoparticle film. The SEM image also illustrates a higher porosity at the bottom of the film than the top of the film. Figure 3-9 shows a lower Young's modulus at the bottom of the film than the top of the film. To measure the Young's modulus using the nanoindentation technique, the suspended cantilevers were harvested and steadily attached to a silicon substrate by placing adhesive tapes on the shorter sides of the cantilever. The Young's modulus at the bottom of the film was measured by flipping the cantilevers over so that the bottom of the beams faces upwards before attaching them on the silicon substrate.
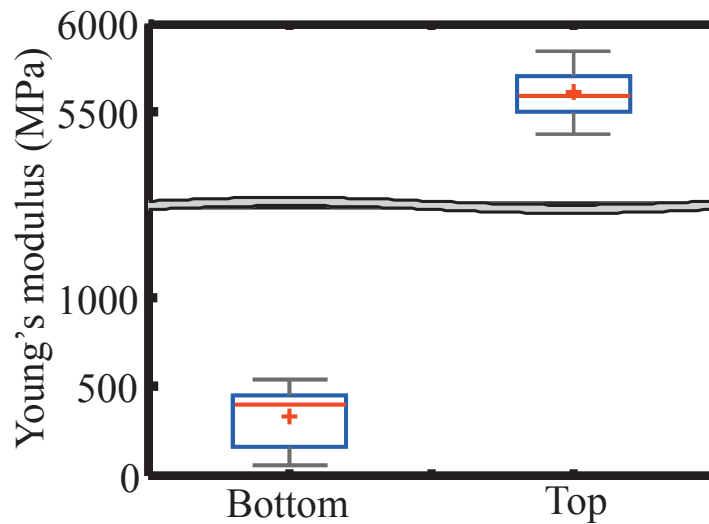
Figure 3-9. Nanoindentation measurement shows less densification near the bottom of the film than the top of the film.

The lower Young's modulus along with the higher porosity suggests the non-densifying nature of the particles coalescence at the bottom of the film. Due to the competing nature of the two groups of diffusion mechanisms, a higher rate of non-densifying diffusion mechanism retards the densifying diffusion mechanism more near the bottom of the film. The lower rate of densifying diffusion mechanisms causes less volume shrinkage and hence induces less tensile stress at the bottom of the film than the top of the film. This low to high tensile stress from the bottom to the top of the film triggers the upward bending of the cantilevers after release. This understanding of the evolution of stress gradients in printed nanoparticles film denotes significant contributions towards the enhancement of the reliability of flexible and printed electronics. This has special interest in the progress of printed MEMS through nanoparticle based ink development and their sintering study to reduce the residual stabilizers and their gradient in the deposited film.

While the proper understanding of the generation of stress gradients in printed thin films offers a route to control the curling of the suspended structures, this understanding also allows the design of novel MEMS architectures exploiting this behavior. The next chapter will present a novel three terminal MEMS relay architecture providing excellent immunity to the stress generation in printed thin film. An all inkjet-printed relay process flow will be developed. The electrical characteristics and an analytical model of these relays will also be presented.

Chapter 4: Fully Inkjet-Printed Stress-Tolerant Three Terminal Reed Relay

Microelectromechanical (MEM) relays with movable cantilevers operated by electrostatic actuation can provide a solution for ultra-low leakage devices with hyper-abrupt switching [87], [89]. MEM relays fabricated using printing techniques can provide switching devices for low-cost and large-area electronics with low leakage, excellent subthreshold swing, and very low on-resistance. Inkjet-printing is attractive for the fabrication of MEM relays due to its mask-free, vacuum-independent, low-temperature and environment-friendly processability [19].
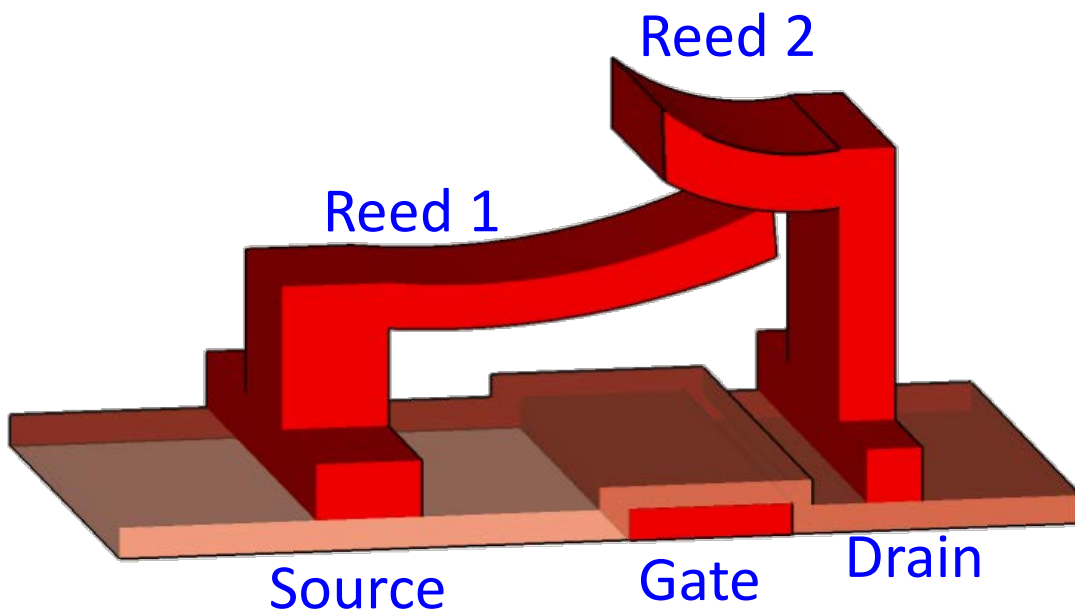
Figure 4-1. Stress-tolerant microelectromechanical reed relay architecture

Although the previously reported printed MEM relays showed superior performance in terms of very low on state resistance (R_{ON}) and minimal off current (I_{OFF}), [19], [21] unfortunately, these structures are vulnerable to stress variations in the printed cantilevers which can cause the suspended beams to curl up. In addition to causing increased device-to-device variation, this phenomenon can increase the electrostatic actuation gap, making the MEM relays inoperable in reasonable actuation voltage ranges. Additionally, in the previously reported printed MEM relays, only the cantilever and post structure was inkjet-printed while the sacrificial layer was deposited

using spin-coating [19], [21], which leads to a poor area scalability. Therefore, a new approach in MEM relay structural design and sacrificial layer processing is necessary to make it viable for realistic large-area electronics realization. In this chapter, the first MEM relay with a printed sacrificial layer will be presented, which makes it realizable for large-area systems; the relay implements a novel structure that provides immunity to the stress variations in the printed cantilevers. A second cantilever is introduced with higher stiffness over the switching cantilever to block the upward curling of the movable cantilever. This MEM relay resembles a reed switch structure with the two reeds in a normally closed state and hence named as 'Reed Relay'. Figure 4-1 illustrates the stress-tolerant reed architecture of MEM relay.

4.1 Processes Development

4.1.1 Inkjet-Printing of Silver Nanoparticles Ink on PMMA Surface

Silver nanoparticles are stabilized in solvents by encapsulating with either polymer (poly acrylic acid, polyvinylpyrolidone etc.) or low molar mass molecules (long chained thiols and carboxylates etc.). Various solvent systems are used to make the ink based on the material used for encapsulating the nanoparticles. CCI-300 from Cabot corp., EMD 5603 and EMD 5730 from Sun chemicals use alcohol based solvents. CCI-300's solvent system mostly contains ethanol and ethylene glycol. EMD 5603 solvent system contains ethanol, ethylene glycol, glycerin and 2-isopropoxyethanol. EMD 5730 contains ethylene glycol and ethyl (S)-2-hydroxypropionate. CCI-300 and EMD5603 have similar surface tension and show similar wetting on PMMA surface. De-wetting of ink was observed when CCI-300 or EMD 5603 was printed on the untreated PMMA surface. PMMA surface energy can be increased by UV-Ozone (UVO) treatment. Both CCI-300 and EMD 5603 ink show very good patterns on the PMMA surface (see Figure 4-2(a)) after 1 min of UVO treatment. EMD 5730 ink also de-wets on the PMMA surface. It requires a long UVO treatment for appreciable wetting of EMD 5730 ink on the PMMA surface. Moreover, even with UVO treatment, EMD 5730 ink does not show good pinning on the PMMA surface. However, EMD5730 ink produces a very good pattern after a short O_2 plasma treatment on the PMMA surface (see Figure 4-2(b)). A 40 W plasma power was used in the treatment process. O_2 plasma treatment not only increase the surface energy of the PMMA surface but also create nanometer-scale roughness on the surface, which helps to create better pinning of the ink.

DGP 40LT-15C ink from ANP uses TGME(Triethylene glycol monoethyl ether) as the solvent. DGP 40LT-15C shows huge spreading on the untreated PMMA surface (see Figure 4-2(c)). Hence, this ink is not suitable to print on the PMMA surface unless the PMMA surface energy is reduced with a surface treatment. A self assembled monolayer (SAM) of HMDS, OTS etc. are usually deposited as surface treatment to make any surface hydrophobic and to reduce the surface energy. However, HMDS and OTS show poor adhesion on the PMMA surface and can not change the PMMA surface properties.

(a)

PMMA

No PMMA surface treatment

200 μm

1 min UVO treatement on PMMA surface

(b)

200 μm

PMMA

PMMA

No PMMA surface treatment

40 W O$_2$ plasma treatement for 20 s on PMMA surface

(c)

PMMA

200 μm
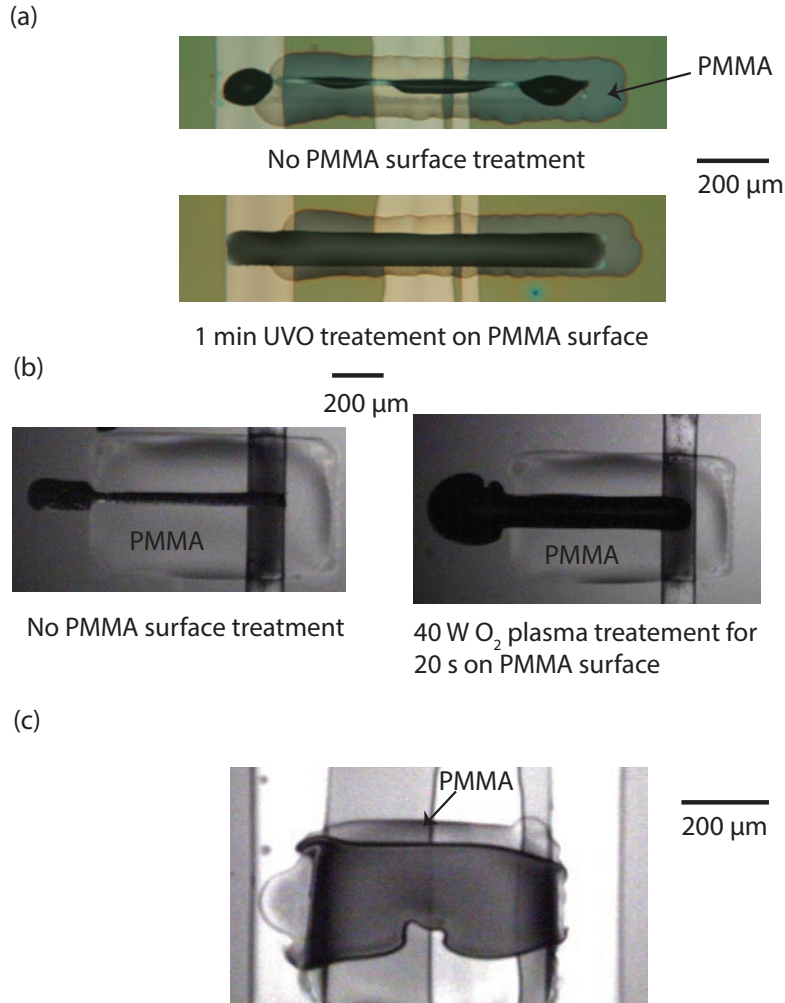
Figure 4-2. Printing silver nanoparticles ink on PMMA surface. (a) CCI-300 and EMD 5603 ink produce good pattern on the 1 min UVO treated PMMA surface. (b) EMD 5730 ink produces good pattern on the PMMA surface after 40 W O2 plasma treatment for 20 s. (c) DGP 40LT-15C ink from ANP shows massive spreading on the untreated PMMA surface.

4.1.2 Sintering Condition of the Silver Ink

The silver ink printed on the PMMA sacrificial layer can penetrate through PMMA during the sintering step. The amount of penetration of the silver ink through PMMA layer was characterized using a crossbar metal-insulator-metal (MIM) capacitors where printed silver electrodes were used as the top and the bottom electrodes and printed PMMA layer was used as the insulating layer (see Figure 4-3(a)). The penetration of the top silver electrode into the PMMA layer demonstrated itself through the dips nears the electrode edges (see Figure 4-3(b)).

59
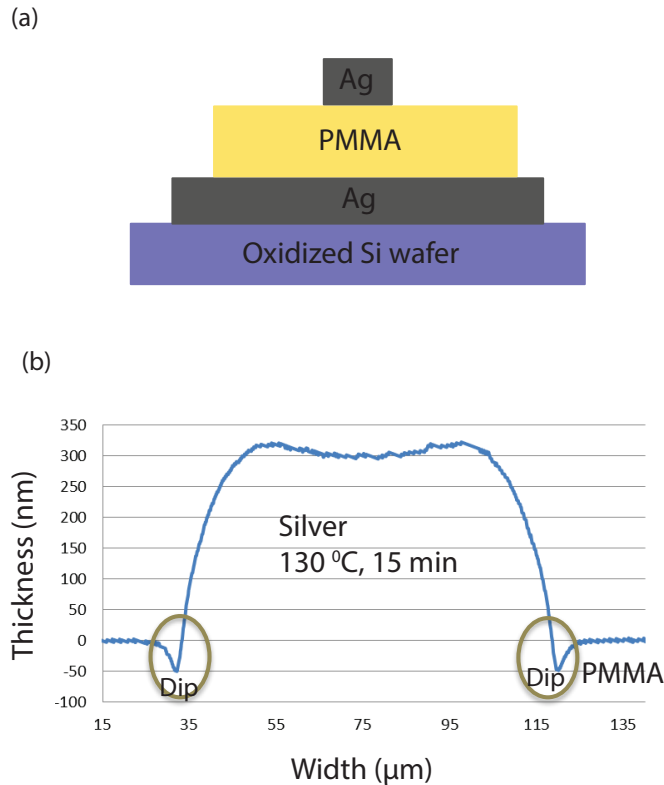
Figure 4-3. (a) Crossbar MIM structure to measure top silver beam penetration with various sintering condition. Thickness of the PMMA layer was calculated from the capacitance measurement taking the dielectric constant of PMMA as 4.1 at 1 kHz. (b) Dips of ~ 50 nm is observed near the edges of the top electrode sintered at 130 ^{0}C for 15 min.

This penetration of the silver electrode into the PMMA layer should be minimized for a reliable MEMS process. The bottom electrode of the MIM structure was inkjet-printed on an oxidized silicon wafer and sintered at 180 ^{0}C for 15 min. The PMMA layer is then inkjet-printed on the bottom electrode and annealed at 150 ^{0}C for 10 min. After that, the top silver electrode was inkjet-printed on the PMMA layer and sintered at various temperature for 15 min. The initial PMMA thickness in the MIM structure was ~1.84 μm. The thickness of the PMMA layer after the sintering of the top electrode was calculated from the capacitance measurement. The dielectric constant of the PMMA layer was taken as 4.1 at 1 kHz. The top electrode sintered at 130 ^{0}C shows a thickness change of ~60 nm. At 150 ^{0}C, the PMMA thickness reduction was ~340 nm. At more than 175 ^{0}C, the top silver electrode completely penetrates through the PMMA layer and makes contact with the bottom electrode. Considering this, the sintering condition for the silver structural layer should

60

be limited to 140 ^{0}C. Table 4-1 presents the thickness of the PMMA layer with various sintering condition of the top electrode.

Sintering Temperature for top Ag (^{0}C)	Capacitance (pF)	Thickness (µm)
130	0.73	1.79
150	0.87	1.51
175	Bottom and top electrodes are shorted	
200		

Table 4-1. Thickness of the PMMA layer with various sintering condition of the top electrode.

4.1.3 Full Process Flow

Figure 4-4 illustrates the schematic process flow used for the fabrication of the fully inkjet-printed 3-terminal MEM reed relay. Inkjet-printing process was performed using a Fujifilm Dimatix materials printer (DMP-2831) with a Fujifilm Dimatix cartridge delivering a 10 pL droplet volume. The gate electrodes were inkjet-printed using a nanoparticle-based silver ink (EMD 5730 from Sunchemical Corp.) on an oxidized silicon wafer, followed by a sintering process at 180 ^{0}C on a hot plate for 30 min. The film thickness and sheet resistance of the gate electrodes were 550 nm and 0.50 Ω/sq respectively. A gate dielectric solution was prepared by dissolving Poly-4(vinylphenol) (PVP) (10 wt%) powder in propylene glycol methyl ether acetate (PGMEA) solvent, with poly(melamine-co-formaldehyde) (2 wt %) as a cross-linking agent (CLA).

The dielectric was spin-coated onto the printed gate electrodes and cross-linked for 30 min on a 180 ^{0}C hot plate, which results in a film thickness of 530 nm. Note that due to the fact that the reed relays operate in non-pull-in mode, gate isolation using a dielectric layer is not a critical part of the process flow and can readily be transferred to a printing process. Figure 4-5 presents an optical image and the thickness profile of an inkjet printed PVP dielectric layer on the gate electrode; the drain and source electrodes were printed on top of the PVP layer.

The PVP ink was prepared by dissolving Poly-4(vinylphenol) (PVP) (12 wt%) powder in 1-Hexanol solvent, with poly(melamine-co-formaldehyde) (PMF) (PVP: PMF=10:1) as a cross-linking agent. Nonetheless, this cross-linked insulation layer can prevent undesired gate leakage if the movable reed pulls-in with an excessive electrostatic force.
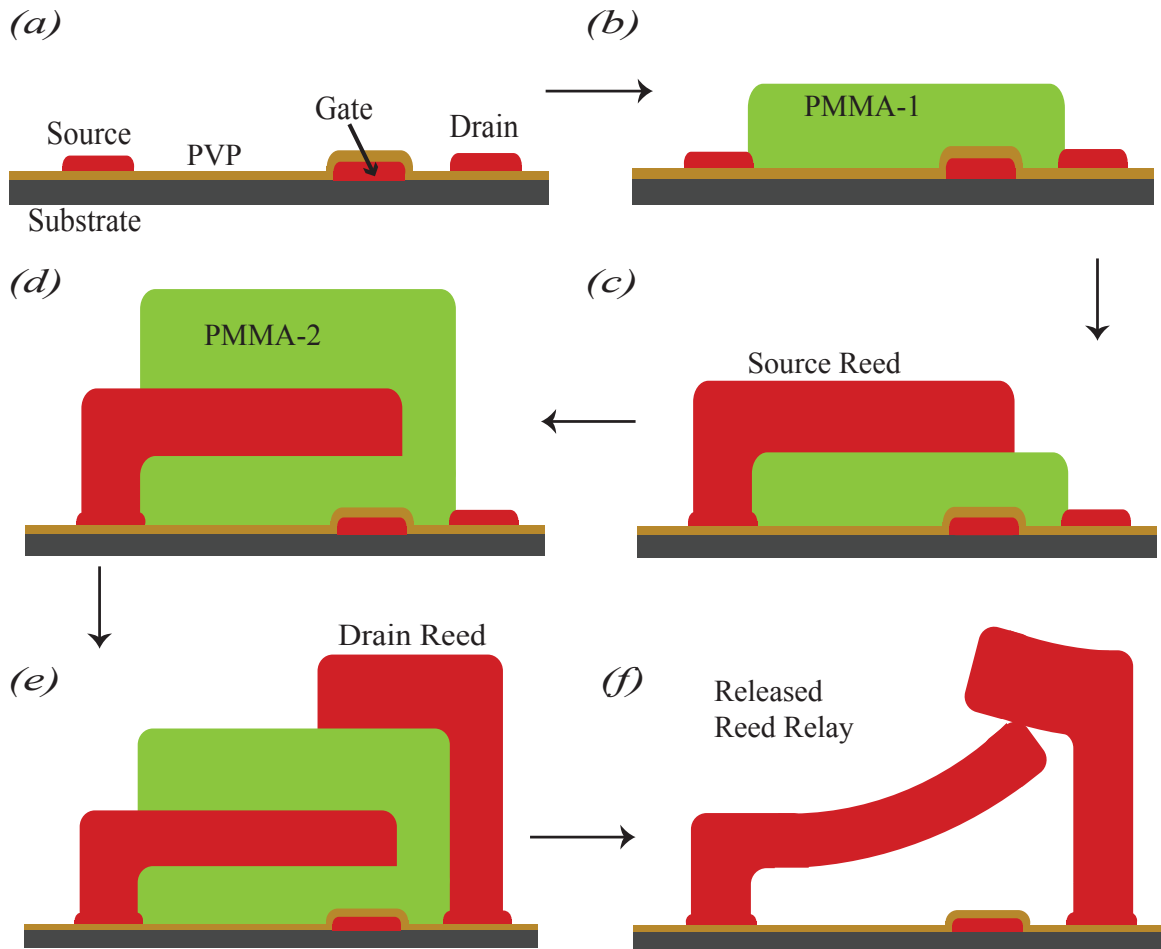
Figure 4-4. Process flow for ink-jet printed MEM reed relay fabrication. (a) Fabrication of the contacting electrodes: gate electrode is inkjet-printed on silicon/silicon dioxide substrate followed by spin-coated PVP dielectric deposition; source and drain electrode are inkjet printed on PVP layer. (b) First sacrificial PMMA layer is inkjet-printed, (c) source reed is inkjet-printed on PMMA-1 sacrificial layer and anchored at the source electrode, (d) second sacrificial PMMA layer is inkjet-printed covering the source reed, (e) drain reed is inkjet-printed on PMMA-2 sacrificial layer and anchored at the drain electrode, (f) sacrificial layer removal by dipping in hot acetone, washing with IPA and drying in a critical point drying chamber.

The electrodes for the source and drain reeds were also inkjet-printed using the same silver nanoparticle ink that was used to print the gate electrode and were then sintered on a 180 ºC hot plate for 30 min. A carefully designed Polymethyl methacrylate (PMMA) ink was used for stable jetting performance and coffee-ring free printing of the sacrificial layer. The coffee-ring effect

creates highly non-uniform thickness profiles with a ridge near the edge and a much thinner valley. A sacrificial pad suffering from coffee-ring effect is thus detrimental to MEM structure realization due to variations in the suspended height upon release.

(a)
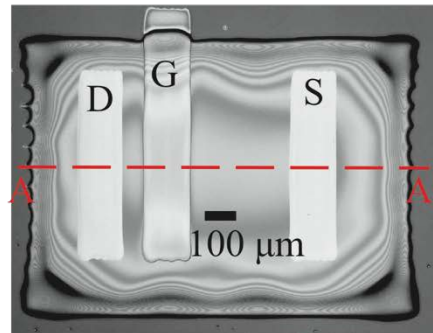
(b)
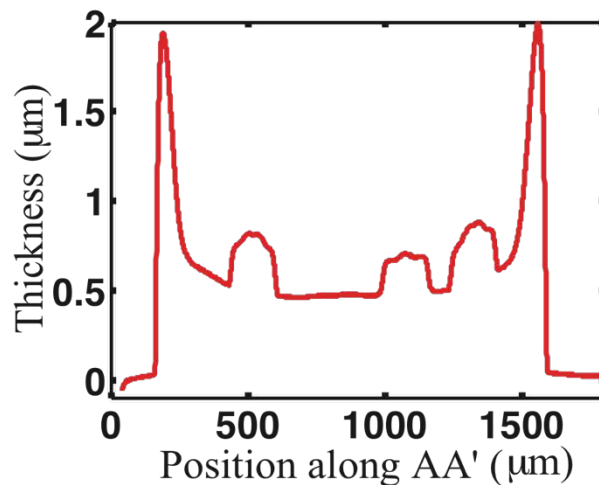
Figure 4-5. (a) Poly(4-vinylphenol) (PVP) ink was inkjet printed on the gate (G) electrode and cross-linked at 230^{0}C by placing the sample on a hot plate. The source (S) and drain (D) electrodes were inkjet-printed on the printed PVP layer. (b) Inkjet-printed PVP layer shows a coffee ring with peak-to-valley thickness ratio of ~4:1. Printed PVP layer presents a uniformly thick valley of ~500 nm, which is well prepared to accommodate the reed relay.

The source reed was also printed using the EMD5730 Ag nanoparticle ink where both the source beam on the PMMA-1 layer and the anchor on the source electrode was printed in the same printing pass. Prior to the Ag ink printing, the PMMA-1 surface was treated with 40 W O_2 plasma for 15 sec to improve the ink wettability. The printing process was carried out on a 60 ^{0}C substrate to get

better anchor to beam step coverage. A multi-pass printing process with interspersed drying on a 115 ^{0}C hot plate was employed to obtain the designed thicknesses of the source beam; each printing pass effectively added ~1 μm thickness to the beam (see Figure 4-6). The source reed was dried on a 115 ^{0}C hot plate for 20 min and then sintered at 140 ^{0}C with a ramp rate of 5 ^{0}C/min, which results in a resistivity of ~ 5x10^{-7} Ω-m.
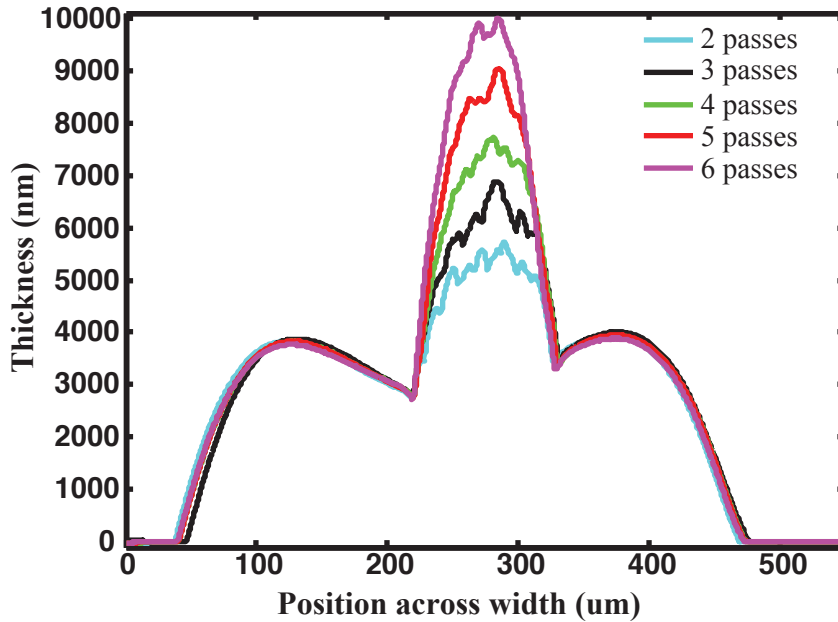
Figure 4-6. Thickness Profiles of Silver beam printed on PMMA surface for various printing passes. Note that the beam penetrated a little bit through PMMA surface as the sintering temperature goes above the PMMA glass transition temperature.

The second PMMA sacrificial layer (PMMA-2) was inkjet-printed in 5 passes, using the same PMMA ink that was used for PMMA-1 layer, to realize a uniform surface on the underlying high topology substrate comprising PMMA-1 and the source reed (see Figure 4-7). PMMA-2 layer was thermally cross-linked at 140 ^{0}C for 10 min on a hot plate. The drain reed was inkjet-printed using 8 passes printing of EMD5730 Ag nanoparticle ink on the PMMA-2 layer, treated with 40 W O$_2$ plasma for 15 sec, with interspersed drying on a 115 ^{0}C hot plate. The drain reed was dried on a 115 ^{0}C hot plate for 20 min and then sintered at 140 ^{0}C with a ramp rate of 5 ^{0}C/min. Finally; the PMMA-1 and PMMA-2 sacrificial layers were removed by dipping into a 45 ^{0}C acetone bath. The acetone was replaced with isopropyl alcohol (IPA) by dipping into a series of IPA baths, and then

the devices were dried in a critical point drying chamber to prevent stiction. All of the fabrication processes were performed in air at a maximum temperature of 180 ^{0}C.
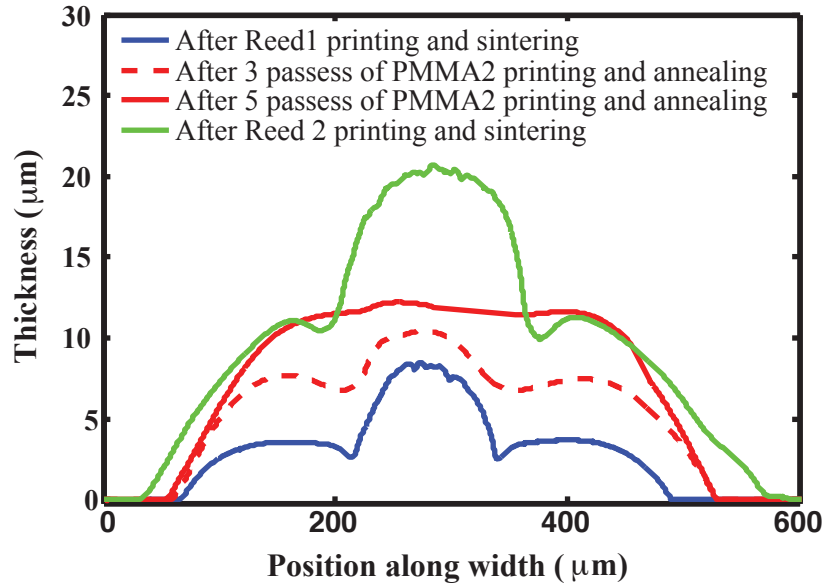
Figure 4-7. Printing the second PMMA sacrificial layer is challenging due to high topography of the surface to print on. A 5-pass printing of second PMMA layer exhibits a nearly uniform surface while 3-pass printing shows large thickness variation.

4.2 Device Operation

Figure 4-8 shows an optical image of a reed relay before removing the sacrificial PMMA layer. The source and drain reeds are released by dissolving PMMA in hot acetone and dried in a critical point drying chamber to avoid stiction. After release, the source reed shows very high curling without the presence of the blocking drain reed.

A suspended source reed with very limited curling can be realized through the curling restriction imposed by the drain reed, as shown in Figure 4-9. The source and the drain reeds are normally in contact and hence the as-fabricated devices are in the 'on' state. Above a certain gate bias (V_{TOF}), the electrostatic force actuates the source reed downwards while leaving the stiffer drain reed in its original position. This separation of source and drain reeds turns the devices 'off'. Note that the reed relay can be operated in non pull-in mode since only a marginal separation between source and the drain reed is necessary to turn off the devices.
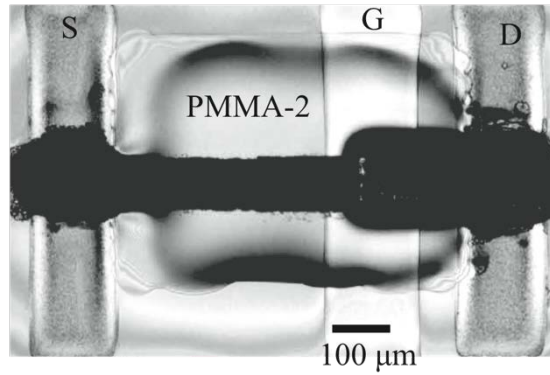
Figure 4-8. Optical image of the unreleased reed relay showing electrodes, sacrificial PMMA layers and the source and drain reeds.
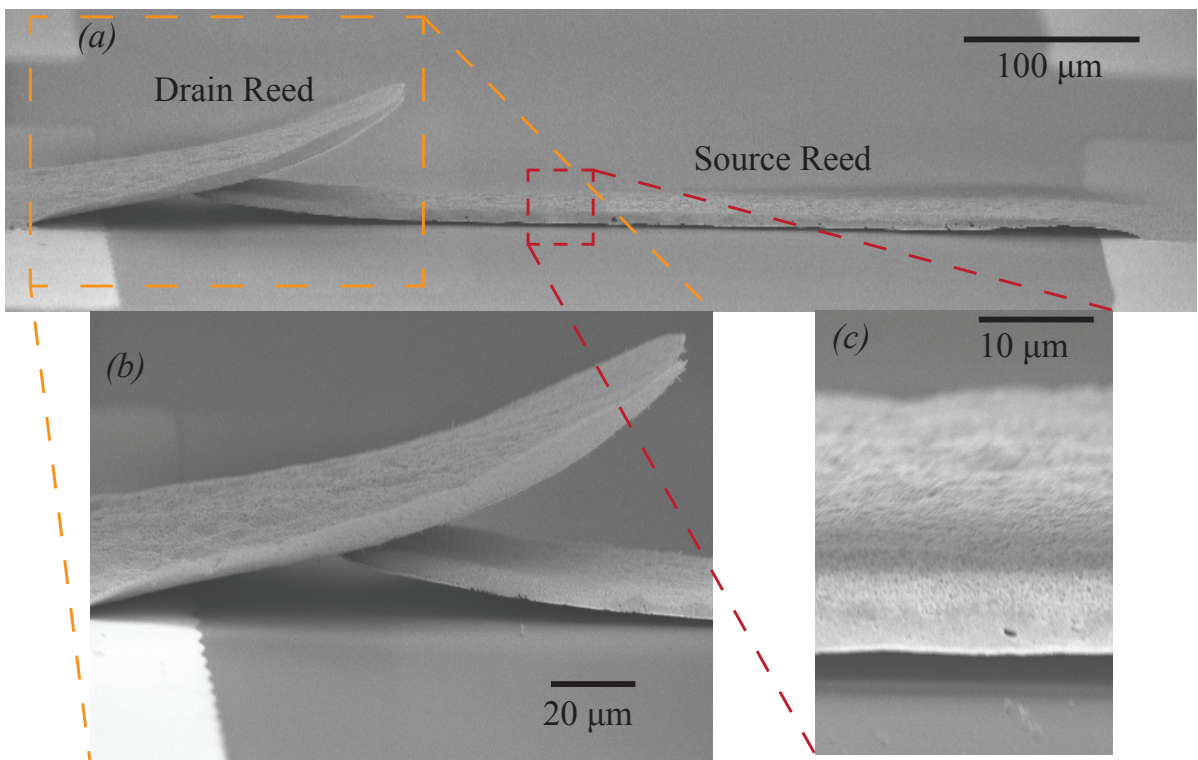
Figure 4-9. SEM images of inkjet-printed MEM reed relay. (a) Drain reed blocks the curling of source reed, (b) close up image of the drain and the source reed contact region, (c) close up image of the suspended source reed showing the air gap.

4.3 Device Characterization

4.3.1 Switching Characteristics

(a)

(b)
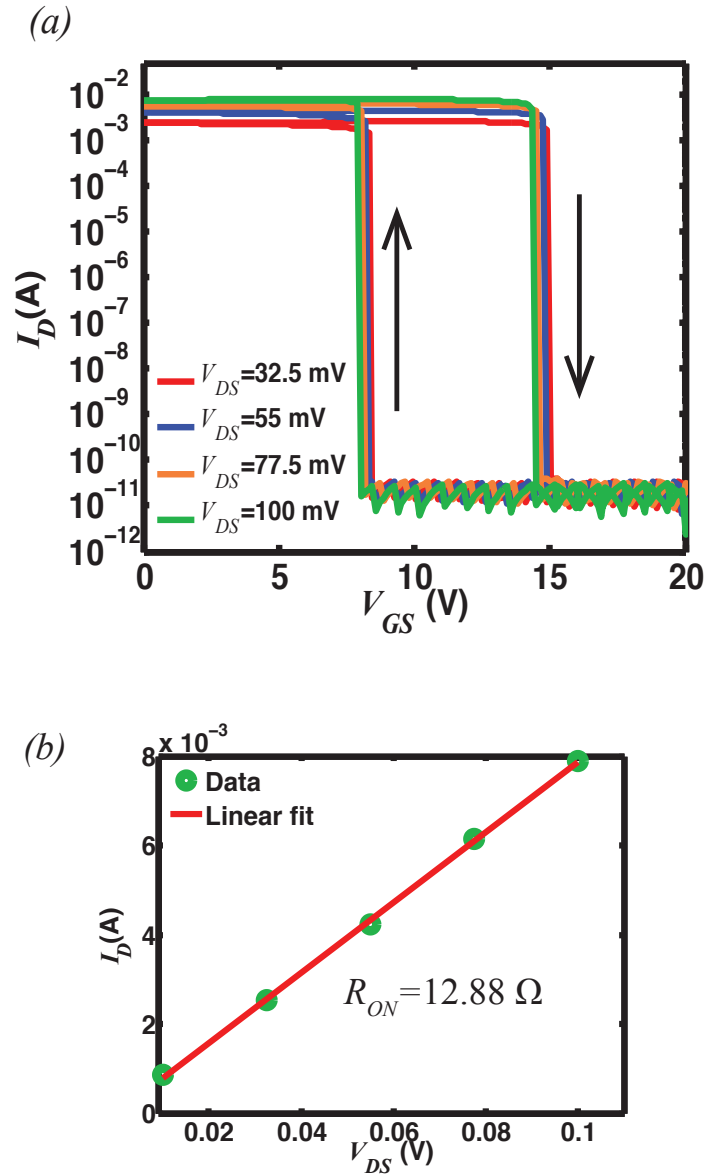
Figure 4-10. (a) Switching characteristics of inkjet-printed reed relays. I_D-V_{GS} characteristics of the reed relay with varying drain bias (V_{DS}) for a 5.5 μm thick source reed showing abrupt switching with turn-off voltages (V_{TOF}) of ~15 V. These devices also show high on current and very low off current that is in the noise floor of the parameter analyzer. (b) Very low on resistances (R_{ON}) of 12.88 Ω is extracted from the I_D-V_{DS} characteristics.

Figure 4-10(a) shows the measured electrical switching characteristics of a representative reed relay with ~5.5 μm thick source beam. The measured I_D-V_{GS} characteristics show excellent characteristics with hyper-abrupt switching, high on-state current (I_{ON}), extremely low off-state current (I_{OFF}), and a turn-off voltage (V_{TOF}) of ~15 V.
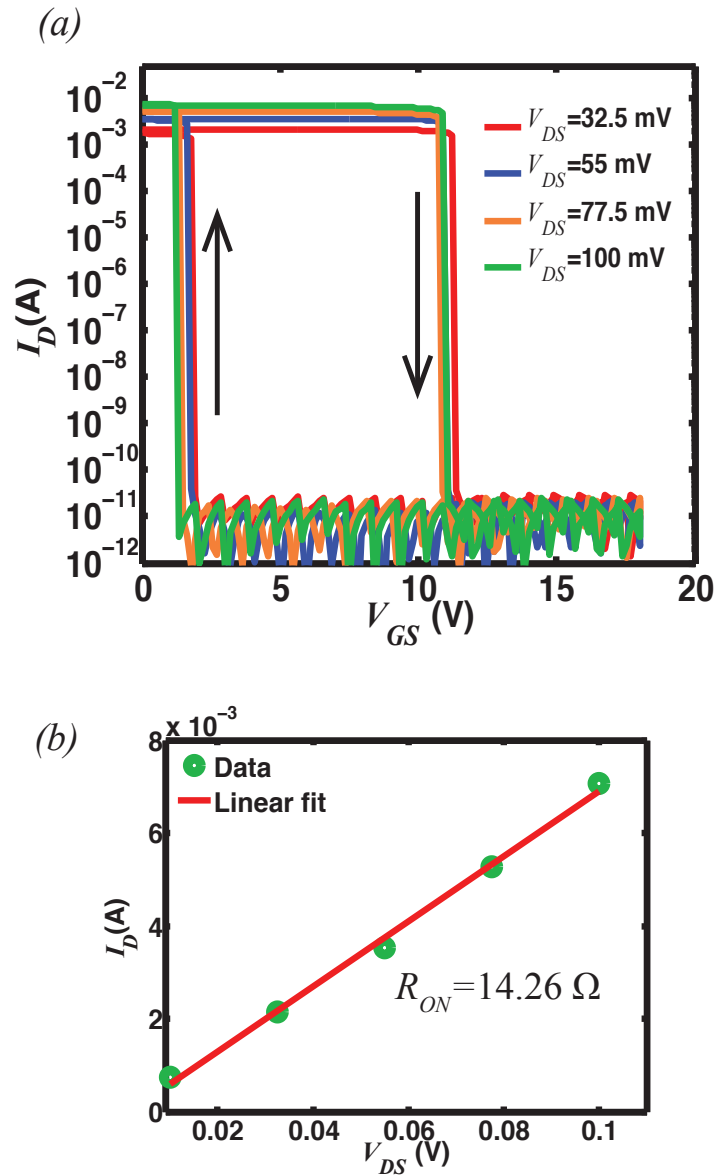
Figure 4-11. (a) I_D-V_{GS} characteristics of the reed relay with varying drain bias (V_{DS}) for a 4.5 μm thick source reed showing a turn-off voltages (V_{TOF}) of ~11 V. (b) low on resistances (R_{ON}) of 14.26 Ω is extracted from the I_D-V_{DS} characteristics.
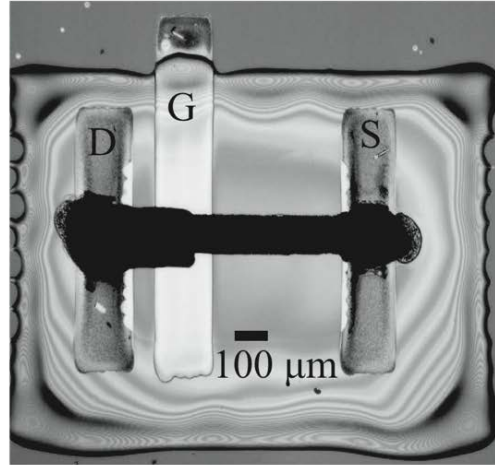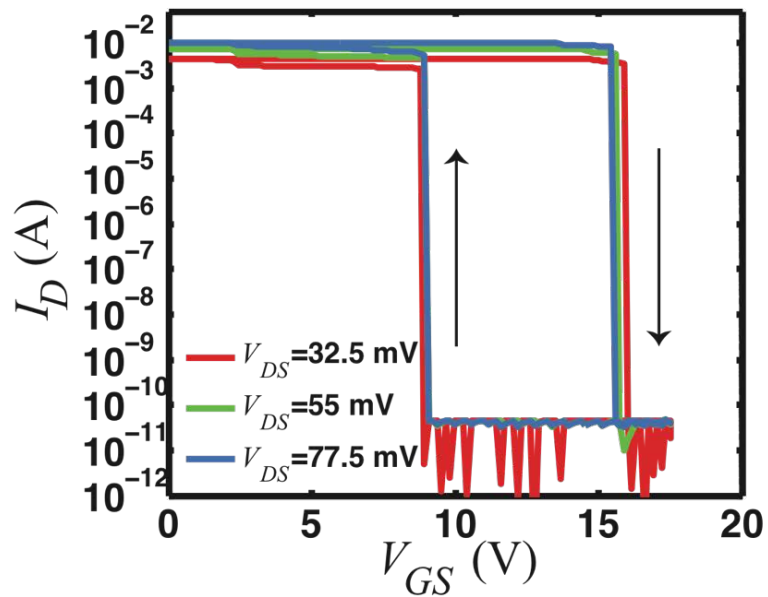
Figure 4-12. (a) Fully Inkjet-printed reed relay with printed PVP dielectric layer and (b) its switching characteristics which shows similar performance of the reed relays with spin-coated PVP layer.

The reed relays show a hysteresis of ~8 V; such hysteresis is commonly observed in MEMS switching devices due to the adhesion force between the source and drain reeds and the asymmetric actuation gap during forward and reverse gate voltage sweeps. Figure 4-11(a) shows the

characteristics of a representative reed relay with a ~4.5 μm beam, delivering a V_{TOF} of ~12 V. The reed relays exhibit extremely low on-state resistance (R_{ON}) of 12.88 Ω and 14.26 Ω, as shown in Figure 4-10(b) and Figure 4-11(b). The design parameters for the devices shown in Figure 4-10 and Figure 4-11 are summarized in Table 4-2. Figure 4-12 shows an optical image of the reed relay employing a printed PVP dielectric layer and its switching characteristics, which is similar to the devices with spin coated PVP dielectric layer.

Parameter	Value
PMMA-1 thickness	2.2 μm
PMMA-2 thickness	3.2 μm
PVP thickness	500 nm
Source reed: Length x Width x Thickness	550 μm x 95 μm x [5.5, 4.5] μm
Drain reed: Length x Width x Thickness	150 μm x 110 μm x 9 μm
Gate actuation area	180 μm x 95 μm

Table 4-2. Designed parameters of the printed reed relays of Figure 4-10 and Figure 4-11

4.3.2 Dynamic Performance

To study the dynamic behavior, a printed reed relay was loaded with a 100 kΩ resistor in a buffer configuration, as shown in Figure 4-13(a). Figure 4-13(b) shows the output voltage (V_{OUT}) of the buffer, recorded in time domain using a digital storage oscilloscope in response to a square-wave input signal (V_{IN}) with a frequency and amplitude of 200 Hz and 15 V respectively. The printed reed relay is in the on-state at V_{IN} of 0 volt, which results in a negligible amount of voltage drop across the relay due to its extremely low on resistance, and therefore, the V_{OUT} follows V_{IN}. V_{IN} of 15 volts turns the reed relay off and leads V_{OUT} to follow V_{DD}. The reed relays show a delay of ~32 μs during the transition from both on to off and off to on state, as shown in Figure 4-14(a) and (b) respectively. The switching delay arises from the inertia limited mechanical delay and the intrinsic electrical RC delay of the relays. As the printed reed relays have an extremely small resistance and capacitance, the delay mechanism is dominated by the mechanical delay.

(a)

$V_{DD}=2V$

100 kΩ

V_{OUT}

V_{IN}

(b)
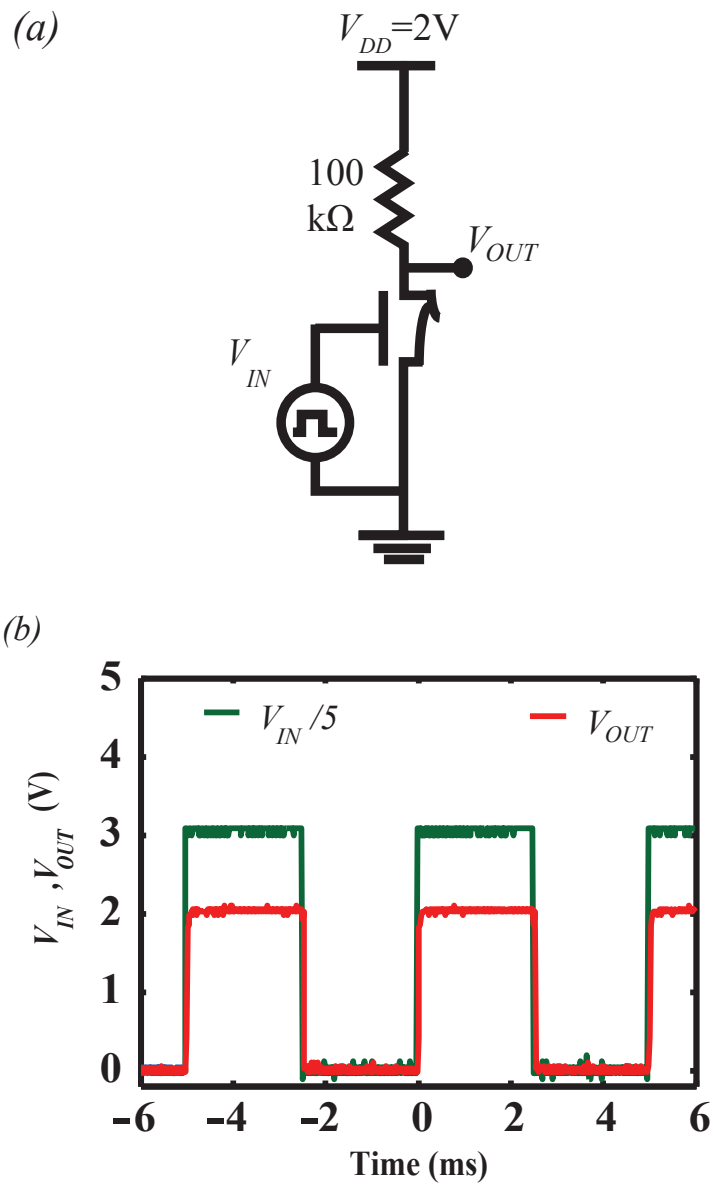
Figure 4-13. Dynamic behavior of the reed relays. (a) Reed relay connected to a 100 kΩ load resistor to construct a voltage buffer circuit, (b) output voltage (V_{OUT}) follows the input square wave (V_{IN}) with a frequency and amplitude of 200 Hz and 15 V respectively. Note that the amplitude of V_{OUT} is restricted to $V_{DD} = 2$ V due to the high current delivered by the low resistance reed.

(a)

(b)
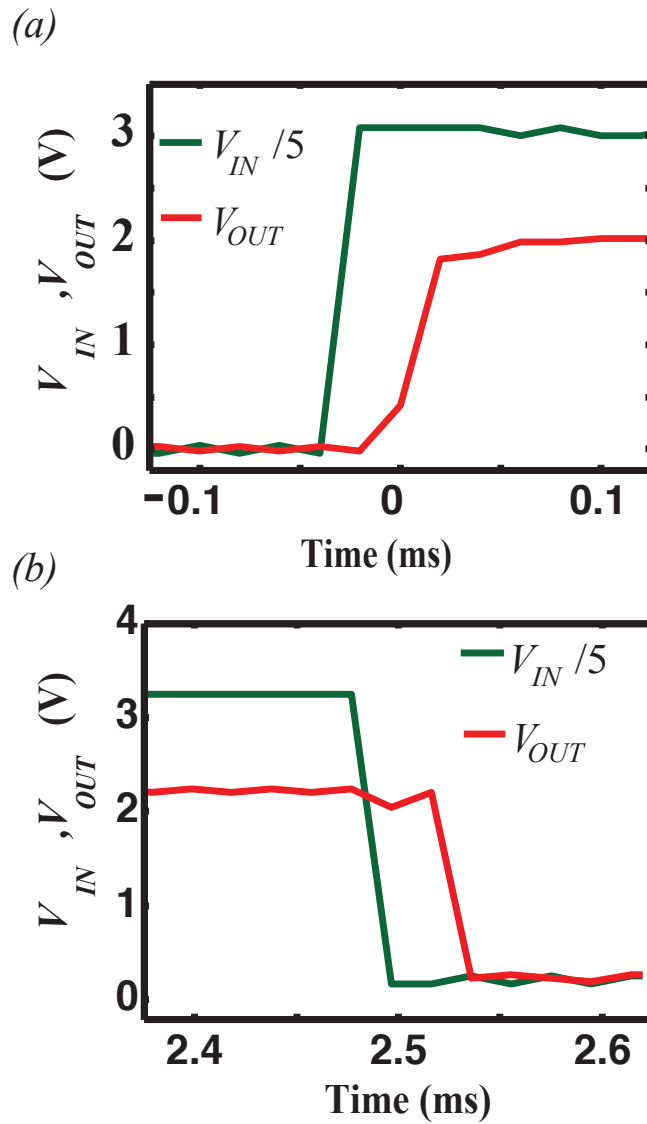
Figure 4-14. A turn-on and turn-off delay of ~32 μs is extracted from the plot (a) and (b) respectively.

4.3.3 Device Reliability

An endurance test for the printed reed relays demonstrated a lifespan of more than 10^5 cycles, with fatigue being the likely failure mechanism as the relays showed collapsed source reed at their end of life (see Figure 4-15).
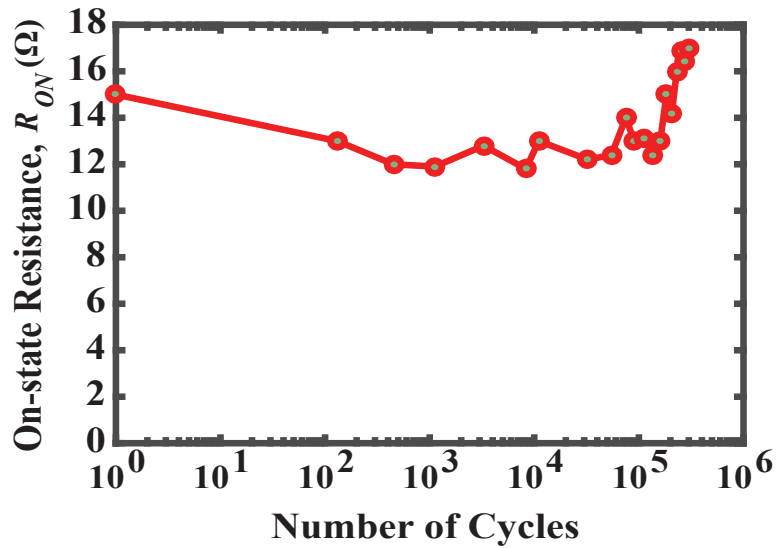
Figure 4-15. Endurance measurement of the reed relays shows that they can operate over 10^5 on/off hot switching cycles.

The reed relays were reproduced several times using the fabrication process presented in Figure 4-4 with varying reed relay geometrical parameters. The characteristics of the reed relays presented in this dissertation were found to be consistent across multiple devices and experiments. The electrical characteristics of the printed reed relays were measured using a semiconductor parameter analyzer (4155C from Agilent Technologies) in air. The thicknesses and surface profiles of the printed electrodes were measured using a surface profilometer (Dektak 6M, Veeco) and a white-light interferometer system (Wyko NT3300, Veeco). A FEI Nova NanoSEM 650 was used to obtain the scanning electron microscope (SEM) images.

4.4 Device Modeling

An analytical model for the reed relay was developed considering the upward bending moment in the source reed due to the residual stresses and the downward electrostatic force exerted by the applied gate voltage.
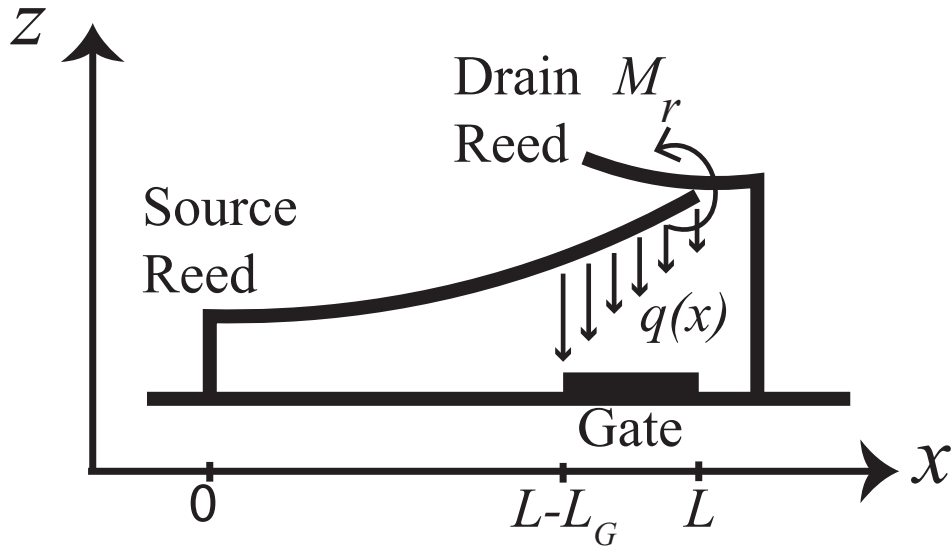
Figure 4-16. Analytical modeling of the reed relay. A non-uniform downward electrostatic force *q(x)* is applied on the source reed through gate bias. *q(x)* overcomes the upward force generated from the residual bending moment (M_r) existing in the source reed blocked by drain reed and moves the source reed downwards to turn the relay off.

Figure 4-16 depicts the side view of the reed relay, where $q(x), M_r, L_G$ and L denote the applied electrostatic load, residual bending moment of the source reed in the blocked state, length of the gate electrode, and designed length of the source reed respectively. We ignored the shrinkage of the source reed after release due to the in-plane tensile thermal stress since the reduction in length is negligible compared to the designed source reed length. The deflection of the source reed $\delta(x)$ with the applied moment (M) was defined using the differential beam bending equation [157], [159].

$$\bar{E}I\delta(x)'' = M,$$ Eq. 4-1

where, $\bar{E}, I$ and $\delta(x)''$ represents the bi-axial Young's modulus, moment of inertia and the second derivative of $\delta(x)$. $\bar{E} = E/(1-v)$, where E and v are the Young's modulus and the Poisson's ratio of the printed silver beam.

4.4.1 Young's Modulus of the Source Reed
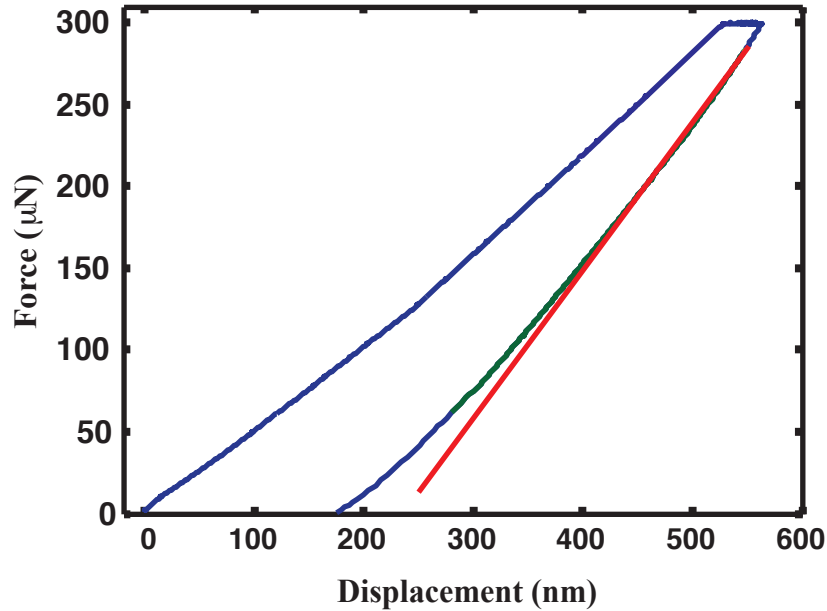
Figure 4-17. Reduced elastic modulus (*E*) of the printed silver film was extracted using nanoindentation technique by fitting the unloading portion of the curve to load equation; $E = (\pi^{1/2})/\{2[A_c(h)]^{1/2}\}$, where *h* and *A_c(h)* are the tip displacement and the contact area of the indenter tip. Inkjet-printed EMD 5730 Silver ink (from Sun chemicals) sandwiched between two PMMA layers and sintered at 140 ^{0}C showed a Young's modulus of 1.01 GPa.

Figure 4-17 shows the force-displacement curve obtained by applying a nanoindenter load to the printed Silver beam. The Young's modulus (*E*) was extracted using the Oliver-Pharr model by fitting the unloading phase of the force-displacement curve [160], [161]. The inkjet-printed source reed shows a low Young's modulus (*E*) of ~ 1.01 GPa due to the high porosity in the film [162], [163]. Note that, the source reed goes through a thermal sintering step where it is sandwiched between two PMMA layer. This changes the Young's modulus of the source reed from the value obtained in the case where the silver cantilever goes through thermal sintering step with the top of the cantilever exposed in the air. Although the presence of a gradient in porosity across the thickness of the source reed may cause a gradient in the elastic modulus, we assume a uniform Young's modulus measured using nanoindentation technique to preserve the simplicity of the model.

4.4.2 Moment of Inertia

The moment of inertia of a rectangular cross-section can be varied based on its axis of rotation. Figure 4-18 shows the same cross-sectional area with two different axis of rotation: one has the origin at one corner, another has origin at the center of the rectangle. The moment of inertia about the x-axis can be defined as

$$I_x = \int y^2 \, dA = \int_0^h y^2 b \, dy = \frac{bh^3}{3}$$ Eq. 4-2

The moment of inertia for the same cross-sectional area but about x'-axis can be defined as

$$I_{x'} = \int y^2 \, dA = 4 \int_0^h y^2 \frac{b}{2} dy = \frac{bh^3}{12}$$ Eq. 4-3

Note that, $I_{x'}$ is only 25% of I_x. Therefore, it is extremely important to calculate the moment of inertia about the correct axis of rotation.
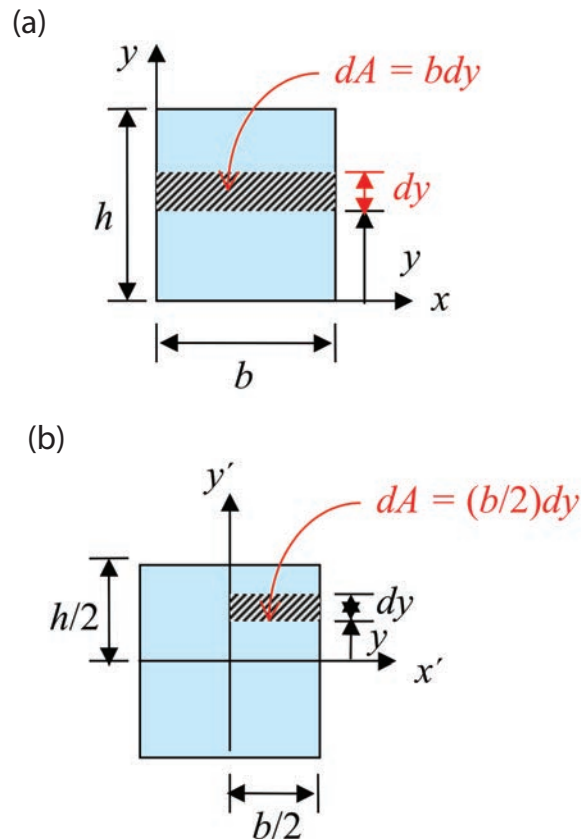
Figure 4-18. Rectangles having same area but different axis of rotation: (a) x-axis, (b) x'-axis.

Figure 4-19 shows the cross-section of a 4-pass printed Silver beam in x-z plane. The moment of inertia about the x-axis was defined as $I_x = 2 \int_0^h z^2 x dz$, where h is the peak height of the beam. The centroid of the beam is at $(0, \bar{z})$ coordinate, where $\bar{z} = \frac{\int_0^h z f(z) dz}{A_c}$. Here, A_c is the cross-sectional area of the beam. Note that the surface roughness of the source reed is negligible compared to the reed thickness and has insignificant impact on the variation in the cross sectional area. The moment of inertia about the x'-axis was evaluated using the parallel axis theorem as $I = I_x - A_c \bar{z}^2$. The moment of inertia for a rectangular cantilever is defined as [157] $I_r = W_r H_r^3 / 12$, where W_r and H_r denotes the width and height. Considering W_r as the base width of the printed source reed (W), an equivalent rectangle height for the source reed can be estimated by setting $I_r = I$, which was defined as the effective thickness of the source reed (H_E).
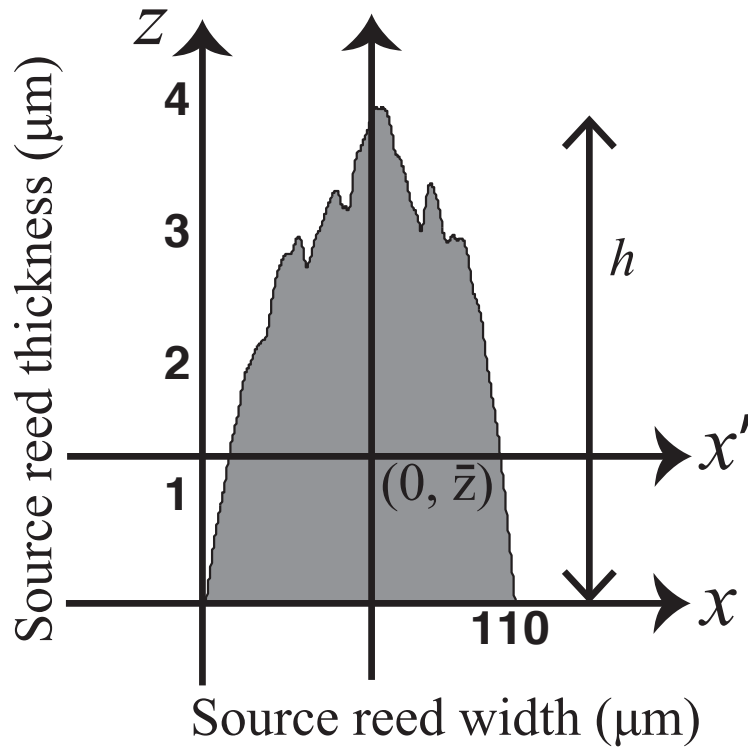
Figure 4-19. Gray area shows the cross section of the 4-pass printed source reed where $(0, \bar{z})$ is the centroid of the beam. The moment of inertia is evaluated about x'-axis.

77

4.4.3 Model of the Turn-Off Voltage

The applied electrostatic load on the source reed was expressed using the applied gate bias (V_{GS}) and the variable actuation gap along the x-axis ($g(x)$) as [159], [164]

$$q(x) = \frac{\epsilon W}{2}\left(\frac{V_{GS}}{g(x)}\right)^2, \qquad\qquad \text{Eq. 4-4}$$

where, ϵ is the permittivity of the air. $g(x) = g_0 + \delta_B(x)$, where g_0 and $\delta_B(x)$ represents the non-curled air gap and the upward deflection of the source reed along the x-axis due to curling in the blocked condition. Considering a uniform bending moment due to the stress gradient in the source reed, $\delta_B(x) = (\delta_{LB}/L^2)x^2$; where δ_{LB} is the tip deflection of the blocked source reed. Since the source reed cannot get rid of all the stresses after release due to the curling limitation imposed by the drain reed, a residual bending moment stays in the beam; which was expressed as

$$M_r = \frac{2(\delta_{LF}-\delta_{LB})\bar{E}I}{L^2}. \qquad\qquad \text{Eq. 4-5}$$

Here, δ_{LF} is the tip deflection of the source reed in free-curling state, which was measured from a separate cantilever structure on the same wafer. Table 4-3 presents the measured free curling and blocked tip deflection of the source reed with varying source reed lengths and effective thicknesses.

The downward tip deflection of the source reed due to only the applied electrostatic load was expressed as [159], [164]

$$\delta_{LES} = \int_{L-L_G}^{L} \frac{x^2}{6\bar{E}I}(3L-x)q(x)dx. \qquad\qquad \text{Eq. 4-6}$$

The upward tip deflection of the source reed considering only the residual bending moment was expressed as

$$\delta_{LRBM} = \frac{M_r L^2}{2\bar{E}I}. \qquad\qquad \text{Eq. 4-7}$$

Considering the superposition of all the loads, the resultant tip deflection of the source reed is expressed as $\delta_L = \delta_{LES} - \delta_{LRBM}$. As the source reed is required to pull down a very small distance to separate it from the drain reed, we defined the tip deflection for turning off the device as $\delta_L = \delta_{LTOF} = 10$ nm. Considering the above equations, the gate voltage at which the reed relay turns-off was therefore calculated to be

$$V_{TOF} = \sqrt{\frac{\delta_{LTOF} + (\delta_{LF}-\delta_{LB})12\bar{E}I}{\epsilon W \int_{L-L_G}^{L} \frac{x^2(3L-x)}{g(x)^2} dx}}. \qquad\qquad \text{Eq. 4-8}$$

(a)

(b)
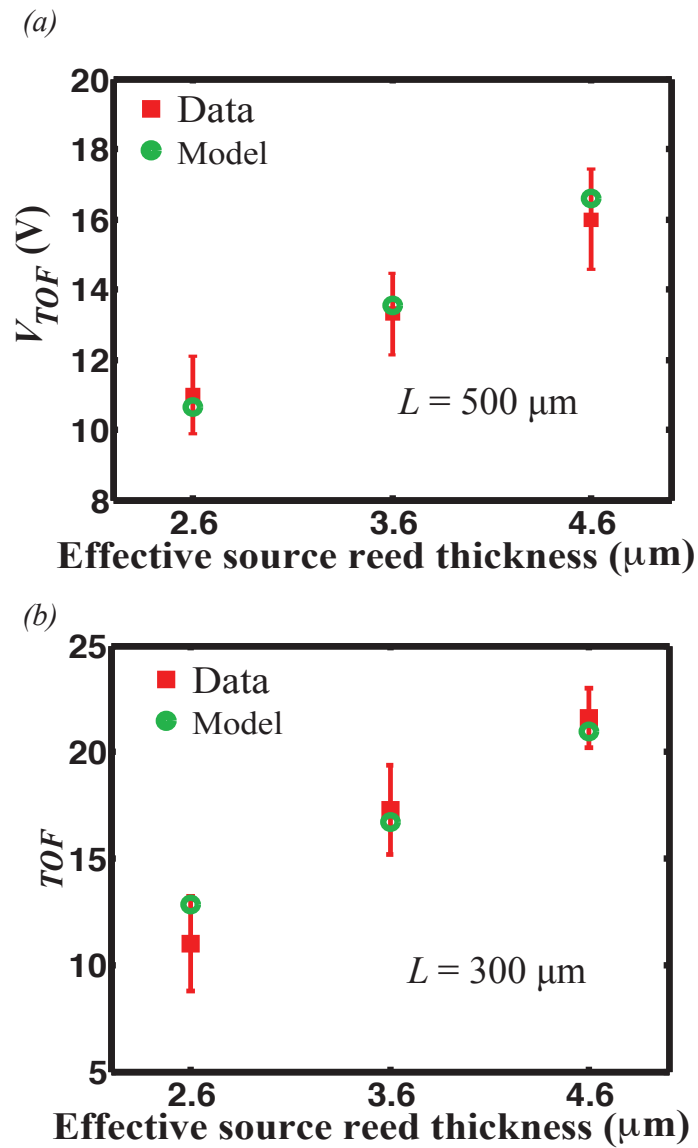
Figure 4-20. Turn-off voltage (V_{TOF}) with varying effective source reed height validates the model with experimental data for source reed lengths of (a) 500 μm and (b) 300 μm respectively.

Figure 4-20(a) and (b) shows a very good agreement between the model and the experimental turn-off voltage data for source reed lengths of 500 μm and 300 μm respectively. The design parameters for the devices shown in Figure 4-20(a) and (b) are summarized in Table 4-4. The good agreement between the model and experiment support our understanding of the implications of residual stress and of relay operation.

	Value					
Source reed tip deflection	$L = 500$			$L = 300$		
	$H_E = 2.6$	$H_E = 3.6$	$H_E = 4.6$	$H_E = 2.6$	$H_E = 3.6$	$H_E = 4.6$
Free curling	50	40	35	21	17	15
Blocked	5	4.1	3.5	5	4.1	3.5

Table 4-3. Measured source reed tip deflection in free curling and blocked state with varying source reed length (L) and effective thickness (H_E) for the devices presented in Figure 4-20(a) and (b). All the values are in μm.

Parameter	Value
Gate actuation Area	165 μm x 110 μm
Non-curled air gap between source reed to gate	1.5 μm
PVP dielectric thickness	500 nm
Source reed width	110 μm
Source reed effective thickness	[2.6, 3.6, 4.6] μm
Drain reed: length x width x thickness	150 μm x 120 μm x 9 μm

Table 4-4. Designed parameters of the printed reed relays of Figure 4-20(a) and (b).

In this chapter, a novel stress-tolerant three terminal reed relay is demonstrated with zero off current, a very low on resistant (< 15 Ω) and a moderate switching delay (~32 μs). This level of performance is excellent, and exceeds the achievable on-off performance of TFTs, making this device extremely promising for display applications. Furthermore, the fully printed nature of the process, and the immunity to stress variations makes this structure significantly more scalable than past efforts in this regard, thus providing a path to applications in realistic large area systems. However, three terminal relays are not suitable for logic circuit design, especially in circuits, where

two or more relays are connected in series. The relay actuation voltage must be independent of the source and the drain voltage to avoid electrically floating electrodes issue. Therefore, a four terminal relay design is necessary for logic circuits. The next chapter provides a fully printed process flow for four terminal relays including their electrical characterization. Similar to the three terminal relays, the design of novel architecture for four terminal relays also utilizes stress generation in printed thin films.

Chapter 5: Fully Inkjet-Printed Four Terminal Microelectromechanical Relay

5.1 Purpose of Four Terminal (4T) Relay

Four terminal (4T) relays have several advantages over three terminal (3T) relays. 4T relays are necessary to design a logic circuit where more than one relay is connected in a series configuration. Figure 5-1(a) shows a complementary NAND logic using 3T relays where the pull-down network consists of two relays connected in series.
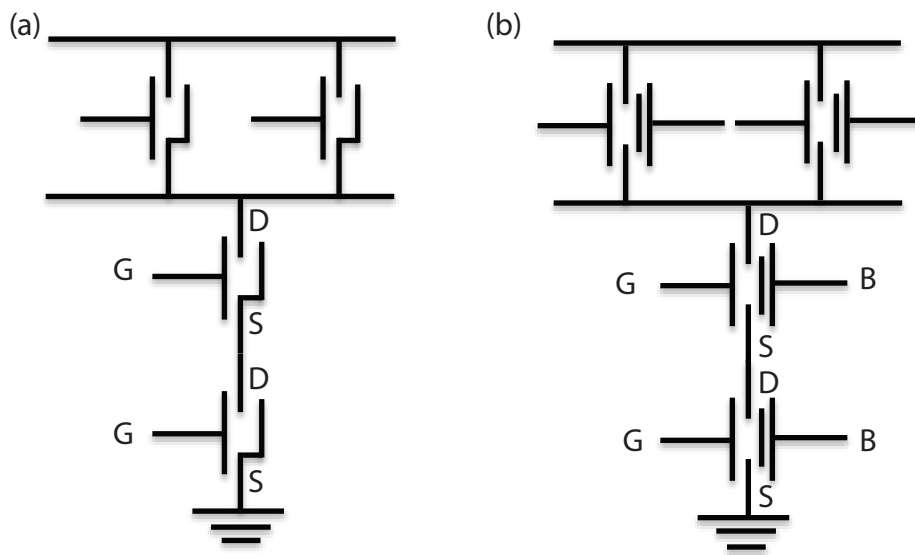
Figure 5-1. Complementary NAND logic circuit using (a) 3T MEM relay, (b) 4T MEM relay

If the bottom relay in the pull-down network remains off, the source of the top relay remains floating. Therefore, the actuation voltage in the top relay is not uniquely defined as in 3T relay the voltage difference between the gate and source terminal defines the actuation of the movable beam. Four terminal relay solves this problem by adding a body terminal in the relay structure (see Figure 5-1(b)). In the 4T system, device actuation is performed using the voltage difference between the

gate and the body terminal; therefore, the switching voltage is independent of the source or drain voltage.

One of the major motivations behind the development of microelectromechanical (MEM) relays was to construct low-power devices utilizing abrupt switching characteristics. The switching voltage should be as low as possible for reduction of the dynamic power dissipation through complete utilization of the abrupt switching of MEM relays. 4T relays have the flexibility to tune the switching voltage by using a body bias and potentially can provide low-voltage and low-power operation. The tuning capability of switching voltage also allows the same 4T relays to perform either as a pull-down or pull-up device; hence, purely complementary logic circuits can be implemented using the 4T relays [88], [90]. Chung et al. demonstrated the first printed 4T MEM relay with spin-coated PMMA sacrificial layer and two-step post and beam printing process [20]. A fully printed process flow is required for low-cost processing and better area scalability.

5.2 Basic Relay Configuration

Figure 5-2 illustrates two basic configurations of the 4T relay. The movable body beam is actuated using a gate bias. The body beam is attached to a conducting channel through an insulating layer. This insulating layer is termed the body dielectric, which needs to provide electrical isolation and mechanical adhesion between the body and the channel. The channel moves with the actuation of the body electrode and can make or break the connection between the source and the drain terminal to turn the relay on or off.

In the relay configuration of Figure 5-2(a), body beam, body dielectric and channel are connected in a stack configuration. Stack configuration provides a strong mechanical attachment between the body beam and the channel. However, the processing of this configuration is difficult due to the high topography. In contrast, the relay configuration of Figure 5-2(a) uses a glued configuration to connect the body beam, body dielectric and channel. The glued configuration has less mechanical integrity between the body and the channel, but has the advantage of simple processing with less process steps.

5.3 Inkjet-Printed Body Dielectric

The body dielectric is a very important part of the 4T relay. A careful choice of material is required for the body dielectric. The body dielectric material should provide good electrical isolation between the body and the channel. It also should have very good adhesive properties to form a strong mechanical tie between the body and the channel. For a fully printed 4T relay process, the body dielectric material has to be solution processable and printable. Also, the solvent for the dielectric material must not etch the structural and sacrificial materials, and the sacrificial etchant

must not etch the body dielectric material. The body dielectric material should be curable at low temperature to avoid any possible thermal damage of the structural or sacrificial materials.
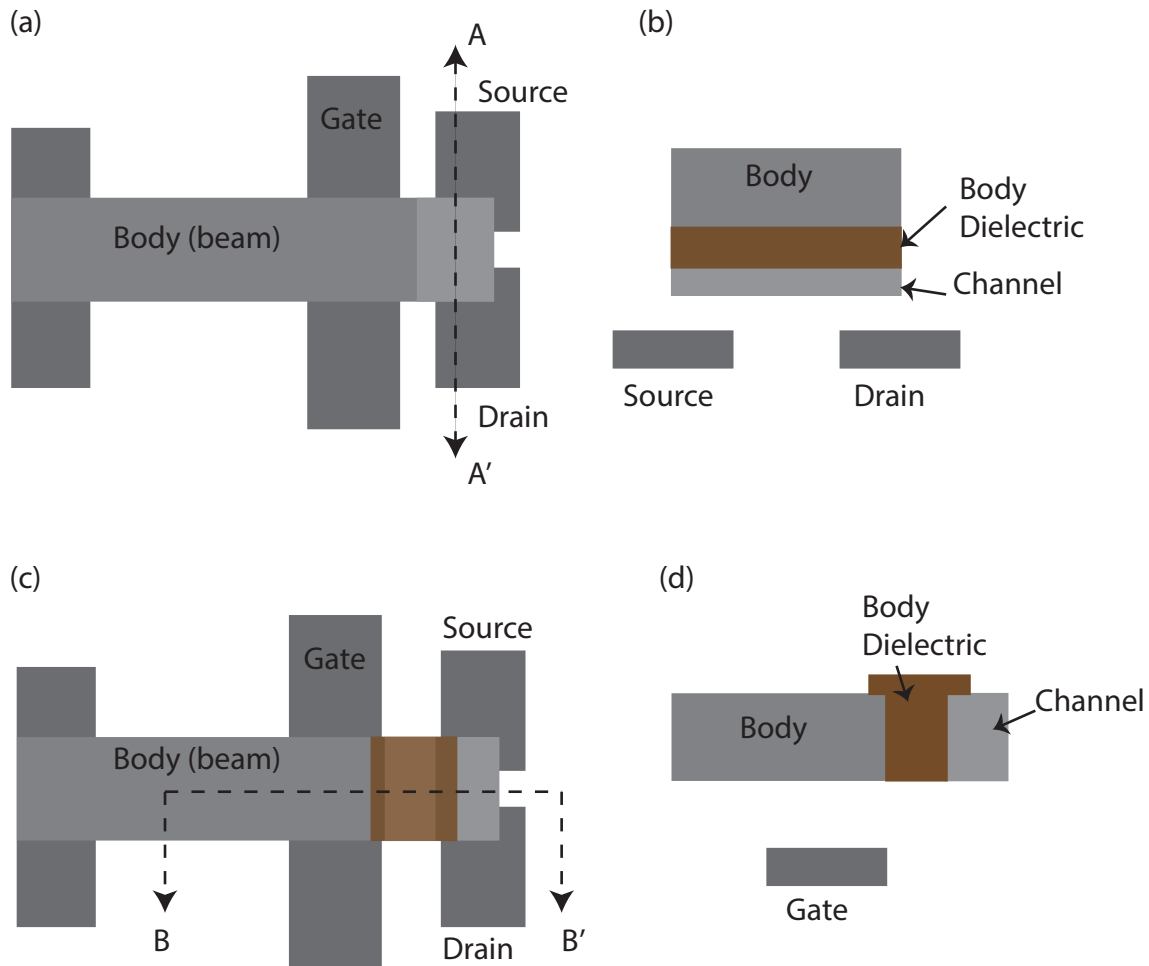
Figure 5-2. Basic configurations of the four terminal relays. (a) Body beam, body dielectric and channel are connected in a stack configuration, (b) cross-sectional view along A-A'. (c) Body beam is glued to the channel using body dielectric, (d) cross-sectional view along B-B'.

Considering all the requirements for the body dielectric materials, SU-8 was chosen for the body dielectric material. As discussed in chapter 3 and 4, a nanoparticulate silver film and PMMA were used for the structural and sacrificial materials for printed MEMS, respectively. SU-8 solvent does not etch either the PMMA or the silver film. SU-8 is solution processable and can be cured at low

temperature (less than 100 ^{0}C). However, SU-8 needs a UV curing step for cross-linking. The required UV exposure dose is small; and hence, PMMA does not get damaged during the UV curing step. During the release step, acetone etches PMMA but does not etch cross-linked SU-8. Also, SU-8 is a strong adhesive, which is a very important property in the scheme of 4T relay configuration .SU-8 2002 MicroChem has a mass loading of 29 wt% and has the right viscosity (7.5 cPs) for inkjet-printing. Table 5-1 presents the physical properties of the SU-8, 200 series from MicroChem.

SU-8 200 series	% solids	Viscosity (cPs)	Density (g/ml)
2000.5	14.3	2.49	1.070
2002	29.0	7.5	1.123
2005	45.0	45	1.164

Table 5-1. Physical properties of SU-8 2000 series from MicroChem

(a)   (b)
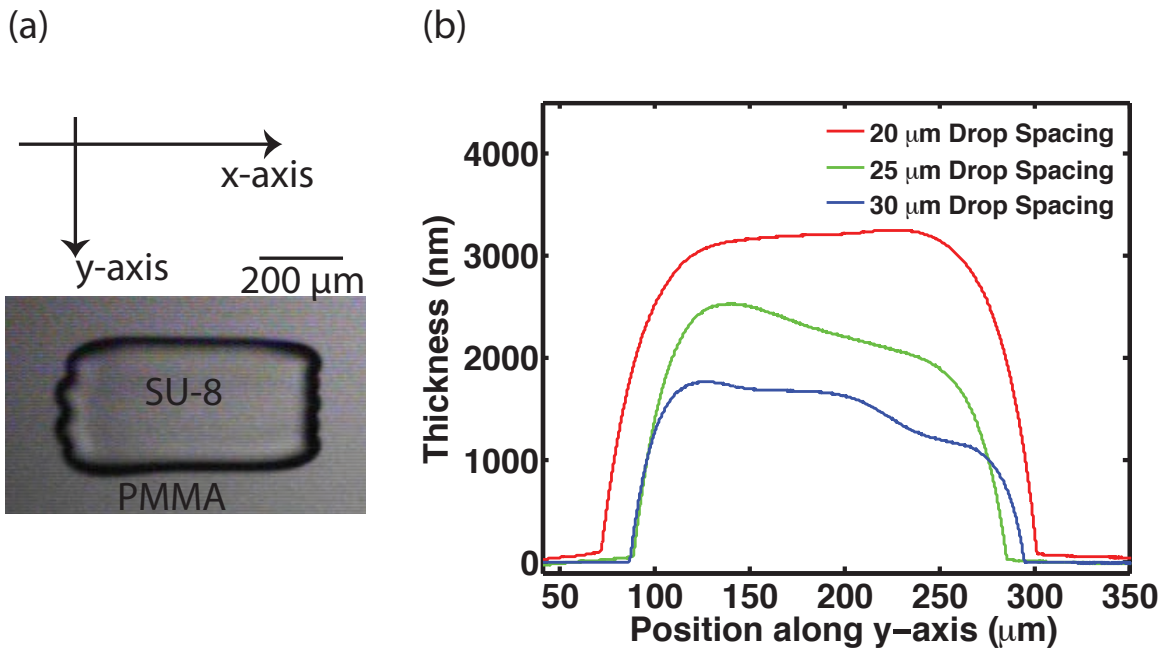
Figure 5-3 (a) Inkjet-printed SU-8 on PMMA surface. (b) Thickness profile of printed SU-8 for various drop spacing.

Reliable jetting of SU-8 2002 was observed using Fujifilm Dimatix cartridge with 10 pl droplet volume. High fidelity of printed pattern was also observed. After printing, SU-8 was soft baked at 95 ^{0}C for 2 min on a hotplate. After that, the sample was exposed to a UV light source for photo-initiated cross-linking of SU-8. This cross-linking step increases both electrical and mechanical strength of the SU-8 dielectric. Finally, a post exposure baking of the sample was carried out at 95 ^{0}C for 2 min on a hotplate. Figure 5-3 shows that SU-8 2002 printed with 20 μm drop spacing produces a very smooth pattern when printed on the PMMA surface.

5.4 Fully Printed Architectures and Process Development

As discussed in the chapter 3 and 4, inkjet-printed silver cantilevers curl in the upward direction after release due to a stress gradient in the film. Therefore, a stress-tolerant structure is necessary for good relay performance. Figure 5-4 shows two stress-tolerant 4T relay structures based on the basic relay configurations discussed in section 5.2. Here, the suspended source and drain beam block the curling of the channel, which is attached to the body beam through a body dielectric. SU-8 is used as the body dielectric in the 4T relay process. The channel is extended along the width direction of the body beam to make contact with both source and drain beam during the curling process. In architecture 'S1', the body beam, body dielectric and channel are connected in a stack configuration; and in architecture 'G1', the body beam is glued to the channel using the body dielectric. The intended operation of these relays is as follows. Both of these relay architectures are normally closed, i.e. the relays are normally in the on-state. The electrostatic actuation between the body and the gate pulls the body beam in the downward direction. The body beam also pulls the channel with it in the downward direction turning the relay off.

Figure 5-5 shows the SEM image of the fabricated 4T relay with S1 architecture. The body beam curls in the upward direction after release. The channel also curls up along with the body beam. Unfortunately, the curling of the channel was blocked by only the source or the drain beam, due to the uneven height of the source and the drain beam. Hence, the channel does not make contact with the source and the drain beam in the as-fabricated condition. Electrical measurements ensured an open connection between the source and the drain beam in the as-fabricated state. The relay fabricated with G1 configuration also showed similar behavior. The relays fabricated with both S1 and G1 architectures do not perform as intended due to the processing difficulties. Fabricating the perfectly even suspended source and drain beam is very difficult, especially using the printing process. Therefore, a modification in the relay configuration is necessary where only one suspended beam is used to block the curling of the body beam.

Figure 5-6 shows the schematic of the 4T relay architecture 'S2' and 'G2'. In the S2 architecture, the source beam is attached with the body beam through the body dielectric in the stacked configuration. In G2 architecture, the source beam is glued onto the body beam using the body dielectric. Both of these 4T relay architectures have the same device operations. The composite

beam consisting of the body beam, body dielectric and source beam bends in the upward direction after release. The upward bending of this composite beam is blocked by the suspended doubly clamped drain beam, which is placed over the source beam. In normal device operation, the source and the drain beams are initially in contact with each other. The body beam pulls the source beam with it in the downward direction when an electrostatic actuation is applied between the body and the gate, which turns the relay off.
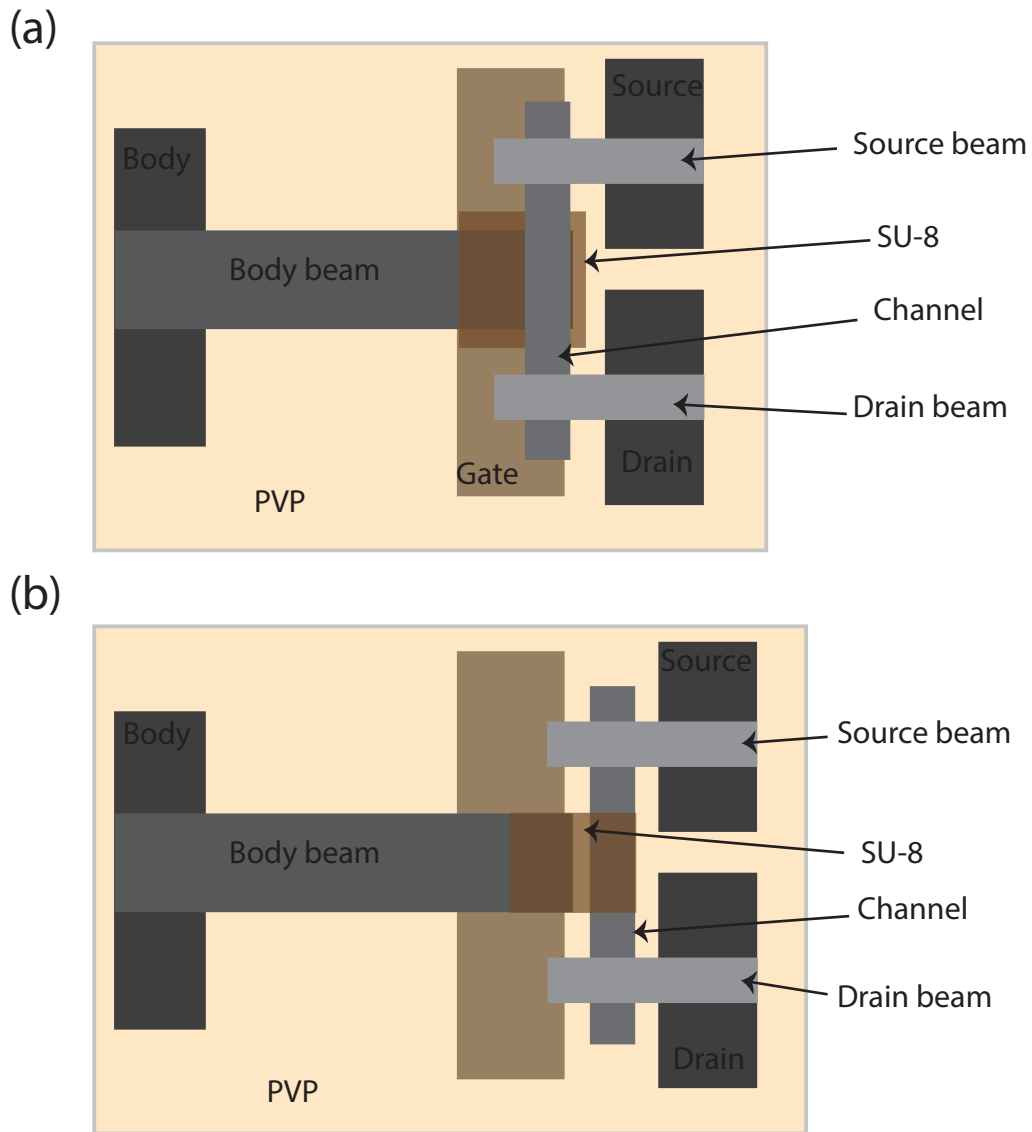
Figure 5-4. Stress tolerant four terminal relay configurations. (a) 'S1' architecture: The body beam, body dielectric and channel are connected in a stack configuration. (b) 'G1' architecture: The body beam is glued to the channel using the body dielectric
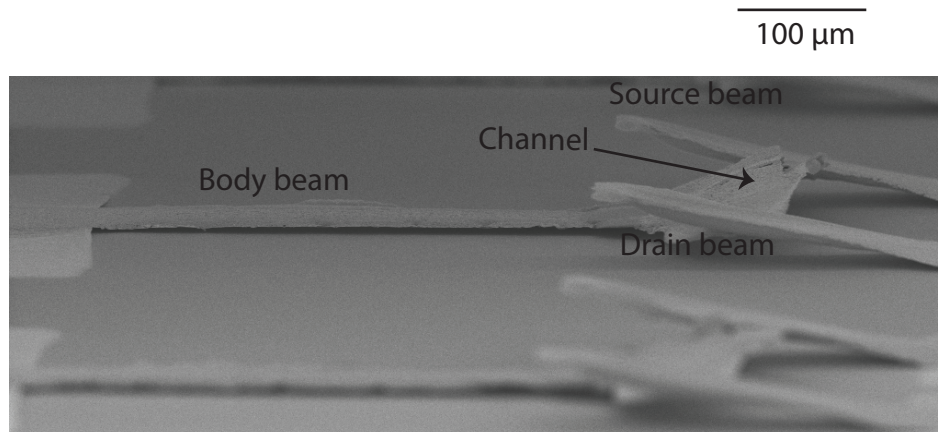
Figure 5-5. SEM image of the fabricated 4T relay with S1 architecture. Due to the uneven height of the source and the drain beam, curled up channel can not make connection between them.

Figure 5-7(a) shows the SEM image of the 4T relay fabricated using the S2 architecture zoomed in the stack region. The SEM image in Figure 5-7(b) shows that the composite beam collapsing near the stack region. This occurs due to the collapsing of the overhung SU-8 along the width direction of the body and the source beam. A slight overhang is required in the stacked structure to prevent the shorting between the body and the source beam.

Figure 5-8(a) shows the SEM images of the 4T relay fabricated using the G2 architecture. Figure 5-8(b) shows the zoomed-in image near the glued region. In the glued configuration, there is no overhung SU-8 and the composite beam is suspended after release. As intended, the source and the drain beams are normally in contact. This was confirmed by the electrical measurements. The movement of the body beam with the electrostatic actuation between the body beam and the gate was observed through an optical microscope. Unfortunately, the SU-8 glue was not strong enough so that the body beam could pull the source beam with it. Also, the stress developed in the SU-8 layer causes the silver beam to deform and take a bow-shape along the width direction after release.

A modified fully printed and stress tolerant 4T architecture 'SG' was developed combining the stacked and the glued configuration, which addresses all the issues related with the S1, S2, G1 and G2 architectures.
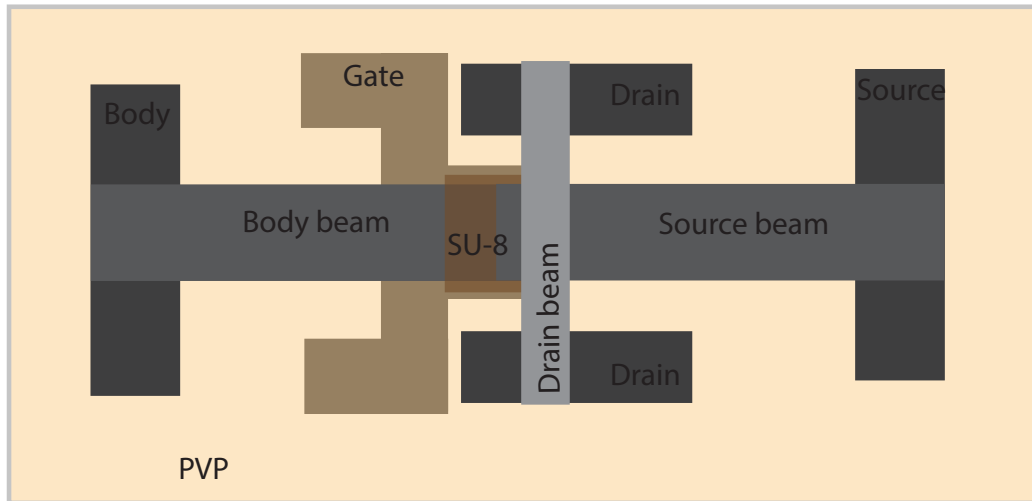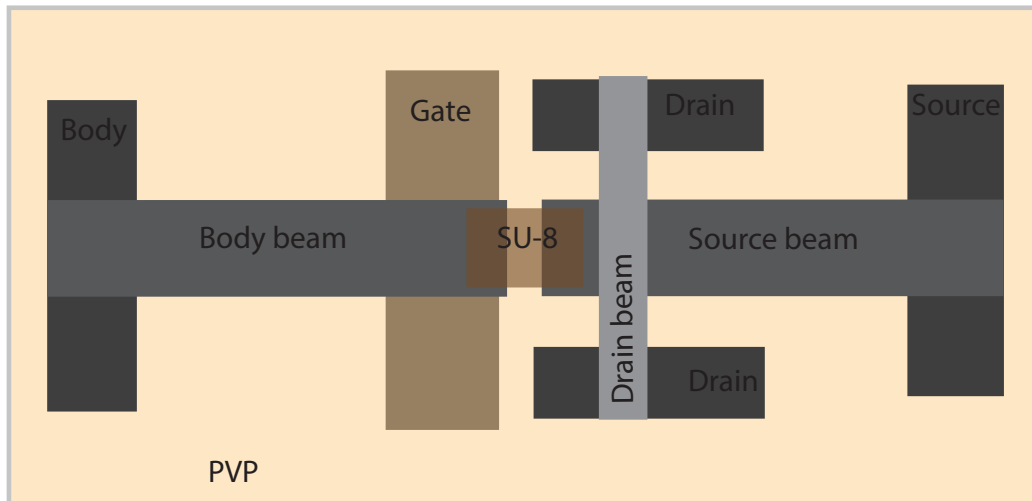
Figure 5-6. Stress tolerant relay: A doubly clamped drain beam is used to block the composite beam consisting of the body beam, body dielectric (SU-8) and the source beam. (a) The source beam is attached with the body beam through the body dielectric in the stacked configuration. (b) The source beam is glued with the body beam using the body dielectric

Figure 5-9 illustrates the schematic of the 4T relay with SG structure. The body and the source beam contain a wider section near the tip. These wider portions of the body and the source beam provide more SU-8 overlap area. The SU-8 is used to glue the body and the source beam. A small

overlap between the body and the SU-8 along the beam length direction helps to avoid bowing of the body beam and ensures better electrostatic actuation. Similar to the stacked configuration, a top silver patch is used for the stronger bonding between the body and the source beam. A doubly clamped drain beam, placed over the source beam, is used to block the upward bending of the composite beam consisting of the body beam, SU-8, silver patch, and source beam after release.

(a)
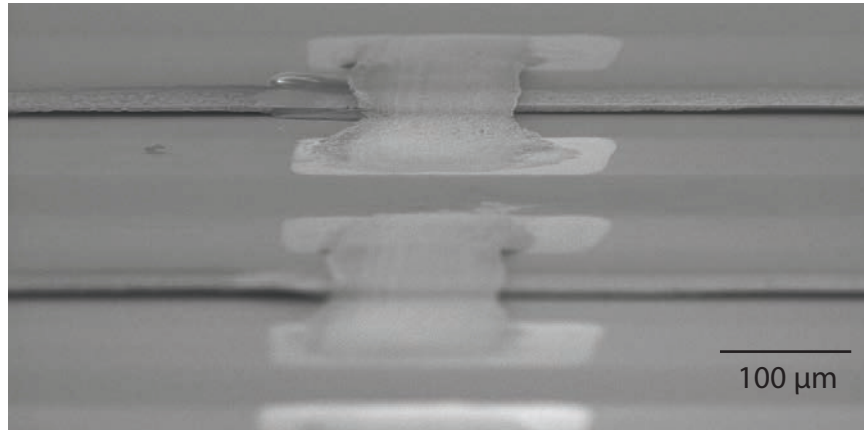
(b)
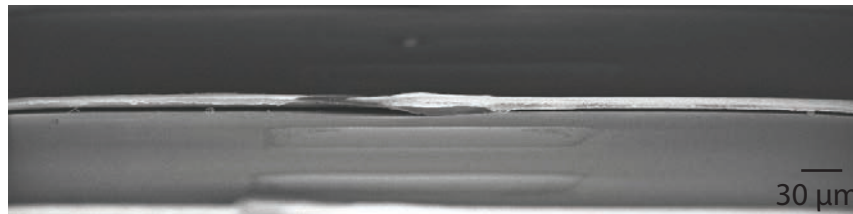
Figure 5-7. SEM images of 4T relay made with S2 architecture. The stack of the body beam, SU-8 and the source beam collapses near the overhung SU-8 region after release. Zoomed-in image of the relay (a) with blocking drain beam, (b) without drain beam.

Figure 5-10 illustrates the fabrication process flow of the 4T relay with SG architecture. The gate electrode was inkjet-printed on an oxidized silicon substrate using silver nanoparticle ink and sintered at 180 ^{0}C for 30 min on a hotplate. A PVP layer was used as the gate dielectric layer. The PVP layer was cross-linked at 230 ^{0}C for 30 min. The body, drain and source electrodes were inkjet-printed on the PVP layer using the same nanoparticle ink and sintered at 180 ^{0}C for 30 min. After that, the first PMMA sacrificial layer (PMMA1) was inkjet-printed between the body and the source electrodes and annealed at 180 ^{0}C for 10 min. A 40 W, O2 plasma treatment was carried

90

(a)

100 μm

(b)

20 μm
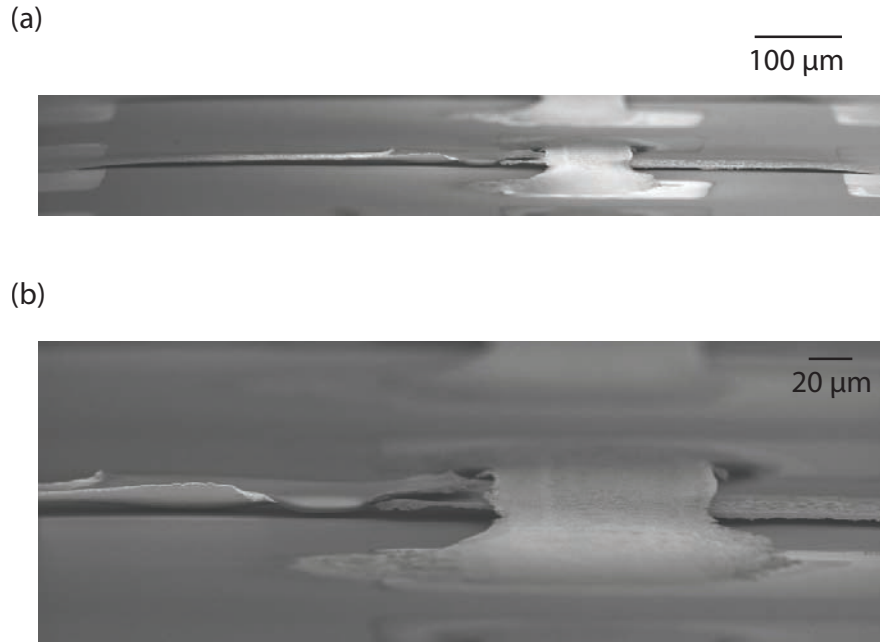
Figure 5-8. (a) SEM image of the 4T relay fabricated using G2 architecture. (b) zoomed-in near glued region. The body beam can not pull the drain beam down with it due to a lack of strong dielectric glue. Also, the stress built up in the SU-8 layer forces the silver beam to take bow-shape along the width direction.
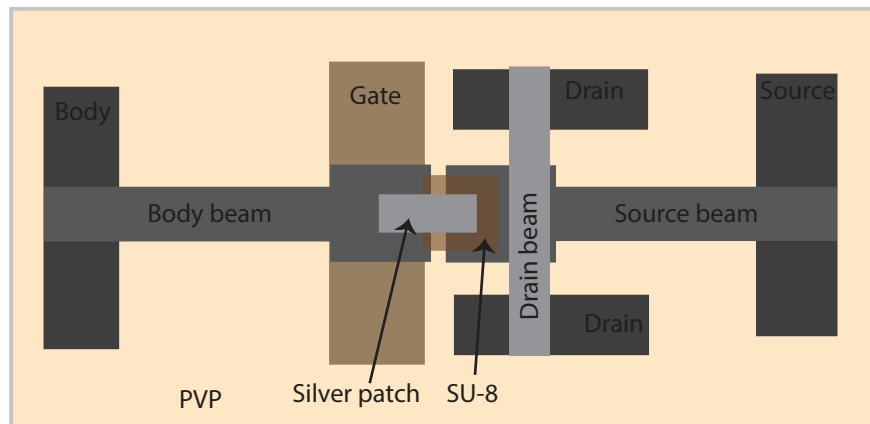
Figure 5-9. Stress tolerant 4T relay. The body beam and the source beam are attached using SU-8 dielectric glue and this attachment is fortified by a top silver patch.
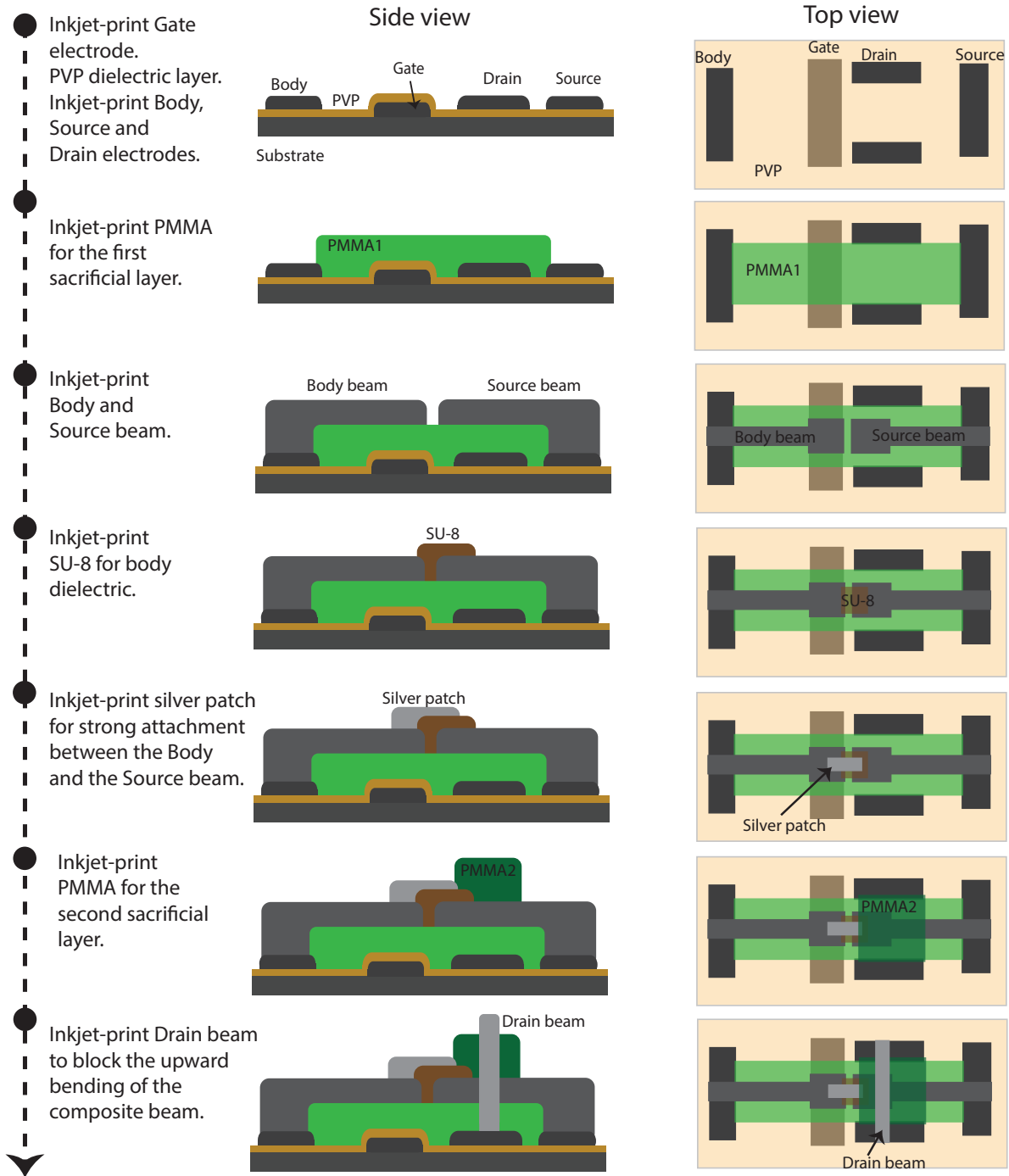
Figure 5-10. Process flow of the stress-tolerant 4T relay with SG architecture. Release of the structure by dissolving PMMA in acetone is not shown here. Schematic is not drawn to the scale.

out to modify the PMMA surface properties for better wetting of the silver ink. The body and the source beam were inkjet-printed on top of the PMMA1 layer using EMD 5730 silver ink. A 4-pass

silver beam printing was carried out for both the body and the source beam with interspersed drying at 120 ^{0}C for 5 min. The beams were sintered at 150 ^{0}C for 15 min. SU-8 layer was inkjet printed to glue the body and the source beam. SU-8 was soft baked for 95 ^{0}C for 2 min, UV treated for 30 s and post-exposure baked at 95 ^{0}C for 2 min.

A silver patch was printed on top of the body beam and the SU-8 layer for stronger attachment between the body and the source beam. Then a second PMMA sacrificial layer (PMMA2) was inkjet-printed between the two drain pads and annealed at 150 ^{0}C. The doubly clamped drain beam was inkjet-printed using silver nanoparticles ink. A 4-pass printing was employed with interspersed drying at 120 ^{0}C for 5 min. The drain beam was sintered at 150 ^{0}C for 15 min. All the heating process was done on a hot plate. Finally, the structure was released by dipping the sample in a hot (40 ^{0}C) acetone bath. The PMMA layers were dissolved in acetone in this step. After release, the sample was washed using IPA and transferred into a critical point drying (CPD) chamber to dry.
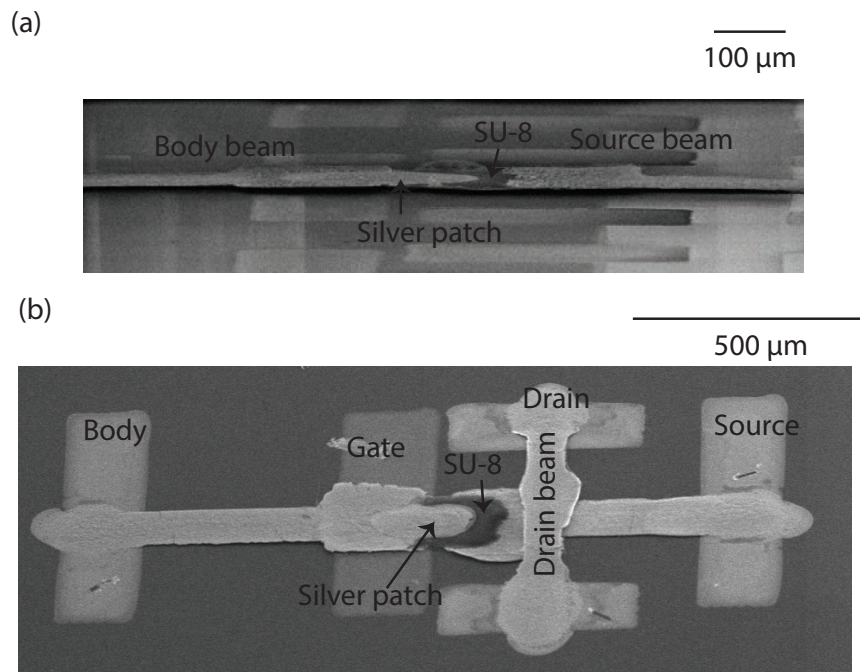
Figure 5-11. (a) SEM image of the suspended composite beam consisting of the body beam, SU-8, source beam and silver patch. (a) SEM image of the fully printed stress-tolerant 4T relay.

Figure 5-11(a) shows the SEM image of a suspended composite beam consisting of the body beam, SU-8, silver patch, and source beam. Figure 5-11(b) shows the SEM image of the full 4T relay.

93

This relay showed good switching operation. The electrical characterization of the 4T relay fabricated with SG structure is discussed in the next section.

5.5 Device Characterization
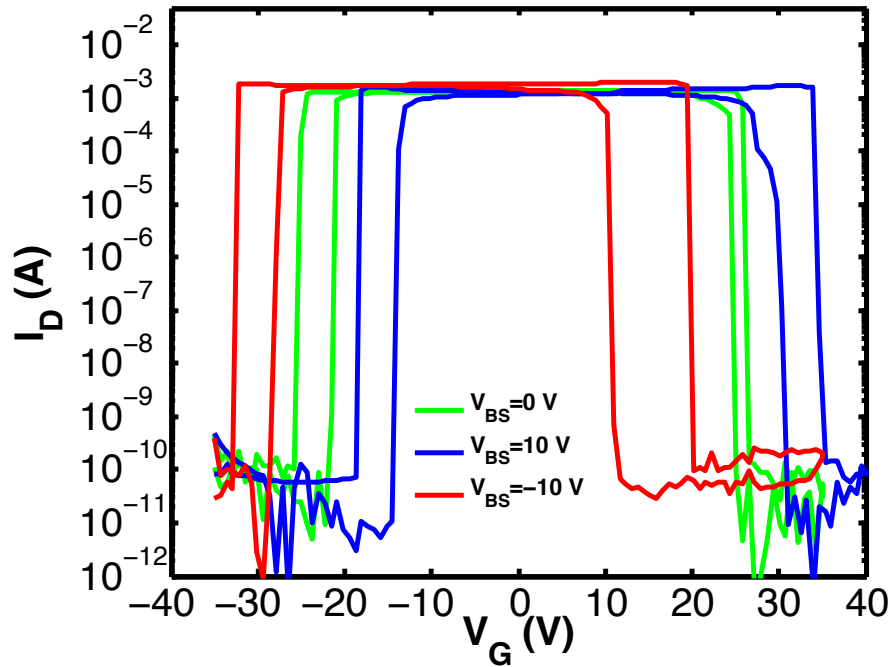
Figure 5-12. I_D-V_G characteristics of the fully printed stress-tolerant four terminal relay fabricated using SG architecture.

Figure 5-12 shows the I_D-V_{GS} characteristics of the fully printed and stress-tolerant 4T relay fabricated using SG architecture with different body biases (V_{BS}). The gate voltage (V_{GS}) was swept from -40 V to +40 V. The as-fabricated relay is in the on-state. At zero body bias the relay turns off when a V_{GS} of ~26 V was applied. The gate voltage at which the relay turns off is defined as the turn-off voltage (V_{TOFF}). This turn-off voltage can be tuned using the body bias. A +10 V body bias increases the V_{TOFF} to ~34 V and shifts the I_D-V_{GS} curve to the right. A -10 V body bias decreases the V_{TOFF} to ~19 V and shifts the I_D-V_{GS} curve to the left. Note that the turn-off voltage is not tuned properly with the body bias. The relationship between the applied body bias and the shift in the turn-off voltage should be linear with a slope of +1. This suggests the existence of

94

parasitic actuation in the relay architecture. Further investigation is required to address this issue. Also, a detailed reliability study needs to be conducted on this relay.

In this chapter, a novel stress-tolerant and fully printed four terminal MEM relay is demonstrated with zero off-state leakage and low on resistance. The hyper-abrupt switching feature of these relays allows for low power logic design. The threshold voltage tuning capability of these relays is demonstrated. This feature provides n-type and p-type relays for CMOS-like logic implementation. The fully printed nature of these four terminal relays is well suited for the implementation of logic operations in low-cost and large-area electronics.

The next chapter will summarize the contribution of this work and discuss the future directions of printed MEMS.

Chapter 6:   Conclusions and Future Work

6.1 Conclusions

In this dissertation, advancement in various aspects of printed MEMS were achieved through comprehensive studies on multiple levels of printed MEMS including printability and characterization of materials, process development and device characterization. The studies presented in this dissertation are as follows.

The materials for the fully printed MEMS processes were identified and their printability was studied. Nanoparticle based silver ink was used to fabricate MEMS structures; Cross-linked PVP, PMMA and SU-8 was selected as the gate dielectric, sacrificial layer and the body dielectric materials respectively. It was found that lowering the molecular weight (MW) of the polymer solute provides vast improvement in the jetting performance. A higher jettable mass loading window of the ink formed from low MW polymers helps to reduce the coffee ring effect. Also, high boiling point and low vapor pressure of the solvent is required to ensure stable jetting of the ink by eliminating nozzle clogging issue.

A systematic mechanistic study on the development of stress gradients in the inkjet-printed silver nanoparticles film was performed. The strain gradient along the thickness of the film was measured from the radius of the curvature of the cantilevers. Auger electron spectroscopy (AES) measurement showed a higher amount of residual carbon from the polymer stabilizer near the bottom of the film than the top of the film, which was verified by the energy-dispersive X-ray spectroscopy (EDS) measurement. The scanning electron microscope (SEM) image showed a higher coarsening with higher porosity at the bottom of the film. A lower Young's modulus suggests the domination of non-densifying over densifying diffusion mechanism at the bottom of the film, which causes less tensile stress at that region than the top of the film. This understanding of the evolution of stress gradient in printed nanoparticles film denotes a significant contribution towards the enhancement and reliability of printed electronics with special interest in the progress of printed MEMS.

A fully inkjet-printed microelectromechanical (MEM) reed relay was demonstrated offering excellent switching characteristics and good mechanical endurance with a novel device architecture to provide immunity to stress variation in the cantilevers. The printed reed relays exhibit a very low on-resistance, immeasurable off-current, hyper-abrupt switching and a good switching speed. We also developed an analytical model to determine the turn-off voltage of the reed relays considering the residual bending moment acting on the blocked source reed and non-uniform electrostatic gate actuation field, which shows very good agreement with the experimental

data. Due to the extensive use of printing and the inherent stress tolerance of the realized structure, the demonstrated reed relays are attractive candidates for low-cost and large-area applications.

Finally, a process flow for the fully printed stress-tolerant four terminal MEM relay was proposed. This 4T relay not only shows low on-resistance, immeasurable off-current and hyper-abrupt switching but also provides switching voltage tuning capabilities. Switching voltage tuning capabilities offer low power switching and complementary relays. Therefore, this fully printed 4T relay is well suited for the implementation of logic operations in low-cost and large-area electronics.

6.2 Future Work

Printed electronics is a very new field of research. Therefore, there are many scopes to contribute to this field in the future including finding and characterizing new materials for printed MEMS, process development, design of novel devices and reliability studies.

Development of stress and stress gradients in the processed films is one of the major concerns in MEMS. However, the study of stress and stress gradient development in solution processed films is very sparse. For example, a large number of studies have been conducted on the synthesis of metallic nanoparticles and their printability [57], [145], [165]–[174], but there are very few studies on the stress characteristics of the films formed from these metallic nanoparticles ink. The size of the nanoparticles, the solvent system, the stabilizer and the other organic additives used to make the ink have influence on the sintering and stress properties of the metallic films. Figure 6-1 shows doubly clamped silver beams formed from two different commercial silver inks; one is CCI-300 from Cabot Corp. and the other is EMD 5730 from Sun Chemicals. The stress gradient developed in the CCI-300 creates a large dome shaped profile of the beam, while the upward bending of the beam made with EMD 5730 ink is small. A detailed study on the design of ink to regulate the development of stress and stress gradient in the film is necessary for the progress of printed MEMS.

A comprehensive study on the reliability of the printed MEM devices needs to be done to employ them in realistic applications. For example, the three terminal reed relay presented in chapter 4 showed reliable operation up to 10^5 hot switching cycles. But for the potential application of the MEM relays as switching devices in active matrix backplane of display devices, the relays must provide reliable switching operation for over 10^{12} cycles. The failure of MEM relays due to welding between source and drain terminal has been reported [86]. The other major failure mechanisms of the MEM relays include fatigue of the structure and dielectric charging. A through study on the failure mechanism of the three and four terminal relay is necessary to improve the relay design for better performance.
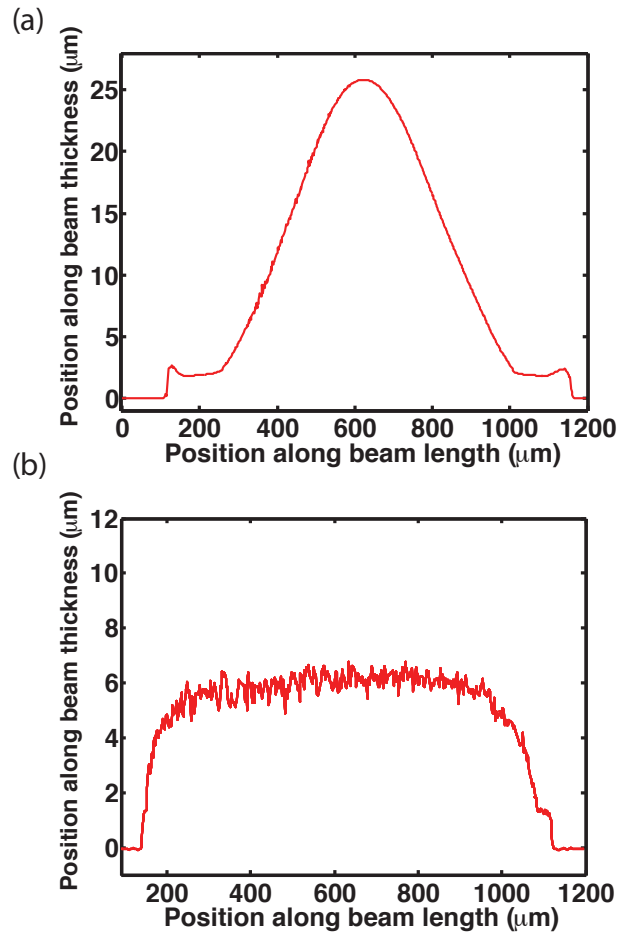
Figure 6-1. Doubly clamped silver beams formed from two different commercial silver inks; (a) CCI-300 from Cabot Corp and (b) EMD 5730 from Sun Chemicals.

So far, PMMA is the only material that has been used for the sacrificial layer in these MEMS processes. Although, PMMA shows moderately good performance as the MEMS sacrificial layer, the maximum processing temperature needs to be limited to less than 140 ^{0}C for a reliable process. This limits the choice of structural materials and their curing conditions. Also, a mechanically strong body dielectric is necessary to eliminate the requirement of the silver patch in the four terminal relay presented in chapter 5. This will reduce a processing step and makes the process flow more simple and reliable.

As a future direction of printed MEMS, the 'stress-engineered processing' technique can be employed for the fabrication of on-chip three-dimensional (3D) electrical devices with superior performances utilizing the stress gradient in the printed films. As discussed in chapter 3, the printed silver films formed from nanoparticles based ink curl in the circular fashion. These curled up circular films have a well defined radius of curvature (r). A planar beam fabricated on a sacrificial

layer with the beam length equal to $2\pi r$ makes a complete circle after release. Figure 6-2 (a) and (b) show the isometric view and the side view of the out-of-plane circles fabricated using a stress-engineered processing technique. The potential application of these 3D circles include micro-heaters, antennas, inductors etc.
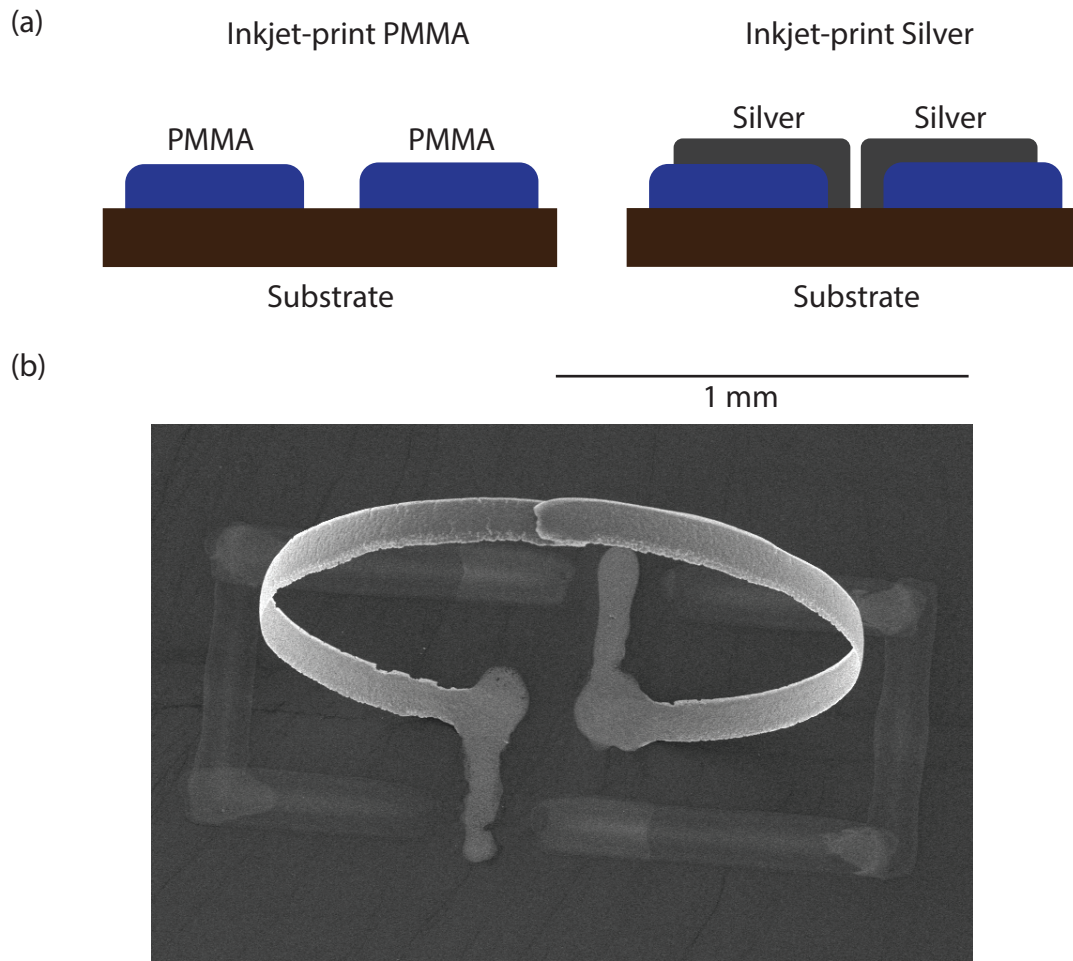
Figure 6-2. (a) Processes flow and (b) SEM image of the inkjet-printed on-chip 3D inductors.

Figure 6-2(a) shows the process flow to fabricate on-chip 3D inductors. Two back to back silver beams were printed on the PMMA sacrificial. After release, these beams curl up and their tips touch with each other to form an inductor. Figure 6-2(b) shows the SEM image of the inductor formed after the release of silver beams.

(a)

(b)
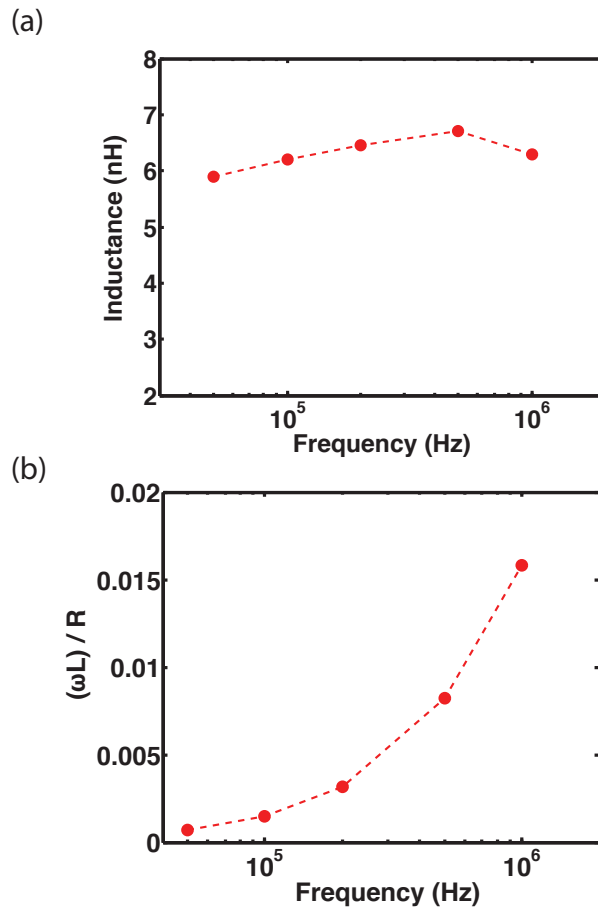
Figure 6-3. Inductance and ωL/R of the inkjet-printed one loop 3D inductor. Here, ω is the angular frequency, and L is the inductance and R is the resistance of the inductor in series configuration.

The three dimensional nature of this inductor is supposed to deliver high quality factor (Q-factor) through elimination of substrate losses. The electrical measurement of this inductor using a precision LCR meter with a range of 20 Hz to 1 MHz showed an inductance of ~6 nH with low loss (see Figure 6-3). For a more accurate measurement of the inductance value and to calculate the Q factor, this inductor needs to be characterized up to 10 GHz frequency range using two-port radio-frequency (RF) measurements. Also, inductors with more than one loop need to be fabricated and characterized.

In a nutshell, the field of printed MEMS is flourishing and further studies on its various aspects are required for its triumph.

Chapter 7:   References

[1] R. M. Solow, "A Contribution to the Theory of Economic Growth," *Q. J. Econ.*, vol. 70, no. 1, pp. 65–94, Feb. 1956.

[2] T. W. Swan, "ECONOMIC GROWTH and CAPITAL ACCUMULATION," *Econ. Rec.*, vol. 32, no. 2, pp. 334–361, Nov. 1956.

[3] V. Subramanian, J. B. Chang, A. d l F. Vornbrock, D. C. Huang, L. Jagannathan, F. Liao, B. Mattis, S. Molesa, D. R. Redinger, D. Soltman, S. K. Volkman, and Q. Zhang, "Printed electronics for low-cost electronic systems: Technology status and application development," in *ESSDERC 2008 - 38th European Solid-State Device Research Conference*, 2008, pp. 17–24.

[4] A. C. Arias, J. D. MacKenzie, I. McCulloch, J. Rivnay, and A. Salleo, "Materials and Applications for Large Area Electronics: Solution-Based Approaches," *Chem. Rev.*, vol. 110, no. 1, pp. 3–24, Jan. 2010.

[5] P. F. Moonen, I. Yakimets, and J. Huskens, "Fabrication of Transistors on Flexible Substrates: from Mass-Printing to High-Resolution Alternative Lithography Strategies," *Adv. Mater.*, vol. 24, no. 41, pp. 5526–5541, Nov. 2012.

[6] S. Owa, S. Wakamoto, M. Murayama, H. Yaegashi, and K. Oyama, "Immersion lithography extension to sub-10nm nodes with multiple patterning," 2014, vol. 9052, p. 90520O–90520O–9.

[7] A. C. Arias, S. E. Ready, R. Lujan, W. S. Wong, K. E. Paul, A. Salleo, M. L. Chabinyc, R. Apte, R. A. Street, Y. Wu, P. Liu, and B. Ong, "All jet-printed polymer thin-film transistor active-matrix backplanes," *Appl. Phys. Lett.*, vol. 85, no. 15, pp. 3304–3306, Oct. 2004.

[8] J. Daniel, A. C. Arias, W. Wong, R. Lujan, S. Ready, B. Krusor, and R. Street, "Jet-Printed Active-Matrix Backplanes and Electrophoretic Displays," *Jpn. J. Appl. Phys.*, vol. 46, no. 3B, pp. 1363–1369, Mar. 2007.

[9] A. C. Arias, J. Daniel, B. Krusor, S. Ready, V. Sholin, and R. Street, "All-additive ink-jet-printed display backplanes: Materials development and integration," *J. Soc. Inf. Disp.*, vol. 15, no. 7, pp. 485–490, Jul. 2007.

[10] V. Subramanian, J. M. J. Frechet, P. C. Chang, D. C. Huang, J. B. Lee, S. E. Molesa, A. R. Murphy, D. R. Redinger, and S. K. Volkman, "Progress Toward Development of All-Printed RFID Tags: Materials, Processes, and Devices," *Proc. IEEE*, vol. 93, no. 7, pp. 1330–1338, Jul. 2005.

[11] H. Andersson, A. Manuilskiy, J. Gao, C. Lidenmark, J. Sidén, S. Forsberg, T. Unander, and H. E. Nilsson, "Investigation of Humidity Sensor Effect in Silver Nanoparticle Ink Sensors Printed on Paper," *IEEE Sens. J.*, vol. 14, no. 3, pp. 623–628, Mar. 2014.

[12] F. Molina-Lopez, D. Briand, and N. F. de Rooij, "All additive inkjet printed humidity sensors on plastic substrate," *Sens. Actuators B Chem.*, vol. 166–167, pp. 212–222, May 2012.

[13] H. Sirringhaus, T. Kawase, R. H. Friend, T. Shimoda, M. Inbasekaran, W. Wu, and E. P. Woo, "High-Resolution Inkjet Printing of All-Polymer Transistor Circuits," *Science*, vol. 290, no. 5499, pp. 2123–2126, Dec. 2000.

[14] Y.-Y. Noh, N. Zhao, M. Caironi, and H. Sirringhaus, "Downscaling of self-aligned, all-printed polymer thin-film transistors," *Nat. Nanotechnol.*, vol. 2, no. 12, pp. 784–789, Dec. 2007.

[15] M. M. Ling and Z. Bao, "Thin Film Deposition, Patterning, and Printing in Organic Thin Film Transistors," *Chem. Mater.*, vol. 16, no. 23, pp. 4824–4840, Nov. 2004.

[16] H.-Y. Tseng and V. Subramanian, "All inkjet-printed, fully self-aligned transistors for low-cost circuit applications," *Org. Electron.*, vol. 12, no. 2, pp. 249–256, Feb. 2011.

[17] G. Grau, R. Kitsomboonloha, S. L. Swisher, H. Kang, and V. Subramanian, "Printed Transistors on Paper: Towards Smart Consumer Product Packaging," *Adv. Funct. Mater.*, vol. 24, no. 32, pp. 5067–5074, Aug. 2014.

[18] K. Braam and V. Subramanian, "A Stencil Printed, High Energy Density Silver Oxide Battery Using a Novel Photopolymerizable Poly(acrylic acid) Separator," *Adv. Mater.*, vol. 27, no. 4, pp. 689–694, Jan. 2015.

[19] E. S. Park, Y. Chen, T.-J. K. Liu, and V. Subramanian, "A New Switching Device for Printed Electronics: Inkjet-Printed Microelectromechanical Relay," *Nano Lett.*, vol. 13, no. 11, pp. 5355–5360, Nov. 2013.

[20] S. Chung, M. A. Ul Karim, H.-J. Kwon, and V. Subramanian, "High-Performance Inkjet-Printed Four-Terminal Microelectromechanical Relays and Inverters," *Nano Lett.*, vol. 15, no. 5, pp. 3261–3266, May 2015.

[21] S. Chung, M. A. U. Karim, M. Spencer, H.-J. Kwon, C. P. Grigoropoulos, E. Alon, and V. Subramanian, "Exploitation of the coffee-ring effect to realize mechanically enhanced inkjet-printed microelectromechanical relays with U-bar-shaped cantilevers," *Appl. Phys. Lett.*, vol. 105, no. 26, p. 261901, Dec. 2014.

[22] J. Yang, D. Vak, N. Clark, J. Subbiah, W. W. H. Wong, D. J. Jones, S. E. Watkins, and G. Wilson, "Organic photovoltaic modules fabricated by an industrial gravure printing proofer," *Sol. Energy Mater. Sol. Cells*, vol. 109, pp. 47–55, Feb. 2013.

[23] S. Tekoglu, G. Hernandez-Sosa, E. Kluge, U. Lemmer, and N. Mechau, "Gravure printed flexible small-molecule organic light emitting diodes," *Org. Electron.*, vol. 14, no. 12, pp. 3493–3499, Dec. 2013.

[24] T. Sekitani, H. Nakajima, H. Maeda, T. Fukushima, T. Aida, K. Hata, and T. Someya, "Stretchable active-matrix organic light-emitting diode display using printable elastic conductors," *Nat Mater*, vol. 8, no. 6, pp. 494–499, Jun. 2009.

[25] S.-C. Chang, J. Liu, J. Bharathan, Y. Yang, J. Onohara, and J. Kido, "Multicolor Organic Light-Emitting Diodes Processed by Hybrid Inkjet Printing," *Adv. Mater.*, vol. 11, no. 9, pp. 734–737, Jun. 1999.

[26] T. R. Hebner, C. C. Wu, D. Marcy, M. H. Lu, and J. C. Sturm, "Ink-jet printing of doped polymers for organic light emitting devices," *Appl. Phys. Lett.*, vol. 72, no. 5, pp. 519–521, Feb. 1998.

[27] B. S. Cook and A. Shamim, "Inkjet Printing of Novel Wideband and High Gain Antennas on Low-Cost Paper Substrate," *IEEE Trans. Antennas Propag.*, vol. 60, no. 9, pp. 4148–4156, Sep. 2012.

[28] G. McKerricher, J. G. Perez, and A. Shamim, "Fully Inkjet Printed RF Inductors and Capacitors Using Polymer Dielectric and Silver Conductive Ink With Through Vias," *IEEE Trans. Electron Devices*, vol. 62, no. 3, pp. 1002–1009, Mar. 2015.

[29] W. A. MacDonald, M. K. Looney, D. MacKerron, R. Eveson, R. Adam, K. Hashimoto, and K. Rakos, "Latest advances in substrates for flexible electronics," *J. Soc. Inf. Disp.*, vol. 15, no. 12, pp. 1075–1083, Dec. 2007.

[30] R. Rustin, "Overview of plastic substrates for printed electronics." .

[31] D. Huang, F. Liao, S. Molesa, D. Redinger, and V. Subramanian, "Plastic-Compatible Low Resistance Printable Gold Nanoparticle Conductors for Flexible Electronics," *J. Electrochem. Soc.*, vol. 150, no. 7, pp. G412–G417, Jul. 2003.

[32] J. R. Greer and R. A. Street, "Thermal cure effects on electrical performance of nanoparticle silver inks," *Acta Mater.*, vol. 55, no. 18, pp. 6345–6349, Oct. 2007.

[33] S. K. Volkman, S. Molesa, B. Mattis, P. C. Chang, and V. Subramanian, "Inkjetted Organic Transistors Using a Novel Pentacene Precursor," *Mater. Res. Soc. Symp. Proc.*, vol. 769, pp. 369–374, 2003.

[34] A. Facchetti, "Semiconductors for organic transistors," *Mater. Today*, vol. 10, no. 3, pp. 28–37, Mar. 2007.

[35] S. Allard, M. Forster, B. Souharce, H. Thiem, and U. Scherf, "Organic semiconductors for solution-processable field-effect transistors (OFETs)," *Angew. Chem. Int. Ed Engl.*, vol. 47, no. 22, pp. 4070–4098, 2008.

[36] H. Sirringhaus, "Materials and Applications for Solution-Processed Organic Field-Effect Transistors," *Proc. IEEE*, vol. 97, no. 9, pp. 1570–1579, Sep. 2009.

[37] Y. Kato, T. Sekitani, Y. Noguchi, M. Takamiya, T. Sakurai, and T. Someya, "A large-area, flexible, ultrasonic imaging system with a printed organic transistor active matrix," in *2008 IEEE International Electron Devices Meeting*, 2008, pp. 1–4.

[38] H. e. a. Huitema, G. h. Gelinck, J. b. p. h. van der Putten, K. e. Kuijk, C. m. Hart, E. Cantatore, and D. m. de Leeuw, "Active-Matrix Displays Driven by Solution-Processed Polymeric Transistors," *Adv. Mater.*, vol. 14, no. 17, pp. 1201–1204, Sep. 2002.

[39] H. Sirringhaus, S. E. Burns, C. Kuhn, K. Jacobs, J. D. MacKenzie, M. Etchells, K. Chalmers, P. Devine, N. Murton, N. Stone, D. Wilson, P. Cain, T. Brown, A. C. Asais, J. Mills, and R. H. Friend, "34.1: Active Matrix Displays Made with Printed Polymer Thin Film Transistors," *SID Symp. Dig. Tech. Pap.*, vol. 34, no. 1, pp. 1084–1087, May 2003.

[40] K. Suzuki, K. Yutani, M. Nakashima, A. Onodera, S. Mizukami, M. Kato, T. Tano, H. Tomono, M. Yanagisawa, and K. Kameyama, "All-Printed Organic TFT Backplanes for Flexible Electronic Paper," *J. Imaging Soc. Jpn.*, vol. 50, no. 2, pp. 142–147, 2011.

[41] R. R. Søndergaard, M. Hösel, and F. C. Krebs, "Roll-to-Roll fabrication of large area functional organic materials," *J. Polym. Sci. Part B Polym. Phys.*, vol. 51, no. 1, pp. 16–34, Jan. 2013.

[42] R. Soukup, A. Hamáček, and J. Řeboun, "Organic based sensors: Novel screen printing technique for sensing layers deposition," in *2012 35th International Spring Seminar on Electronics Technology*, 2012, pp. 19–24.

[43] G. E. Jabbour, R. Radspinner, and N. Peyghambarian, "Screen printing for the fabrication of organic light-emitting devices," *IEEE J. Sel. Top. Quantum Electron.*, vol. 7, no. 5, pp. 769–773, Sep. 2001.

[44] R. Brendel, A. Aberle, A. Cuevas, S. Glunz, G. Hahn, J. Poortmans, R. Sinton, A. Weeber, H. Hannebauer, T. Dullweber, T. Falcon, and R. Brendel, "Fineline Printing Options for High Efficiencies and Low Ag Paste Consumption," *Energy Procedia*, vol. 38, pp. 725–731, Jan. 2013.

[45] D. Erath, A. Filipović, M. Retzlaff, A. K. Goetz, F. Clement, D. Biro, and R. Preu, "Advanced screen printing technique for high definition front side metallization of crystalline silicon solar cells," *Sol. Energy Mater. Sol. Cells*, vol. 94, no. 1, pp. 57–61, Jan. 2010.

[46] F. C. Krebs, "Fabrication and processing of polymer solar cells: A review of printing and coating techniques," *Sol. Energy Mater. Sol. Cells*, vol. 93, no. 4, pp. 394–412, Apr. 2009.

[47] S. Khan, L. Lorenzelli, and R. S. Dahiya, "Technologies for Printing Sensors and Electronics Over Large Flexible Substrates: A Review," *IEEE Sens. J.*, vol. 15, no. 6, pp. 3164–3185, Jun. 2015.

[48] D. Sung, A. de la F. Vornbrock, and V. Subramanian, "Scaling and Optimization of Gravure-Printed Silver Nanoparticle Lines for Printed Electronics," *IEEE Trans. Compon. Packag. Technol.*, vol. 33, no. 1, pp. 105–114, Mar. 2010.

[49] M. Pudas, N. Halonen, P. Granat, and J. Vähäkangas, "Gravure printing of conductive particulate polymer inks on flexible substrates," *Prog. Org. Coat.*, vol. 54, no. 4, pp. 310–316, Dec. 2005.

[50] D. Zielke, A. C. Hübler, U. Hahn, N. Brandt, M. Bartzsch, U. Fügmann, T. Fischer, J. Veres, and S. Ogier, "Polymer-based organic field-effect transistor using offset printed source/drain structures," *Appl. Phys. Lett.*, vol. 87, no. 12, p. 123508, Sep. 2005.

[51] H. Kang, R. Kitsomboonloha, K. Ulmer, L. Stecker, G. Grau, J. Jang, and V. Subramanian, "Megahertz-class printed high mobility organic thin-film transistors and inverters on plastic using attoliter-scale high-speed gravure-printed sub-5 μm gate electrodes," *Org. Electron.*, vol. 15, no. 12, pp. 3639–3647, Dec. 2014.

[52] R. Kitsomboonloha, S. J. S. Morris, X. Rong, and V. Subramanian, "Femtoliter-Scale Patterning by High-Speed, Highly Scaled Inverse Gravure Printing," *Langmuir*, vol. 28, no. 48, pp. 16711–16723, Dec. 2012.

[53] L. Jacot-Descombes, M. R. Gullo, V. J. Cadarso, and J. Brugger, "Fabrication of epoxy spherical microstructures by controlled drop-on-demand inkjet printing," *J. Micromechanics Microengineering*, vol. 22, no. 7, p. 074012, 2012.

[54] G. L. Fillmore, "Drop Velocity from an Ink-Jet Nozzle," *IEEE Trans. Ind. Appl.*, vol. IA-19, no. 6, pp. 1098–1103, Nov. 1983.

[55] "Dimatix Materials Printer DMP-2800 Series User Manual. V. 1.5.0.1." .

[56] D. B. Bogy and F. E. Talke, "Experimental and Theoretical Study of Wave Propagation Phenomena in Drop-on-demand Ink Jet Devices," *IBM J Res Dev*, vol. 28, no. 3, pp. 314–321, May 1984.

[57] H. C. Nallan, J. A. Sadie, R. Kitsomboonloha, S. K. Volkman, and V. Subramanian, "Systematic Design of Jettable Nanoparticle-Based Inkjet Inks: Rheology, Acoustics, and Jettability," *Langmuir*, vol. 30, no. 44, pp. 13470–13477, Nov. 2014.

[58] D. Soltman and V. Subramanian, "Inkjet-Printed Line Morphologies and Temperature Control of the Coffee Ring Effect," *Langmuir*, vol. 24, no. 5, pp. 2224–2231, Mar. 2008.

[59] D. Soltman, B. Smith, H. Kang, S. J. S. Morris, and V. Subramanian, "Methodology for Inkjet Printing of Partially Wetting Films," *Langmuir*, vol. 26, no. 19, pp. 15686–15693, Oct. 2010.

[60] H. Kipphan, *Handbook of Print Media - Technologies and Production Methods*. Springer, 2001.

[61] D. Tobjörk and R. Österbacka, "Paper Electronics," *Adv. Mater.*, vol. 23, no. 17, pp. 1935–1961, May 2011.

[62] J. Noh, K. Jung, J. Kim, S. Kim, S. Cho, and G. Cho, "Fully Gravure-Printed Flexible Full Adder Using SWNT-Based TFTs," *IEEE Electron Device Lett.*, vol. 33, no. 11, pp. 1574–1576, Nov. 2012.

[63] H. Kempa, M. Hambsch, K. Reuter, M. Stanel, G. C. Schmidt, B. Meier, and A. C. Hubler, "Complementary Ring Oscillator Exclusively Prepared by Means of Gravure and Flexographic Printing," *IEEE Trans. Electron Devices*, vol. 58, no. 8, pp. 2765–2769, Aug. 2011.

[64] H. Park, H. Kang, Y. Lee, Y. Park, J. Noh, and G. Cho, "Fully roll-to-roll gravure printed rectenna on plastic foils for wireless power transmission at 13.56 MHz," *Nanotechnology*, vol. 23, no. 34, p. 344006, 2012.

[65] T.-M. Lee, S.-H. Lee, J.-H. Noh, D.-S. Kim, and S. Chun, "The effect of shear force on ink transfer in gravure offset printing," *J. Micromechanics Microengineering*, vol. 20, no. 12, p. 125026, 2010.

[66] N. Choi, H. Wee, S. Nam, J. Lavelle, and M. Hatalis, "A modified offset roll printing for thin film transistor applications," *Microelectron. Eng.*, vol. 91, pp. 93–97, Mar. 2012.

[67] T.-M. Lee, J.-H. Noh, I. Kim, D.-S. Kim, and S. Chun, "Reliability of gravure offset printing under various printing conditions," *J. Appl. Phys.*, vol. 108, no. 10, p. 102802, Nov. 2010.

[68] H. Yan, Z. Chen, Y. Zheng, C. Newman, J. R. Quinn, F. Dötz, M. Kastler, and A. Facchetti, "A high-mobility electron-transporting polymer for printed transistors," *Nature*, vol. 457, no. 7230, pp. 679–686, Feb. 2009.

[69] D. Deganello, J. A. Cherry, D. T. Gethin, and T. C. Claypole, "Impact of metered ink volume on reel-to-reel flexographic printed conductive networks for enhanced thin film conductivity," *Thin Solid Films*, vol. 520, no. 6, pp. 2233–2237, Jan. 2012.

[70] M. K. Kwak, K. H. Shin, E. Y. Yoon, and K. Y. Suh, "Fabrication of conductive metal lines by plate-to-roll pattern transfer utilizing edge dewetting and flexographic printing," *J. Colloid Interface Sci.*, vol. 343, no. 1, pp. 301–305, Mar. 2010.

[71] T. X. Liang, W. Z. Sun, L. D. Wang, Y. H. Wang, and H. D. Li, "Effect of surface energies on screen printing resolution," *IEEE Trans. Compon. Packag. Manuf. Technol. Part B*, vol. 19, no. 2, pp. 423–426, May 1996.

[72] C. W. P. Shi, X. Shan, G. Tarapata, R. Jachowicz, J. Weremczuk, and H. T. Hui, "Fabrication of wireless sensors on flexible film using screen printing and via filling," *Microsyst. Technol.*, vol. 17, no. 4, pp. 661–667, Nov. 2010.

[73] W. Y. Chang, T. H. Fang, H. J. Lin, Y. T. Shen, and Y. C. Lin, "A Large Area Flexible Array Sensors Using Screen Printing Technology," *J. Disp. Technol.*, vol. 5, no. 6, pp. 178–183, Jun. 2009.

[74] J. Perelaer, P. J. Smith, D. Mager, D. Soltman, S. K. Volkman, V. Subramanian, J. G. Korvink, and U. S. Schubert, "Printed electronics: the challenges involved in printing devices, interconnects, and contacts based on inorganic materials," *J. Mater. Chem.*, vol. 20, no. 39, pp. 8446–8453, Sep. 2010.

[75] M. Singh, H. M. Haverinen, P. Dhagat, and G. E. Jabbour, "Inkjet Printing—Process and Its Applications," *Adv. Mater.*, vol. 22, no. 6, pp. 673–685, Feb. 2010.

[76] W. Kang, M. Kitamura, and Y. Arakawa, "High performance inkjet-printed C60 fullerene thin-film transistors: Toward a low-cost and reproducible solution process," *Org. Electron.*, vol. 14, no. 2, pp. 644–648, Feb. 2013.

[77] B. J. Kang, C. K. Lee, and J. H. Oh, "All-inkjet-printed electrical components and circuit fabrication on a plastic substrate," *Microelectron. Eng.*, vol. 97, pp. 251–254, Sep. 2012.

[78] W. Smaal, C. Kjellander, Y. Jeong, A. Tripathi, B. van der Putten, A. Facchetti, H. Yan, J. Quinn, J. Anthony, K. Myny, W. Dehaene, and G. Gelinck, "Complementary integrated circuits on plastic foil using inkjet printed n- and p-type organic semiconductors: Fabrication, characterization, and circuit analysis," *Org. Electron.*, vol. 13, no. 9, pp. 1686–1692, Sep. 2012.

[79] A. Hierlemann and H. Baltes, "CMOS-based chemical microsensors," *Analyst*, vol. 128, no. 1, pp. 15–28, Dec. 2003.

[80] G. T. A. Kovacs, *Micromachined Transducers Sourcebook*. New York: McGraw-Hill, 1998.

[81] S. Yoneoka, M. Liger, G. Yama, R. Schuster, F. Purkl, J. Provine, F. B. Prinz, R. T. Howe, and T. W. Kenny, "ALD-metal uncooled bolometer," in *2011 IEEE 24th International Conference on Micro Electro Mechanical Systems (MEMS)*, 2011, pp. 676–679.

[82] "Jack St Clair Kilby Biography by Texas Instruments." [Online]. Available: http://www.ti.com/corp/docs/kilbyctr/jackstclair.shtml. [Accessed: 16-Jun-2016].

[83] G. E. Moore, "Cramming More Components Onto Integrated Circuits," *Proc. IEEE*, vol. 86, no. 1, pp. 82–85, Jan. 1998.

[84] "Progress in digital integrated electronics," in *Electron Devices Meeting, 1975 International*, 1975, vol. 21, pp. 11–13.

[85] "Intel Processors," *Intel® ARK (Product Specs)*. [Online]. Available: http://ark.intel.com/. [Accessed: 16-Jun-2016].

[86] R. Nathanael, "Nano-Electro-Mechanical (NEM) Relay Devices and Technology for Ultra-Low Energy Digital Integrated Circuits," University of California, Berkeley, 2012.

[87] V. Pott, H. Kam, R. Nathanael, J. Jeon, E. Alon, and T. J. K. Liu, "Mechanical Computing Redux: Relays for Integrated Circuit Applications," *Proc. IEEE*, vol. 98, no. 12, pp. 2076–2094, Dec. 2010.

[88] R. Nathanael, V. Pott, H. Kam, J. Jeon, E. Alon, and T. J. K. Liu, "Four-Terminal-Relay Body-Biasing Schemes for Complementary Logic Circuits," *IEEE Electron Device Lett.*, vol. 31, no. 8, pp. 890–892, Aug. 2010.

[89] H. Kam, V. Pott, R. Nathanael, J. Jeon, E. Alon, and T.-J. K. Liu, "Design and reliability of a micro-relay technology for zero-standby-power digital logic applications," in *2009 IEEE International Electron Devices Meeting (IEDM)*, 2009, pp. 1–4.

[90] J. Jeon, V. Pott, H. Kam, R. Nathanael, E. Alon, and T. J. K. Liu, "Perfectly Complementary Relay Design for Digital Logic Applications," *IEEE Electron Device Lett.*, vol. 31, no. 4, pp. 371–373, Apr. 2010.

[91] M. Spencer, F. Chen, C. C. Wang, R. Nathanael, H. Fariborzi, A. Gupta, H. Kam, V. Pott, J. Jeon, T. J. K. Liu, D. Markovic, E. Alon, and V. Stojanovic, "Demonstration of Integrated Micro-Electro-Mechanical Relay Circuits for VLSI Applications," *IEEE J. Solid-State Circuits*, vol. 46, no. 1, pp. 308–320, Jan. 2011.

[92] S. B. Fuller, E. J. Wilhelm, and J. M. Jacobson, "Ink-jet printed nanoparticle microelectromechanical systems," *J. Microelectromechanical Syst.*, vol. 11, no. 1, pp. 54–60, Feb. 2002.

[93] E. J. Wilhelm, B. T. Neltner, and J. M. Jacobson, "Nanoparticle-based microelectromechanical systems fabricated on plastic," *Appl. Phys. Lett.*, vol. 85, no. 26, pp. 6424–6426, Dec. 2004.

[94] S. Nakano, T. Sekitani, T. Yokota, and T. Someya, "Low operation voltage of inkjet-printed plastic sheet-type micromechanical switches," *Appl. Phys. Lett.*, vol. 92, no. 5, p. 053302, Feb. 2008.

[95] T. Sekitani, M. Takamiya, Y. Noguchi, S. Nakano, Y. Kato, T. Sakurai, and T. Someya, "A large-area wireless power-transmission sheet using printed organic transistors and plastic MEMS switches," *Nat. Mater.*, vol. 6, no. 6, pp. 413–417, Jun. 2007.

[96] T. Yokota, S. Nakano, T. Sekitani, and T. Someya, "Plastic complementary microelectromechanical switches," *Appl. Phys. Lett.*, vol. 93, no. 2, p. 023305, Jul. 2008.

[97] E. W. Lam, H. Li, and M. A. Schmidt, "Silver nanoparticle structures realized by digital surface micromachining," in *TRANSDUCERS 2009 - 2009 International Solid-State Sensors, Actuators and Microsystems Conference*, 2009, pp. 1698–1701.

[98] E. Lueder, "Addressing Schemes for Liquid Crystal Displays," in *Liquid Crystal Displays*, John Wiley & Sons, Ltd, 2010, pp. 185–187.

[99] J. A. Castellano, *Liquid Gold: The Story of Liquid Crystal Displays and the Creation of an Industry*. WORLD SCIENTIFIC, 2005.

[100] C. Hilsum, "Flat-panel electronic displays: a triumph of physics, chemistry and engineering," *Philos. Trans. R. Soc. Lond. Math. Phys. Eng. Sci.*, vol. 368, no. 1914, pp. 1027–1082, Mar. 2010.

[101] C. A. Bower, E. Menard, S. Bonafede, J. W. Hamer, and R. S. Cok, "Active-matrix OLED display backplanes using transfer-printed microscale integrated circuits," in *2010 Proceedings 60th Electronic Components and Technology Conference (ECTC)*, 2010, pp. 1339–1343.

[102] D.-U. Jin, J.-S. Lee, T.-W. Kim, S.-G. An, D. Straykhilev, Y.-S. Pyo, H.-S. Kim, D.-B. Lee, Y.-G. Mo, H.-D. Kim, and H.-K. Chung, "65.2: Distinguished Paper: World-Largest (6.5") Flexible Full Color Top Emission AMOLED Display on Plastic Film and Its Bending Properties," *SID Symp. Dig. Tech. Pap.*, vol. 40, no. 1, pp. 983–985, Jun. 2009.

[103] J. Y. Kwon, K. S. Son, J. S. Jung, T. S. Kim, M. K. Ryu, K. B. Park, B. W. Yoo, J. W. Kim, Y. G. Lee, K. C. Park, S. Y. Lee, and J. M. Kim, "Bottom-Gate Gallium Indium Zinc Oxide Thin-Film Transistor Array for High-Resolution AMOLED Display," *IEEE Electron Device Lett.*, vol. 29, no. 12, pp. 1309–1311, Dec. 2008.

[104] W. c Kao, J. a Ye, F. s Lin, P. y Cheng, and R. Sprague, "Configurable timing controller design for active matrix electrophoretic display," *IEEE Trans. Consum. Electron.*, vol. 55, no. 1, pp. 1–5, Feb. 2009.

[105] R. Zehner, K. Amundson, A. Knaian, B. Zion, M. Johnson, and G. Zhou, "20.2: Drive Waveforms for Active Matrix Electrophoretic Displays," *SID Symp. Dig. Tech. Pap.*, vol. 34, no. 1, pp. 842–845, May 2003.

[106] G. H. Gelinck, H. E. A. Huitema, E. van Veenendaal, E. Cantatore, L. Schrijnemakers, J. B. P. H. van der Putten, T. C. T. Geuns, M. Beenhakkers, J. B. Giesbers, B.-H. Huisman, E. J. Meijer, E. M. Benito, F. J. Touwslager, A. W. Marsman, B. J. E. van Rens, and D. M. de Leeuw, "Flexible active-matrix displays and shift registers based on solution-processed organic transistors," *Nat. Mater.*, vol. 3, no. 2, pp. 106–110, Feb. 2004.

[107] H. Klauk, D. J. Gundlach, J. A. Nichols, and T. N. Jackson, "Pentacene organic thin-film transistors for circuit and display applications," *IEEE Trans. Electron Devices*, vol. 46, no. 6, pp. 1258–1263, Jun. 1999.

[108] Y.-Y. Lin, D. I. Gundlach, S. F. Nelson, and T. N. Jackson, "Pentacene-based organic thin-film transistors," *IEEE Trans. Electron Devices*, vol. 44, no. 8, pp. 1325–1331, Aug. 1997.

[109] Y.-H. Kim, D.-G. Moon, and J.-I. Han, "Organic TFT array on a paper substrate," *IEEE Electron Device Lett.*, vol. 25, no. 10, pp. 702–704, Oct. 2004.

[110] F. Garnier, G. Horowitz, X. Peng, and D. Fichou, "An all-organic 'soft' thin film transistor with very high carrier mobility," *Adv. Mater.*, vol. 2, no. 12, pp. 592–594, Dec. 1990.

[111] H. Klauk, D. J. Gundlach, and T. N. Jackson, "Fast organic thin-film transistor circuits," *IEEE Electron Device Lett.*, vol. 20, no. 6, pp. 289–291, Jun. 1999.

[112] S. Chung, M. Jang, S.-B. Ji, H. Im, N. Seong, J. Ha, S.-K. Kwon, Y.-H. Kim, H. Yang, and Y. Hong, "Flexible High-Performance All-Inkjet-Printed Inverters: Organo-Compatible and Stable Interface Engineering," *Adv. Mater.*, vol. 25, no. 34, pp. 4773–4777, Sep. 2013.

[113] D. S. Chung, J.-S. Lee, J. Huang, A. Nag, S. Ithurria, and D. V. Talapin, "Low voltage, hysteresis free, and high mobility transistors from all-inorganic colloidal nanocrystals," *Nano Lett.*, vol. 12, no. 4, pp. 1813–1820, Apr. 2012.

[114] K. Fukuda, Y. Takeda, Y. Yoshimura, R. Shiwaku, L. T. Tran, T. Sekine, M. Mizukami, D. Kumaki, and S. Tokito, "Fully-printed high-performance organic thin-film transistors and circuitry on one-micron-thick polymer films," *Nat. Commun.*, vol. 5, p. 4147, Jun. 2014.

[115] B. Kim, S. Jang, M. L. Geier, P. L. Prabhumirashi, M. C. Hersam, and A. Dodabalapur, "High-speed, inkjet-printed carbon nanotube/zinc tin oxide hybrid complementary ring oscillators," *Nano Lett.*, vol. 14, no. 6, pp. 3683–3687, Jun. 2014.

[116] U. Zschieschang and H. Klauk, "Low-voltage organic transistors with steep subthreshold slope fabricated on commercially available paper," *Org. Electron.*, vol. 25, pp. 340–344, Oct. 2015.

[117] U. Zschieschang, R. Hofmockel, R. Rödel, U. Kraft, M. J. Kang, K. Takimiya, T. Zaki, F. Letzkus, J. Butschke, H. Richter, J. N. Burghartz, and H. Klauk, "Megahertz operation of flexible low-voltage organic thin-film transistors," *Org. Electron.*, vol. 14, no. 6, pp. 1516–1520, Jun. 2013.

[118] J. Jang, R. Kitsomboonloha, S. L. Swisher, E. S. Park, H. Kang, and V. Subramanian, "Transparent High-Performance Thin Film Transistors from Solution-Processed SnO2/ZrO2 Gel-like Precursors," *Adv. Mater.*, vol. 25, no. 7, pp. 1042–1047, Feb. 2013.

[119] C. Avis and J. Jang, "High-performance solution processed oxide TFT with aluminum oxide gate dielectric fabricated by a sol–gel method," *J. Mater. Chem.*, vol. 21, no. 29, pp. 10649–10652, Jul. 2011.

[120] J. Jang, H. Kang, H. C. N. Chakravarthula, and V. Subramanian, "Fully Inkjet-Printed Transparent Oxide Thin Film Transistors Using a Fugitive Wettability Switch," *Adv. Electron. Mater.*, vol. 1, no. 7, p. n/a–n/a, Jul. 2015.

[121] S. K. Volkman, S. Yin, T. Bakhishev, K. Puntambekar, V. Subramanian, and M. F. Toney, "Mechanistic Studies on Sintering of Silver Nanoparticles," *Chem. Mater.*, vol. 23, no. 20, pp. 4634–4640, Oct. 2011.

[122] J. R. Greer and R. A. Street, "Mechanical characterization of solution-derived nanoparticle silver ink thin films," *J. Appl. Phys.*, vol. 101, no. 10, p. 103529, May 2007.

[123] Y. Jang, D. H. Kim, Y. D. Park, J. H. Cho, M. Hwang, and K. Cho, "Influence of the dielectric constant of a polyvinyl phenol insulator on the field-effect mobility of a pentacene-based thin-film transistor," *Appl. Phys. Lett.*, vol. 87, no. 15, p. 152105, Oct. 2005.

[124] H. Klauk, M. Halik, U. Zschieschang, G. Schmid, W. Radlik, and W. Weber, "High-mobility polymer gate dielectric pentacene thin film transistors," *J. Appl. Phys.*, vol. 92, no. 9, pp. 5259–5263, Nov. 2002.

[125] W. Wang, D. Ma, S. Pan, and Y. Yang, "Hysteresis mechanism in low-voltage and high mobility pentacene thin-film transistors with polyvinyl alcohol dielectric," *Appl. Phys. Lett.*, vol. 101, no. 3, p. 033303, Jul. 2012.

[126] T.-S. Huang, Y.-K. Su, and P.-C. Wang, "Study of organic thin film transistor with polymethylmethacrylate as a dielectric layer," *Appl. Phys. Lett.*, vol. 91, no. 9, p. 092116, Aug. 2007.

[127] W. Bao, X. Cai, D. Kim, K. Sridhara, and M. S. Fuhrer, "High mobility ambipolar MoS2 field-effect transistors: Substrate and dielectric effects," *Appl. Phys. Lett.*, vol. 102, no. 4, p. 042104, Jan. 2013.

[128] W. L. Kalb, T. Mathis, S. Haas, A. F. Stassen, and B. Batlogg, "Organic small molecule field-effect transistors with Cytop™ gate dielectric: Eliminating gate bias stress effects," *Appl. Phys. Lett.*, vol. 90, no. 9, p. 092104, Feb. 2007.

[129] R. Gregorio and E. M. Ueno, "Effect of crystalline phase, orientation and temperature on the dielectric properties of poly (vinylidene fluoride) (PVDF)," *J. Mater. Sci.*, vol. 34, no. 18, pp. 4489–4500.

[130] R. D. Deegan, O. Bakajin, T. F. Dupont, G. Huber, S. R. Nagel, and T. A. Witten, "Capillary flow as the cause of ring stains from dried liquid drops," *Nature*, vol. 389, no. 6653, pp. 827–829, Oct. 1997.

[131] D. Kim, S. Jeong, B. K. Park, and J. Moon, "Direct writing of silver conductive patterns: Improvement of film morphology and conductance by controlling solvent compositions," *Appl. Phys. Lett.*, vol. 89, no. 26, p. 264101, Dec. 2006.

[132] H. Hu and R. G. Larson, "Marangoni Effect Reverses Coffee-Ring Depositions," *J. Phys. Chem. B*, vol. 110, no. 14, pp. 7090–7094, Apr. 2006.

[133] W. M. van Spengen, R. Puers, and I. D. Wolf, "A physical model to predict stiction in MEMS," *J. Micromechanics Microengineering*, vol. 12, no. 5, p. 702, 2002.

[134] N. Tas, T. Sonnenberg, H. Jansen, R. Legtenberg, and M. Elwenspoek, "Stiction in surface micromachining," *J. Micromechanics Microengineering*, vol. 6, no. 4, p. 385, 1996.

[135] Z. Yapu, "Stiction and anti-stiction in MEMS and NEMS," *Acta Mech. Sin.*, vol. 19, no. 1, pp. 1–10, Feb. 2003.

[136] P. Buffat and J.-P. Borel, "Size effect on the melting temperature of gold particles," *Phys. Rev. A*, vol. 13, no. 6, pp. 2287–2298, Jun. 1976.

[137] S. Wünscher, R. Abbel, J. Perelaer, and U. S. Schubert, "Progress of alternative sintering approaches of inkjet-printed metal inks and their application for manufacturing of flexible electronic devices," *J. Mater. Chem. C*, vol. 2, no. 48, pp. 10232–10261, Nov. 2014.

[138] F. C. Krebs, "All solution roll-to-roll processed polymer solar cells free from indium-tin-oxide and vacuum coating steps," *Org. Electron.*, vol. 10, no. 5, pp. 761–768, Aug. 2009.

[139] H. M. Haverinen, R. A. Myllyla, and G. E. Jabbour, "Inkjet Printed RGB Quantum Dot-Hybrid LED," *J. Disp. Technol.*, vol. 6, no. 3, pp. 87–89, Mar. 2010.

[140] K. Woo, C. Bae, Y. Jeong, D. Kim, and J. Moon, "Inkjet-printed Cu source/drain electrodes for solution-deposited thin film transistors," *J. Mater. Chem.*, vol. 20, no. 19, pp. 3877–3882, May 2010.

[141] S. Wünscher, B. Seise, D. Pretzel, S. Pollok, J. Perelaer, K. Weber, J. Popp, and U. S. Schubert, "Chip-on-foil devices for DNA analysis based on inkjet-printed silver electrodes," *Lab. Chip*, vol. 14, no. 2, pp. 392–401, Dec. 2013.

[142] J. C. Batchelor, E. A. Parker, J. A. Miller, V. Sanchez-Romaguera, and S. G. Yeates, "Inkjet printing of frequency selective surfaces," *Electron. Lett.*, vol. 45, no. 1, pp. 7–8, Jan. 2009.

[143] J. A. Sadie and V. Subramanian, "Three-Dimensional Inkjet-Printed Interconnects using Functional Metallic Nanoparticle Inks," *Adv. Funct. Mater.*, vol. 24, no. 43, pp. 6834–6842, Nov. 2014.

[144] M. A. U. Karim, S. Chung, E. Alon, and V. Subramanian, "Fully Inkjet-Printed Stress-Tolerant Microelectromechanical Reed Relays for Large-Area Electronics," *Adv. Electron. Mater.*, p. n/a–n/a, Feb. 2016.

[145] S. Magdassi, A. Bassa, Y. Vinetsky, and A. Kamyshny, "Silver Nanoparticles as Pigments for Water-Based Ink-Jet Inks," *Chem. Mater.*, vol. 15, no. 11, pp. 2208–2217, Jun. 2003.

[146] S. Magdassi, M. Grouchko, and A. Kamyshny, "Copper Nanoparticles for Printed Electronics: Routes Towards Achieving Oxidation Stability," *Materials*, vol. 3, no. 9, pp. 4626–4638, Sep. 2010.

[147] H.-H. Lee, K.-S. Chou, and K.-C. Huang, "Inkjet printing of nanosized silver colloids," *Nanotechnology*, vol. 16, no. 10, p. 2436, 2005.

[148] J. R. Greer and R. A. Street, "Thermal cure effects on electrical performance of nanoparticle silver inks," *Acta Mater.*, vol. 55, no. 18, pp. 6345–6349, Oct. 2007.

[149] B. Ingham, T. H. Lim, C. J. Dotzler, A. Henning, M. F. Toney, and R. D. Tilley, "How Nanoparticles Coalesce: An in Situ Study of Au Nanoparticle Aggregation and Grain Growth," *Chem. Mater.*, vol. 23, no. 14, pp. 3312–3317, Jul. 2011.

[150] K. K. Nanda, A. Maisels, F. E. Kruis, H. Fissan, and S. Stappert, "Higher Surface Energy of Free Nanoparticles," *Phys. Rev. Lett.*, vol. 91, no. 10, p. 106102, Sep. 2003.

[151] B. T. Anto, S. Sivaramakrishnan, L.-L. Chua, and P. K. H. Ho, "Hydrophilic Sparse Ionic Monolayer-Protected Metal Nanoparticles: Highly Concentrated Nano-Au and Nano-Ag 'Inks' that can be Sintered to Near-Bulk Conductivity at 150 °C," *Adv. Funct. Mater.*, vol. 20, no. 2, pp. 296–303, Jan. 2010.

[152] S. Sivaramakrishnan, P.-J. Chia, Y.-C. Yeo, L.-L. Chua, and P. K.-H. Ho, "Controlled insulator-to-metal transformation in printable polymer composites with nanometal clusters," *Nat. Mater.*, vol. 6, no. 2, pp. 149–155, Feb. 2007.

[153] R. k. Bordia and R. Raj, "Sintering Behavior of Ceramic Films Constrained by a Rigid Substrate," *J. Am. Ceram. Soc.*, vol. 68, no. 6, pp. 287–292, Jun. 1985.

[154] T. J. Garino and H. K. Bowen, "Kinetics of Constrained-Film Sintering," *J. Am. Ceram. Soc.*, vol. 73, no. 2, pp. 251–257, Feb. 1990.

[155] J. Choe, J. N. Calat, and G.-Q. Lu, "Constrained-film sintering of a gold circuit paste," *J. Mater. Res.*, vol. 10, no. 04, pp. 986–994, 1995.

[156] Y.-C. Lin and J.-H. Jean, "Constrained Sintering of Silver Circuit Paste," *J. Am. Ceram. Soc.*, vol. 87, no. 2, pp. 187–191, Feb. 2004.

[157] S. D. Senturia, *Microsystem design*. Boston: Kluwer Academic Publishers, 2001.

[158] M. N. Rahaman, *Sintering of ceramics*. Boca Raton, FL: CRC Press, 2008.

[159] J. Gere and B. Goodno, *Mechanics of Materials*. CL-Engineering, 2013.

[160] W. c. Oliver and G. m. Pharr, "An improved technique for determining hardness and elastic modulus using load and displacement sensing indentation experiments," *J. Mater. Res.*, vol. 7, no. 06, pp. 1564–1583, Jun. 1992.

[161] W. c. Oliver and G. m. Pharr, "Measurement of hardness and elastic modulus by instrumented indentation: Advances in understanding and refinements to methodology," *J. Mater. Res.*, vol. 19, no. 01, pp. 3–20, Jan. 2004.

[162] J. Kováčik, "Correlation between Young's modulus and porosity in porous materials," *J. Mater. Sci. Lett.*, vol. 18, no. 13, pp. 1007–1010.

[163] D. J. Lee and J. H. Oh, "Inkjet printing of conductive Ag lines and their electrical and mechanical characterization," *Thin Solid Films*, vol. 518, no. 22, pp. 6352–6356, Sep. 2010.

[164] L. C. Wei, A. B. Mohammad, and N. M. Kassim, "Analytical modeling for determination of pull-in voltage for an electrostatic actuated MEMS cantilever beam," in *IEEE International Conference on Semiconductor Electronics, 2002. Proceedings. ICSE 2002*, 2002, pp. 233–238.

[165] Z. Zhang and W. Zhu, "Controllable synthesis and sintering of silver nanoparticles for inkjet-printed flexible electronics," *J. Alloys Compd.*, vol. 649, pp. 687–693, Nov. 2015.

[166] Y. Li, Y. Wu, and B. S. Ong, "Facile Synthesis of Silver Nanoparticles Useful for Fabrication of High-Conductivity Elements for Printed Electronics," *J. Am. Chem. Soc.*, vol. 127, no. 10, pp. 3266–3267, Mar. 2005.

[167] Y.-L. Tai and Z.-G. Yang, "Facile and Scalable Preparation of Solid Silver Nanoparticles (<10 nm) for Flexible Electronics," *ACS Appl. Mater. Interfaces*, vol. 7, no. 31, pp. 17104–17111, Aug. 2015.

[168] Y. Sun and Y. Xia, "Shape-Controlled Synthesis of Gold and Silver Nanoparticles," *Science*, vol. 298, no. 5601, pp. 2176–2179, Dec. 2002.

[169] K. J. Lee, B. H. Jun, J. Choi, Y. I. Lee, J. Joung, and Y. S. Oh, "Environmentally friendly synthesis of organic-soluble silver nanoparticles for printed electronics," *Nanotechnology*, vol. 18, no. 33, p. 335601, 2007.

[170] M. Brust, M. Walker, D. Bethell, D. J. Schiffrin, and R. Whyman, "Synthesis of thiol-derivatised gold nanoparticles in a two-phase Liquid–Liquid system," *J. Chem. Soc. Chem. Commun.*, no. 7, pp. 801–802, Jan. 1994.

[171] S. Alex and A. Tiwari, "Functionalized Gold Nanoparticles: Synthesis, Properties and Applications—A Review," *J. Nanosci. Nanotechnol.*, vol. 15, no. 3, pp. 1869–1894, Mar. 2015.

[172] I. Jung, Y. H. Jo, I. Kim, and H. M. Lee, "A Simple Process for Synthesis of Ag Nanoparticles and Sintering of Conductive Ink for Use in Printed Electronics," *J. Electron. Mater.*, vol. 41, no. 1, pp. 115–121, Sep. 2011.

[173] Z. Zhang, X. Zhang, Z. Xin, M. Deng, Y. Wen, and Y. Song, "Synthesis of monodisperse silver nanoparticles for ink-jet printed flexible electronics," *Nanotechnology*, vol. 22, no. 42, p. 425601, 2011.

[174] S. K. Tam and K. M. Ng, "High-concentration copper nanoparticles synthesis process for screen-printing conductive paste on flexible substrate," *J. Nanoparticle Res.*, vol. 17, no. 12, pp. 1–12, Nov. 2015.